

UNIVERSITÄT HAMBURG

**Study of a Cation Exchange Reaction:
From Cu_{2-x}S to CuInS_2 in Nanorods**

Dissertation

zur Erlangung des Doktorgrades

Doktor der Naturwissenschaften

im

Institut für Physikalische Chemie

Fachbereich Chemie

Fakultät für Mathematik, Informatik
und Naturwissenschaften

Universität Hamburg

vorgelegt von

Felix Thiel

2023

The practical part of the present work has been carried out between March 2018 and July 2022 in the Institute of Physical Chemistry of the University of Hamburg in the group of Prof. Dr. Horst Weller.

Submitted	14 March 2023
Primary Reviewer	Prof. Dr. Horst Weller
Secondary Reviewer	Prof. Dr. Alf Mews
Disputation Date	5 May 2023
Board of Examiners	Dr. Irene Fernandez-Cuesta Prof. Dr. Horst Weller Priv. Doz. Dr. Christoph Wutz
Approved for Publication	5 May 2023

List of Publications

The following list contains chronologically ordered publications of articles in peer-reviewed journals and conference proceedings.

Journal Articles

1. Thiel, F.; Palencia, C.; Weller, H. Kinetic Analysis of the Cation Exchange in Nanorods from Cu_{2-x}S to CuInS_2 : Influence of Djurleite's Phase Transition Temperature on the Mechanism. *ACS Nano* **2023**, *17*, 3676–3685.

Conference Proceedings

1. Thiel, F.; Palencia, C.; Seher, R.; Weller, H. Cation Exchange Reactions: From Cu_{2-x}S to CuInS_2 Nanorods. Poster presented at *QD2018, 10th Conference on Quantum Dots*, Toronto, Canada, 25–29 June, 2018.
2. Thiel, F.; Palencia, C.; Weller, H. Cation Exchange Reactions: From Cu_{2-x}S to CuInS_2 Nanorods. Oral Presentation at *nanoGe Fall Meeting*, Berlin, Germany, 4–8 November, 2019.

Abstract

The direct synthesis of ternary I–III–VI nanomaterials is hampered by the ability to balance three precursor reactivities to achieve the desired size, shape, crystal structure and composition. Cation exchange (CE) reactions present an attractive two-stage alternative, in which binary nanocrystals (NCs) are initially produced as a template structure with the desired morphology, and subsequently altered post-synthetically by incorporating a second cationic species into the NCs to attain the desired ternary crystal structure. The kinetics of such reactions have not yet been fully understood and the underlying mechanisms not comprehensively analyzed.

This work presents the CE reaction with Cu-deficient djurleite nanorods (NRs) as a template structure to attain pure wurtzite CuInS₂ NRs, while maintaining the size and shape of the template. CE reaction parameters were also varied in a wide temperature range between 40 °C and 160 °C with reaction times between seconds and weeks to obtain large numbers of intermediate products. It became apparent, that the phase transition temperature of the template djurleite NRs (~ 93 °C in the bulk) had a significant impact on the reaction kinetics. Below the phase transition temperature, In was only incorporated into the surface of the NRs; while above the phase transition temperature, In could diffuse into the volume of the NRs, and a Janus-type exchange mechanism could be observed, in which CuInS₂ bands formed along the djurleite NRs.

These findings indicate that In diffusion at reaction temperatures above djurleite's phase transition temperature is strongly favored along the Cu planes of the NRs, while the diffusion through the anionic S sublattice layers along the long axis of the NRs is inhibited. Furthermore, the kinetic analysis of the CE reaction revealed a significant difference between the activation energies below and above djurleite's phase transition temperature of 37 kJ mol⁻¹. The investigations suggested that the diffusion mechanism is vacancy-mediated and limited by the creation of further vacancies during the CE reaction.

Kurzfassung

Die direkte Synthese von ternären I–III–VI Nanomaterialien ist beeinträchtigt durch die Fähigkeit, drei Präkursor-Reaktivitäten zu balancieren, um die gewünschte Größe, Form, Kristallstruktur und Komposition zu erhalten. Kationenaustauschreaktionen stellen eine attraktive zwei-stufige Alternative dar, bei welcher zuerst binäre Nanopartikel (NP) als Vorlage mit der gewünschten Morphologie hergestellt werden, um diese anschließend post-synthetisch zu verändern, indem eine zweite Kationenspezies in die NP eingebaut wird. So kann die gewünschte Kristallstruktur mit der ursprünglichen NP-Morphologie erzielt werden. Die Kinetik solcher Reaktionen ist noch immer nicht vollkommen verstanden, und der zugrundeliegende Mechanismus noch nicht vollständig aufgeklärt.

In dieser Arbeit wird der Kationenaustausch mit Cu-defizitären Djurleit Nanostäbchen (NSt) als formvorgebende Struktur präsentiert. Durch den Kationenaustausch konnten phasenreine Wurtzit-CuInS₂-NSt erhalten werden, unter Beibehaltung der ursprünglichen Größe und Form. Die Reaktionsparameter wurden weiterhin umfangreich variiert, mit Temperaturen zwischen 40 °C und 160 °C und Reaktionsdauern zwischen Sekunden und Tagen, um eine Vielzahl an intermediären Produkten herzustellen. Es wurde ersichtlich, dass die Phasenübergangstemperatur der Djurleit-NSt (~ 93 °C im Festkörper) einen signifikanten Einfluss auf die Reaktionskinetik hatte. Unter der Phasenübergangstemperatur konnte In nur in die Oberfläche der NSt eingebaut werden, während In oberhalb der Phasenübergangstemperatur in das gesamte NSt-Volumen diffundieren konnte. Hier konnte ein Janus-ähnlicher Austauschmechanismus beobachtet werden, bei welchem sich CuInS₂-Bänder entlang der Djurleit-NSt bildeten.

Diese Erkenntnisse legen nahe, dass die Diffusion von In oberhalb der Phasenübergangstemperatur von Djurleit stark bevorzugt innerhalb der Cu-Ebenen der NSt stattfindet, während die Diffusion durch die Ebenen des anionischen S-Untergitters gehemmt ist. Weiterhin konnte die kinetische Analyse zeigen, dass ein signifikanter Unterschied zwischen den Aktivierungsenergien unter- und oberhalb der Phasenübergangstemperatur von 37 kJ mol^{-1} besteht. Die Untersuchungen weisen darauf hin, dass der Diffusionsmechanismus durch Vakanzan vorangetrieben wird, und durch dessen weitere Schaffung während der Austauschreaktion limitiert ist.

Contents

List of Publications	iii
Abstract	v
Kurzfassung	vii
Contents	ix
Acronyms	xi
Glossary	xiii
List of Symbols	xv
1 Introduction	1
2 Theoretical Background	3
2.1 The Solid State	3
2.1.1 Macroscopic Properties	5
2.1.2 Nanoscopic Properties	8
2.2 Diffusion	12
2.2.1 Fick's First and Second Law of Diffusion	12
2.2.2 Solid State Diffusion	13
2.2.3 Cation Exchange	18
3 Scope	21
4 Cu_{2-x}S Nanocrystals as Starting Particles for CE Reactions	23
4.1 Permanent Properties: Morphology, Composition and Crystal Structure	24
4.2 Impermanent Properties: Thermal Stability, Oxidative Decay and Aging	28
5 Cation Exchange	31
5.1 Insights into the Cation Exchange Reaction	31
5.2 Kinetics and Diffusion Mechanism	39
5.3 Special Conditions for Cation Exchange Reactions	45
5.3.1 Cation Exchange Near the Phase Transition Temperature	46
5.3.2 UV Light Influence	50
6 Summary	57

7	Experimental Methods	61
7.1	Cu _{2-x} S Nanocrystal Synthesis	61
7.2	Cation Exchange Reaction	61
7.3	Characterization Methods	62
7.3.1	Differential Scanning Calorimetry	62
7.3.2	Energy-Dispersive X-ray Spectroscopy	63
7.3.3	Transmission Electron Microscopy	63
7.3.4	UV-Vis-NIR Spectroscopy	63
7.3.5	X-ray Diffraction	64
A	Supporting Information	65
A.1	Supporting Information regarding Chapter 4	65
A.1.1	Size Distributions of Starting Samples	65
A.1.2	Properties of Sample 080222-B	65
A.2	Supporting Information regarding Chapter 5	66
A.2.1	Calculation of Atoms in a NR Before and After a CE Reaction	66
A.2.2	Plot of the Absorbance Curve Integrals	68
A.2.3	Calculation of the Amount of Atoms on the Surface of a NR	68
A.2.4	Additional Information on the Crystal Phase Determination <i>via</i> fast Fourier transform (FFT)	69
A.2.5	Specifications regarding CE experiments under UV light Illu- mination	71
B	Safety Data	73
C	Acknowledgements	75
D	Declaration of Authorship	77
	Bibliography	79

Acronyms

AR aspect ratio.

ccp cubic close-packed.

CE cation exchange.

DSC differential scanning calorimetry.

EDX energy-dispersive X-ray spectroscopy.

FFT fast Fourier transform.

hcp hexagonally close-packed.

HRTEM high-resolution transmission electron microscopy.

LSPR localized surface plasmon resonance.

NC nanocrystal.

NHC nanoheterostructure.

NIR near-infrared.

NR nanorod.

SEM scanning electron microscopy.

TEM transmission electron microscopy.

TOP trioctylphosphine.

TOPO trioctylphosphine oxide.

T_{pt} phase transition temperature.

UV ultraviolet.

XRD X-ray powder diffraction.

Glossary

arithmetic mean The arithmetic mean, sometimes also arithmetic average, or simply mean or average, is the sum of a set of numbers, divided by the quantity of numbers in that set.

Cyanex Cyanex[®] 923 extractant is a mixture of tertiary alkyl phosphine oxides, produced by Cytec Solvay Group.

ICDD The International Centre for Diffraction Data is a nonprofit scientific organization, maintaining a database of powder diffraction patterns, the Powder Diffraction File[™] (PDF[®]).

parallelepiped A geometrical three-dimensional body confined by six parallelograms.

PDF The Powder Diffraction File[™] (PDF[®]) is the database of powder diffraction patterns, maintained by the International Centre for Diffraction Data, a nonprofit scientific organization.

UV-Vis-NIR A wavelength range of the ultraviolet (UV), visible (Vis) and near-infrared (NIR) electromagnetic spectrum, often probed *via* spectroscopic methods.

List of Symbols

a, b, c	lattice constants
A	atomic species in a crystal of A atoms
A_i	atom A in a self-interstitial site
\mathcal{A}	absorption coefficient
B	atomic species as a solute in a crystal of A atoms
B_i	atom B in an interstitial lattice site
B_s	atom B in a substitutional lattice site
\mathcal{B}	constant
C_{1V}	concentration of monovacancies (1V)
d	lattice plain distance
D	diffusivity
D_e	displacement (of charges)
E_a	activation energy
$E_{a\uparrow}$	activation energy above T_{pt}
$E_{a\downarrow}$	activation energy below T_{pt}
E_c	lowest energy of the conduction band
E^{conf}	confinement energy
E_e^{pol}	self-polarization energy of the electron
E_g	band gap energy
E_g^{bulk}	band gap energy, specifically in the bulk material
E_g^{tot}	total band gap energy
E_h^{pol}	self-polarization energy of the hole
E_n	energy eigenvalue of an electron in an orbital n
E_{Ry}^*	Rydberg energy of an exciton
E_v	highest energy of the valence band
\mathcal{E}	electric field
f	factor in Tauc method, depending on the nature of the electron transition
F	pre-exponential factor
ΔG	Gibbs free energy
ΔG_{crit}	Gibbs critical formation energy
$G_{f,1V}$	Gibbs free energy of a monovacancy formation
ΔG_m	Gibbs free energy of migration
ΔG_v	Gibbs free energy of the volume
h, k, l	Miller indices

J	flux
\vec{J}	flux vector
J_{e-h}	Coulomb interaction between the electron and hole
J_x, J_y, J_z	flux in x -, y - and z -direction
k, k'	rate constants
L	length
m	mass
m_e^*	effective mass of the electron
m_h^*	effective mass of the hole
n	electron concentration
n_1, n_2, n_3	integers
N	integer, relating to a quantity
$N_{\text{atom,NR}}$	amount of atoms per nanorod
$N_{\text{atom,uc}}$	amount of atoms per unit cell
$N_{\text{uc,NR}}$	amount of unit cells per nanorod
P	polarization
r	radius
r_{crit}	critical radius
$r_{\text{Cu-S}}$	distance of a Cu-S bond in djurleite
\vec{r}_i	jump vector of the i th jump
\vec{r}_n	lattice vector with n dimensions
\vec{R}_n	displacement vector after n jumps
S	supersaturation
t	time
T	temperature
T_{pt}	phase transition temperature
V	vacancy
V	volume
V_{NR}	volume of a nanorod
V_{uc}	volume of a unit cell
V_{m}	molar volume
W	width
x, y, z	Cartesian coordinates
Z	coordination number
α, β, γ	angles
γ_s	surface free energy
Γ	jump rate
Γ_{ex}	exchange jump rate
$\Gamma_{\text{ex,tot}}$	total exchange jump rate
ϵ	absolute permittivity
ε	energy of a fermion
η	absolute hardness (HSAB theory)

θ	diffraction angle
λ	wavelength
μ	chemical potential
ν	photon frequency
ν_0	attempt frequency
τ	residence time
ψ_n	electron wave function
ω	frequency
ω_{1V}	exchange rate between an atom and a monovacancy
ω_p	plasma frequency
∇	nabla operator, a vector whose components are partial derivatives

Chapter 1

Introduction

Nanoscience is a field that has, in the year 2023, a history of more than half a decade. Foundational works of Louis E. Brus, Alexander L. Efros and others introduced the concept of semiconductor nanomaterials in the 1980s,^[1-6] and the research field of colloidal semiconductor nanoparticles was further established, among others, by Horst Weller and colleagues in the 1990s.^[7-9] Today, nanoscience is still highly relevant and an ever-evolving research field with an increasing number of publications every year. The European Commission first adapted a definition for a nanomaterial in 2011,^[10] which in its current form defines it as "a natural, incidental or manufactured material consisting of solid particles that are present, either on their own or as identifiable constituent particles in aggregates or agglomerates" with "one or more external dimensions of the particle . . . in the size range of 1 nm to 100 nm".^[11] The small extent of nanocrystals (NCs) differentiate them from their respective bulk equivalents, resulting in size-dependent properties, which are not only defined by their chemical compositions, but by their physical properties as well. Many applications arise from these unique characteristics intrinsic to nanoparticles, e.g. solar energy conversion, optoelectronics, nanophotonics, spintronics, catalysts, bio-medical applications and more.^[12-17]

Over the years, the synthetic control of colloidal NCs improved towards tailoring the sizes and shapes of particles with a high degree of specificity, especially of II-VI and IV-VI type semiconductor NCs.^[18,19] CdSe NCs represent a popular member of the II-VI semiconductor class, which can emit light in the visible spectrum, can be prepared with a high monodispersity and excellent control over the size and shape, and thus offer a broad field of applications.^[20,21] Yet, most of the II-VI and IV-VI semiconductors contain one or more carcinogenic, mutagenic or reprotoxic substances (abbreviated as CMR substances), e.g. Cd, Hg, Pb and Se. The class of ternary I-III-VI semiconductors offers similar properties with less toxic elemental components, e.g. Cu, S and In.^[22] But due to the necessity to balance multiple precursor reactivities in syntheses of ternary compounds, the direct synthetic route often leads to subpar control over the size, shape and composition of the NCs.^[23]

However, cation exchange (CE) emerged as an attractive strategy for post-synthetic chemical modification of NCs. Particles of the desired size and shape are synthesized in a first step, and subsequently some or all cations of the host lattice are exchanged in one or multiple steps, resulting in new crystal phases. The rigid anionic sublattice of the host particle acts as a template structure, which can be conserved at much milder reaction conditions than typical for hot-injection syntheses (usually $\geq 300\text{ }^{\circ}\text{C}$ ^[18,21,24,25]), offering the possibility to reach a wide range of compositions, from particles doped with a few atoms, to fully exchanged NCs.^[26] In this way, many ternary compositions become accessible with a plethora of possible morphologies, which would otherwise not be achievable *via* direct synthetic routes.

The CE field grew steadily from early publications, reporting surface modifications in the 1990s,^[27,28] to important break-through works in 2004 offering mechanistic insights into CE reactions,^[29–31] and onwards to recent publications in 2020 designing complex nanoheterostructures (NHCs) with a multitude of incorporated materials by performing sequential CE reactions.^[32] Of special interest in the research area are anisotropic and heterostructured NCs, due to the difficulty of manufacturing them in direct synthetic approaches. Anisotropic nanostructures offer a myriad of possible applications, either individually or as building blocks for the fabrication of macroscopic functional materials, e.g. for photovoltaics, plasmonics, magnetic storage, and sensing.^[33–37]

CuInS₂ in the wurtzite crystal phase is a I–III–VI material with a direct band gap in the visible spectrum,^[38] a very large optical absorption coefficient (10^5 cm^{-1} ^[22]) with durable photostability, making it an ideal candidate as a light-absorbing material in solar cells. It has already been shown, that devices based on CuInS₂ can deliver efficiencies above 10%.^[39] But the direct synthesis of this ternary compound could still be improved. The fabrication of anisotropic wurtzite CuInS₂ NHCs could be optimized in a two-step process: Initially synthesizing anisotropic copper sulfide NCs with a high degree of control over the desired size and shape, and subsequently performing CE reactions to obtain CuInS₂ NCs under size and shape retention. By examining CE reactions in detail and producing various intermediate CuInS₂ NHCs, the mechanism of such reactions will be elucidated, making a contribution to the scientific community to more thoroughly understand the process of CE.

Chapter 2

Theoretical Background

This chapter is meant to provide brief descriptions of important theories of solid state physics as a foundation for the topics discussed in the discussions on cation exchange reactions. Firstly, properties of crystalline matter are introduced and will be discussed for the bulk, as well as for the nanoscopic scale. Further, atomic movement, especially in solids, will be discussed in the last section.

2.1 The Solid State

Two atoms of the same species can minimize their respective total energies in a solid by assuming an equilibrium distance to each other. Therefore, the surroundings in a three-dimensional solid viewed from each atom need to be equal in all directions, resulting in a periodic order, referred to as crystalline.^[40] This three-dimensional order is also present in crystalline solids with more than one component in form of repeating identical atomic groups: the base.^[41] The base of a crystal lattice is identical in its composition, configuration and orientation.^[41] This periodic arrangement of the base on a three-dimensional lattice can be expressed as a lattice vector^[40]

$$\vec{r}_n = n_1\vec{a} + n_2\vec{b} + n_3\vec{c} \quad (2.1)$$

by which every point on the lattice can be reached with any integer n_1 , n_2 and n_3 . Depending on the length ratios of the vectors \vec{a} , \vec{b} and \vec{c} , and the included angles α , β and γ , seven different basis vector systems are possible, with fourteen different lattice types.^[41] The smallest possible parallelepiped of the base vectors containing only one lattice point is called a primitive unit cell.^[40] Crystal planes could be indexed by three collinear points of a plain, but for the structure analysis it is useful to use Miller indices to describe them. They are obtained, firstly, by determining the points of intersection from the plain with the three axes a , b and c in units of the lattice parameters n_1 , n_2 and n_3 ; and secondly, by determining the reciprocal values of these integers and then finding three integers with the same ratios as the reciprocal values to each another. The Miller indices are then expressed as (hkl) .^[41]

Spheres of the same size can be ordered to maximize their packing density. If a sphere has six nearest neighbors in its plain, and three nearest neighbors in the plain

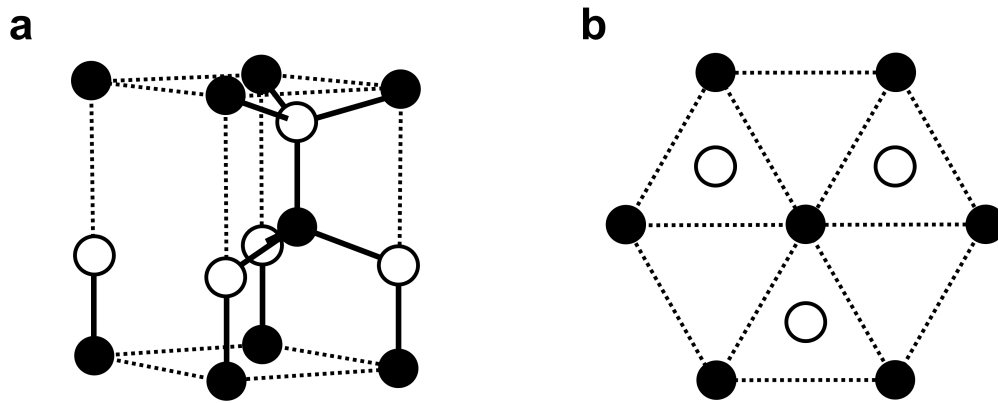


FIGURE 2.1: Two views of the wurtzite crystal structure with two atomic species represented as black and white spheres; with (a) the side view of the unit cell and (b) the view along the (111) plain illustrating the AB layer stacking, characteristic of the hcp structure.

above and below, it has a coordination number of twelve. The hexagonally close-packed (hcp) structure is one type of close-packing of equal spheres with a fraction of filled space of 0.74.^[41] The other type is the face-centered cubic or cubic close-packed (ccp) structure. One way of layering a close-packed plain of spheres A, is to stack a second equivalent layer B on top, such that every sphere of B touches three spheres of A. A third layer—again, equal to A and B—can be stacked in two ways: Either by stacking layer C, so that the spheres of that layer align with the holes of layer A, which are not occupied by layer B, resulting in a ccp structure, or by aligning the third layer of spheres to that of layer A, resulting in an AB, AB... stack, which describes the hcp structure.^[40,41] Wurtzite is an example for a hexagonal structure (see Figure 2.1), which has a tetrahedral configuration of nearest neighbors^[40], and has ABAB... layer stacking along its (111) plain.^[42] Many compounds of the II-VI compounds crystallize in the wurtzite structure, e.g. ZnO, ZnSe, CdS and CdSe, but also some tertiary compounds, like CuInS₂.^[22,40,43]

Crystal structures can be analyzed *via* diffraction of electromagnetic waves. In case of wavelengths similar to the atomic distances in a crystal, diffracted waves are only observable for certain incidence directions. X-rays meet these requirements with typical wavelengths between 1 pm to 10 nm.^[44] W. L. Bragg explained this by constructive interference of diffracted waves for certain conditions. Incoming waves are partially reflected on the crystal planes. Diffracted waves are only detectable, if the reflected waves on parallel crystal plains interfere constructively, which is expressed in the Bragg condition^[41]

$$2d \sin \theta = n\lambda \quad (2.2)$$

with the lattice plain distance d , the angle between the incidence beam and the lattice plain θ , an integer n , and the incidence wavelength λ . Just about 10^{-3} to 10^{-5} of incidence waves are reflected on any given lattice plain. So, only for certain incidence

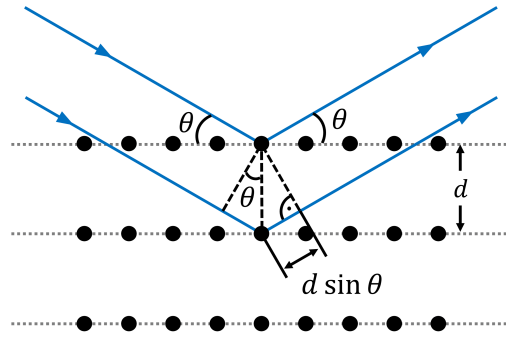


FIGURE 2.2: Depiction of parallel atomic layers with a distance d , on which incoming electromagnetic waves with an angle of incidence θ are reflected, leading to a phase difference of $2d \sin \theta$.

angles θ do the phases of reflected waves from all (or at least 10^3 to 10^5) parallel lattice planes add up to a strong signal. The path difference of X-rays in order to interfere constructively is $2d \sin \theta$, as seen in Figure 2.2.^[41]

2.1.1 Macroscopic Properties

Free Electron Model The free electron model can adequately describe properties of metals, e.g. the heat capacity, thermal and electric conductivity. The one-dimensional model assumes an electron of mass m , which is restricted by an infinitely high potential barrier, but can move freely inside the length L . The electron wave function ψ_n is a solution of the stationary Schrödinger equation^[41]

$$-\frac{\hbar^2}{2m} \frac{d^2 \psi_n}{dx^2} = E_n \psi_n \quad (2.3)$$

with the reduced Planck constant \hbar and the energy eigenvalue E_n of the electron in orbital n (an integer). An orbital is a solution of the electron wave function, which can be occupied by one electron in one quantum state.^[41] The energy E_n can be expressed as^[41]

$$E_n = \frac{\hbar^2}{2m} \left(\frac{n\pi}{L} \right)^2. \quad (2.4)$$

An orbital can be described by three different quantum numbers. The principal quantum number n denotes the shell of the electron. The quantum numbers l and m_l are in correlation to the the angular momentum of the electron.^[45] The Pauli exclusion principle states, that no two electrons can occupy the same quantum state with identical quantum numbers. Since electrons have an intrinsic angular momentum, or spin, which can be in one of two states (spin up or spin down), a system with N electrons can occupy $N/2$ orbitals. The first three quantum states of the free electron can be seen in Figure 2.3.^[41,45]

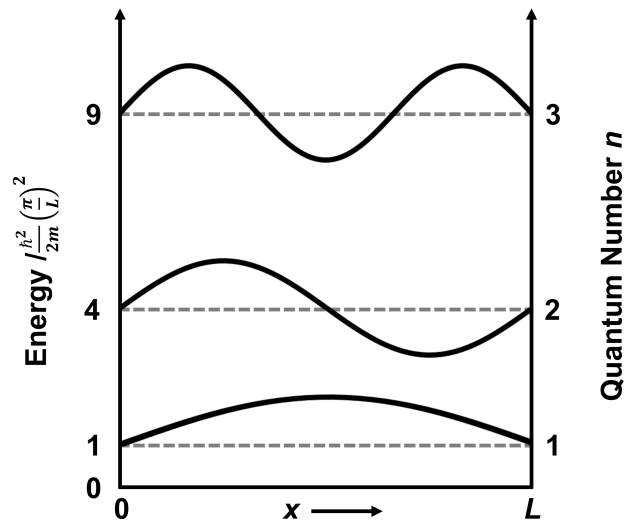


FIGURE 2.3: Illustration of the first three quantum states of a free electron with a mass m , enclosed in an infinitely high potential of width L . Depicted are standing waves of the electron wave functions with wavelengths λ of $2L$, L and $\frac{2}{3}L$ for the quantum numbers n of 1, 2 and 3, respectively.

Nearly Free Electron Model What the free electron model fails to describe is the difference between metals, insulators and semiconductors. The free electron model can be expanded to consider the periodicity of the lattice. In the model of the nearly free electron, ion cores form a periodic potential, which influence the previously thought of free propagation of electron waves in a lattice. As a result, energy regions emerge, in which no wave-like solution of the Schrödinger equation exists, referred to as a band gap.^[41] The electrons in allowed states in a crystal occupy energy bands, as depicted in Figure 2.4. If a crystal has only fully occupied and unoccupied energy bands and behaves as an insulator, no charge will be conducted in an externally applied electric field. If the band gap is small enough, electrons can be excited from the ground state into an excited state, i.e. from the valence into the conduction band, and conduct electric charge in this way. These materials are classified as semiconductors. If energy bands are only partially occupied, or the valence and conduction bands overlap, as in metals, electrons are very close to unoccupied states and can thus move almost freely through the crystal if an electric field is applied.^[41]

Optical Properties

The solid state in a crystalline form, the formation of electronic bands and the resulting classification into material classes is a self-contained framework. Now, the interaction of the solid state with electromagnetic waves will be introduced in a classic or macroscopic view, developed from the Maxwell equations.^[40] Specifically, the interaction of electromagnetic waves with a dielectric medium, i.e. weakly conductive or insulating matter. The dielectric constant ϵ is defined by a displacement (of charges)

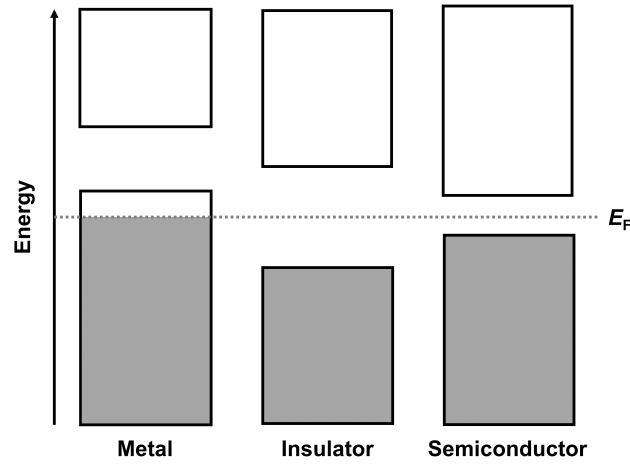


FIGURE 2.4: Illustration of the different band structures and electron occupations in insulators, metals and semiconductors. Energy bands occupied by electrons are depicted in grey, unoccupied bands are in white. Inside the boxes are allowed energy states. In the ground state of a system at absolute zero at 0 K, the highest energy state occupied by an electron is defined as the Fermi energy E_F . Above absolute zero, previously unoccupied electronic states can be occupied, due to the increased kinetic energy of the system. The Fermi-Dirac distribution $f(E) = \frac{1}{e^{(\epsilon-\mu)/k_B T} + 1}$ states the probability that an orbital with energy ϵ is occupied in a system in thermal equilibrium, with the chemical potential μ and the Boltzmann constant k_B .^[41]

D_ϵ , via the electric field \mathcal{E} and the polarization P (density of dipole moments)^[41]

$$D_\epsilon = \epsilon_0 \mathcal{E} + P = \epsilon \epsilon_0 \mathcal{E} \quad (2.5)$$

with the vacuum permittivity ϵ_0 . The dielectric function with the frequency ω can be written as^[41]

$$\epsilon(\omega) = 1 - \frac{\omega_p^2}{\omega^2} \quad (2.6)$$

with the plasma frequency $\omega_p^2 \equiv ne^2/\epsilon_0 m_e$, with the electron concentration n , the electrical charge of an electron e , and the electron mass m_e .^[41] A plasma is a medium containing equal amounts of positive and negative charges. In a crystal, negative charges in the form of electrons equal the positive charges of the ion cores. If the valence electrons are collectively excited, the resulting longitudinal displacement of electrons relative to the ion cores is called a plasma oscillation (a plasmon is the quant of the plasma oscillation). The oscillation of ion cores is much slower compared to the oscillation of electrons, and can be approximated as constant.^[41] The collective displacement of the electron plasma generates an electric field, acting as a restoring force and results in the oscillation of the plasma around a neutral position. This can be considered as a longitudinal eigen oscillation of the electron plasma with the plasma frequency ω_p .^[40] The previous explanations assumed an extended crystal lattice. But plasmons can also occur at the crystal boundary, the surface. Here, electromagnetic waves can interact with transversal lattice oscillations, and are called surface plasmon polaritons, or just surface plasmons. If the incident wavelength is

large compared to the size of the excited crystal, e.g. for visible light exciting nano-sized crystals, the surface plasmon is confined to the particle and electrons oscillate collectively, referred to as localized surface plasmon.^[46]

Absorption Following the description of the interaction of electromagnetic waves with a dielectric medium must be the resulting optical properties of such a medium. Experimentally, the dielectric function $\epsilon(\omega)$ is not accessible, but the related observables of the reflectivity, refractive index and extinction coefficient can be probed.^[41] The latter is most relevant for this work, since it provides insight into the band structure of a crystal. A semiconductor crystal with a band gap energy E_g between its occupied valence band with energy E_v and unoccupied conduction band with energy E_c , will absorb a photon with an energy of $\hbar\omega$, following^[41,45]

$$\hbar\omega = E_c - E_v. \quad (2.7)$$

If the energy of the incident photon is greater than the band gap energy, the excited electron in the conduction band can form a bond with the remaining positively charged electron hole in the valence band, stabilized by the attracting Coulomb interaction of the opposing charges. This electron-hole pair is referred to as an exciton.^[41] Excitons can exist in a weakly bound state, called Mott-Wannier excitons, and strongly bound as Frenkel excitons.^[40] A semiconductor is considered to have a direct band gap, if an exciton can be created with photon energies over the threshold of $\hbar\omega > E_g$. If an additional phonon is necessary for the excitation, the band gap is referred to as indirect.^[41]

2.1.2 Nanoscopic Properties

Electronic and optical properties of the macroscopic solid state, i.e. the bulk, often differ from those exhibited in materials of the same composition, but of nanoscopic size. Furthermore, the crystals utilized in this work were nanocrystals (NCs) as well. Therefore, properties of nanomaterials will be discussed in the following section, as well as the synthesis of such crystals.

Size Quantization Effect

The previous description of crystals forming energy bands, which can be interrupted by energy gaps, assumes a lattice of infinite size. Since the electron wave function is not confined in any dimension, quantum states, as seen in Figure 2.3, are infinitesimally close, resulting in the aforementioned band structure, in which electrons can assume energy states on a continuum.^[45] On the nanoscale, electrons and excitons, for that matter, can be confined similar to the one-dimensional model of the free electron, which confined the electron wave function in a one-dimensional potential well of length L . In case of a three-dimensional spherical NC with radius r , charge carriers of an exciton are confined in a spherical potential of the same radius. The

solution of the Schrödinger equation yields discrete energy levels, similar to that of the free electron model. The total band gap E_g^{tot} of such a semiconducting NC is then equal to the bulk band gap energy E_g^{bulk} and a confinement term E^{conf} ^[47]

$$E_g^{\text{tot}} = E_g^{\text{bulk}} + E^{\text{conf}}. \quad (2.8)$$

Depending on the radius of a NC in comparison to the Bohr radius a_0 , charge carriers can be in a strong or weak confinement regime. If $r \ll a_0$, the kinetic energies of the charge carriers are much larger than the Coulomb interaction, and the Coulomb interaction can be neglected. But if $r > a_0$, the exciton is only weakly confined, and the energy gap is expressed, including a Coulomb term, as^[47]

$$E_g^{\text{tot}}(r) = E_g^{\text{bulk}} + \frac{\hbar^2 \pi^2}{2r^2} \left(\frac{1}{m_e^*} + \frac{1}{m_h^*} \right) - J_{e-h} + E_e^{\text{pol}} + E_h^{\text{pol}} - 0.248 E_{\text{Ry}}^* \quad (2.9)$$

with the effective electron and hole masses m_e^* and m_h^* , the Coulomb interaction between the electron and hole $J_{e-h} = 1.786e^2/\epsilon r$ (with the dielectric constant of the NC ϵ), the self-polarization energies of the electron and hole E_e^{pol} and E_h^{pol} (depending on e^2/r and the dielectric constants of the NC and surrounding medium), and the exciton Rydberg energy E_{Ry}^* , accounting for the spatial correlation between the electron and hole.^[47]

As a result, firstly, energy levels in NCs are discrete and quantized, and secondly, the band gap of NCs of the same composition and crystal structure will increase with decreasing particle size.

Synthesis of Nano-Structured Matter

The formation of NCs can be divided into two parts: the nucleation and growth of particles. It is convenient for the description to introduce monomers as the smallest units of a crystal. In case of a supersaturation S of monomers in solution, defined as the ratio of monomer concentration $[M]$ to the equilibrium monomer concentration of the bulk solid $[M]_0$, the formation of crystals can relieve the excess free energy of the monomers in a supersaturated solution.^[48] Here, only homogeneous nucleation will be considered, i.e. nuclei forming homogeneously throughout the entire reaction solution, opposed to heterogeneous nucleation, occurring on structural inhomogeneities, such as reaction vessel surfaces, impurities or grain boundaries.^[49]

A nucleus, i.e. a small sphere of condensed matter, with radius r has a free energy $\Delta G(r)$ of^[48]

$$\Delta G(r) = 4\pi r^2 \gamma_s + \frac{4}{3}\pi r^3 \Delta G_v \quad (2.10)$$

with the surface free energy per unit area γ_s and the free energy of the volume ΔG_v , which is defined as^[48]

$$\Delta G_v = -\frac{k_B T \ln S}{V_m} \quad (2.11)$$

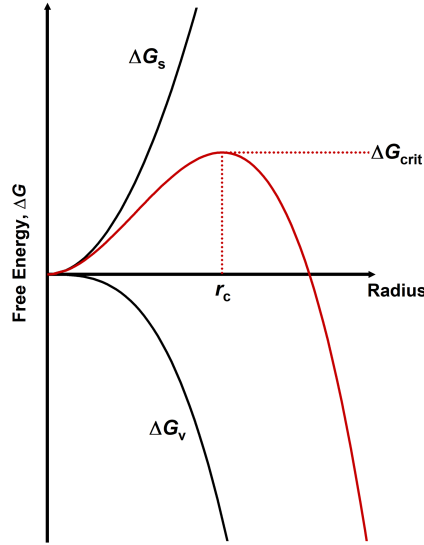


FIGURE 2.5: Plot of the free energy ΔG against the particle radius r , with a positive surface contribution ΔG_s and a negative volume contribution ΔG_v to the total free energy curve, resulting in a peak, corresponding to a critical radius r_{crit} and a critical formation energy of a crystal ΔG_{crit} .

where k_B is the Boltzmann constant, T the temperature and V_m the molar volume. The contribution of the surface and volume terms to the formation of a nucleus are plotted in Figure 2.5. The volume term $4/3\pi r^3 \Delta G_v$ promotes the nucleus formation for any value of $S > 1$, reducing the free energy, but any increase in surface area increases the free energy of the surface. Thus, the curve of the total free energy for the formation of a nucleus has a maximum at a critical radius r_{crit} . Nuclei of a radius smaller than the critical radius can not grow and dissolve back into solution, to decrease their free energy, while nuclei larger than the critical radius are able to grow. The critical radius is the smallest size, at which nuclei for a given supersaturation are stable.^[49] The critical radius can be expressed as^[48]

$$r_{\text{crit}} = \frac{-2\gamma_s}{\Delta G_v} = \frac{2\gamma_s V_m}{k_B T \ln S}. \quad (2.12)$$

The rate of nucleation is then dependent on the temperature, surface free energy, a pre-exponential factor F and, most importantly, the supersaturation (see Equation 2.13).^[48] The rate of nucleation is indeed very sensitive to the supersaturation, as Kwon and Hyeon showed: An increment from $S = 2$ to $S = 4$ resulted in an increase of the nucleation rate by a factor of $\sim 10^{70}$.^[48]

$$\frac{dN}{dt} = F \exp \left[\frac{-\Delta G_{\text{crit}}}{k_B T} \right] = F \exp \left[-\frac{16\pi\gamma_s^3 V_m^2}{3k_B^3 T^3 (\ln S)^2} \right]. \quad (2.13)$$

After the nucleation stage, the growth of NCs proceeds, which can be limited by two criteria: the transport of monomers from the solution to the surface, i.e. diffusion (discussed in the next section), and the reaction of monomers on the surface of a nuclei.^[50] In the diffusion-controlled growth regime (see left panel of Figure

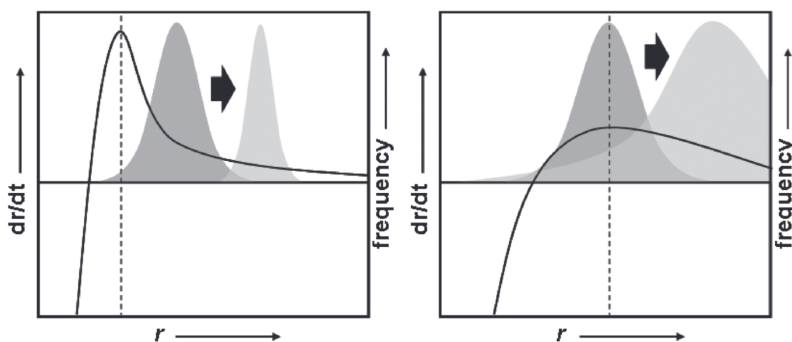


FIGURE 2.6: Two plots of growth rate against particle radius, with the evolution of the size distributions in shaded grey; depicted is a high supersaturation on the left, and a low supersaturation on the right. Reprinted with permission from Klabunde, K. J.; Richards, R. M., *Nanoscale Materials in Chemistry*, 2nd ed.; John Wiley & Sons, Inc: Hoboken, New Jersey, 2009, p 141.^[51] Copyright 2009 John Wiley & Sons, Inc.

2.6), the concentration of monomers is much higher than the solubility of NCs. In this case, all diffusion of monomers to the surface of a NC leads to the precipitation of monomers on the surface and subsequent growth. As a result, small NCs have a higher growth rate than larger ones, which leads to a narrowing particle size distribution, referred to as the size focusing effect.^[48,51] Even though the monomer concentration is high in early stages of a reaction, the level of supersaturation diminishes with ongoing reaction time. As a result, the competing crystallization reaction to the precipitation, i.e. the phase transfer of monomers from the solute to the solid phase, takes over the dissolution. In this stage, small NCs dissolve due to their high chemical potential and the shift of the critical radius to larger values. This type of NC growth is called Ostwald ripening and is controlled by the reaction rate (reaction-controlled). Due to a higher growth rate of large NCs compared to small ones, the particle size distribution broadens (see right panel of Figure 2.6).^[48,51]

The development of monomer concentration with time, with the separation into phases of nucleation and growth, is described in the LaMer model. It was first proposed for the preparation of monodisperse sulfur hydrosols by LaMer and Dinegar in 1950.^[52] The LaMer diagram, shown in Figure 2.7, is divided into three phases.^[53] In the first phase, sometimes referred to as the accumulation phase, the monomer concentration in solution rises rapidly,^[48] either as a result of precursor heating, or by injecting a precursor solution into a hot solvent, referred to as a hot injection.^[54] In the second phase, above a critical monomer concentration S_{crit} , a spontaneous burst nucleation leads to the formation of nuclei, which reduces the amount of free monomers in solution. Due to the reduced monomer concentration, no further nucleation occurs in the third phase. Instead, the previously formed nuclei enter the growth phase, which is initially controlled by the diffusion of monomers through the reaction solution to the surface of the nuclei.^[48,49,52]

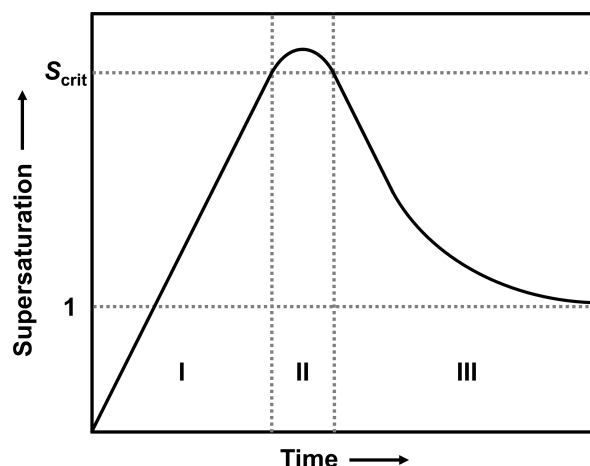


FIGURE 2.7: LaMer diagram with the supersaturation S plotted against reaction time; with horizontal dotted lines marking a supersaturation of $S = 1$, and the minimal supersaturation for homogeneous nucleation, the critical supersaturation S_{crit} ; and vertical dotted lines dividing the three phases of nucleation and growth: (I) the accumulation phase, (II) homogeneous nucleation and (III) diffusion-controlled growth.^[48,52]

2.2 Diffusion

Diffusion is the temperature-induced process of matter transport by atomic or molecular movement.^[55] Some concepts considerably advanced the understanding of diffusion. The empirical continuum theory proposed by Adolf Fick in 1855 introduced the diffusion coefficient.^[56] Later, in 1905, Albert Einstein explained the theory of Brownian motion (random motion of suspended particles), already observed and described by the eponymous Robert Brown in 1828,^[57] by a random walk triggered by collisions of the particles with solvent molecules.^[58] The atomistic description of diffusion and disorder in the solid state was later introduced in 1926 by Jakov Il'ich Frenkel, suggesting that thermal excitation causes the transition of lattice atoms to interstitial sites, leaving behind a vacancy.^[59] Shortly after, Wagner and Schottky generalized the theory of disorder for binary compounds and extended the description of interstitials to the occurrence of vacancies, self-interstitials and antisite defects.^[60]

Below, the continuum theory of diffusion will be introduced, which is applicable to gases, liquids, and the solid state. Following, more relevant to this work, diffusion theory in the solid state will be discussed in more detail. And finally, the introduced concepts will be applied to the special case of cation exchange reactions.

2.2.1 Fick's First and Second Law of Diffusion

First Law Fick's first law describes the flux of particles, which can be atoms, ions, or molecules. In its simplest form, the flux J can be described in an isotropic medium, i.e. a medium with equal physical and chemical properties in all directions, with

only one dimension^[55]

$$J_x = -D \frac{\partial C}{\partial x}. \quad (2.14)$$

Here, the flux in x -direction J_x depends on the gradient of concentration C and a proportionality factor D , which is referred to as the diffusion coefficient or diffusivity. The negative sign of Equation 2.14 implies that the flux is in opposite direction to the concentration gradient.^[55] In three dimensions, the flux is expressed as a vector, and the partial derivative is replaced with the nabla operator ∇ , acting on the scalar concentration field $C(x, y, z, t)$, which produces a concentration gradient field ∇C ^[55]

$$\vec{J} = -D \nabla C. \quad (2.15)$$

In most cases, the number of diffusing particles is conserved, and therefore the mass of a system is conserved. Thus, an equation of continuity can be phrased as^[55]

$$\text{inflow} - \text{outflow} = \text{accumulation (or loss) rate.}$$

Assuming a test volume enclosed by Δx , Δy and Δz , this equation can be approximated as^[55]

$$-\left[\frac{\partial J_x}{\partial x} + \frac{\partial J_y}{\partial y} + \frac{\partial J_z}{\partial z} \right] \Delta x \Delta y \Delta z = \frac{\partial C}{\partial t} \Delta x \Delta y \Delta z. \quad (2.16)$$

This equation can be abbreviated with the introduction of the vector operation $\nabla \cdot$ to the equation typically denoted as the continuity equation^[55]

$$-\nabla \cdot \vec{J} = \frac{\partial C}{\partial t}. \quad (2.17)$$

Second Law Combining Fick's first law (Equation 2.15) and the continuity equation (Equation 2.17), Fick's second law can be derived, referred to as the diffusion equation^[55]

$$\frac{\partial C}{\partial t} = \nabla \cdot (D \nabla C). \quad (2.18)$$

This equation relates the accumulation or depletion of concentration over time to the curvature of the concentration gradient. If the diffusivity D is independent of the concentration, for example for diffusion in ideal solid solutions, the equation can be expressed more simply as^[55]

$$\frac{\partial C}{\partial t} = D \nabla^2 C. \quad (2.19)$$

2.2.2 Solid State Diffusion

Diffusion in gases can be described as free flights of atoms or molecules, which are interrupted by its collisions. In liquids, the atomic or molecular motion is more subtle and resembles random shuffles, each much smaller than the average spacing of atoms or molecules in the liquid. In solids, especially in crystalline solids, the

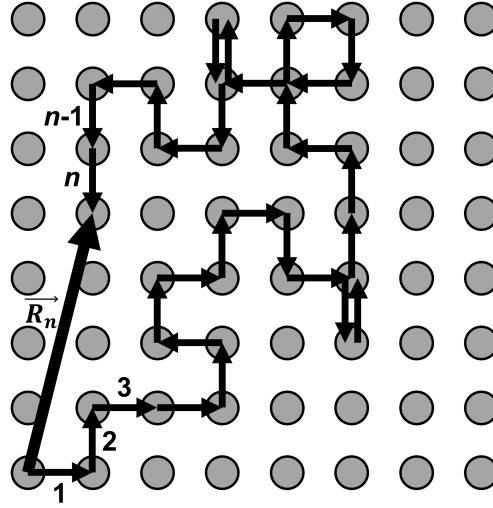


FIGURE 2.8: Example of a random walk sequence with n jumps, with individual jump vectors \vec{r}_i , and a total displacement \vec{R}_n . Adapted with permission from Mehrer, H., *Diffusion in Solids*, 1st ed.; Springer-Verlag: Berlin, Germany, 2007; p 60.^[55] Copyright Springer-Verlag 2007.

motion of atoms occurs by hopping from one lattice site to another. The timescales of these atomic hops are very different from the time between one hop to the next, which leads to the macroscopic observation of diffusion.

The diffusion of an atom in a lattice can be considered a random walk. In a lattice with coordination number Z , each jump direction occurs with a probability of $1/Z$, with a jump length usually equal to the nearest-neighbor distance in the lattice. The total displacement \vec{R} of an atom is equal to the sum of all individual jumps an atom took on its path through the lattice, as depicted in Figure 2.8,^[55]

$$\vec{R} = \sum_{i=1}^n \vec{r}_i \quad (2.20)$$

with the individual jump vectors \vec{r}_i . Assuming the diffusing atom has no memory of the previous jump, the sequence of jumps is considered an uncorrelated random walk, referred to as a Markov sequence. The average displacement can then be expressed as^[55]

$$\langle \vec{R}^2 \rangle = \sum_{i=1}^n \langle r_i^2 \rangle. \quad (2.21)$$

Assuming, that in a crystal with coordination number Z , only nearest-neighbor jumps with a jump length of d are possible, Equation 2.21 reduces to^[55]

$$\langle \vec{R}^2 \rangle = \langle n \rangle d^2 \quad (2.22)$$

with the average number of jumps of an atom $\langle n \rangle$. The jump rate Γ with which a jump of an atom to one of the Z neighboring lattice sites occurs can be expressed

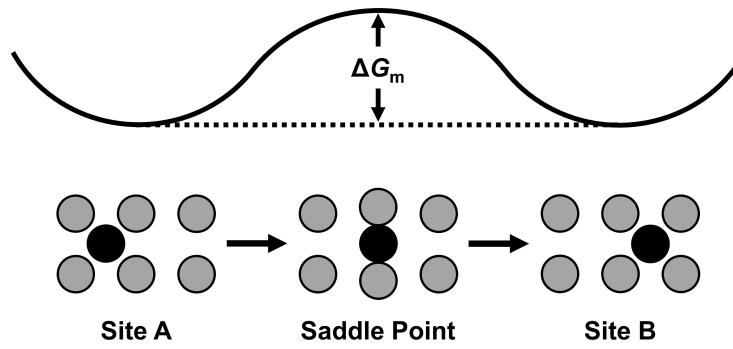


FIGURE 2.9: Atomic jump in a crystalline solid (grey spheres) of an atom (black sphere) from its initial position at lattice site A, through a saddle point, to lattice site B; with an energy barrier height of the saddle point of ΔG_m . Adapted with permission from Mehrer, H., *Diffusion in Solids*, 1st ed.; Springer-Verlag: Berlin, Germany, 2007; p 64.^[55] Copyright Springer-Verlag 2007.

as^[55]

$$\Gamma \equiv \frac{\langle n \rangle}{Zt}. \quad (2.23)$$

By comparison with Fick's first law the diffusion coefficient is obtained^[55]

$$D = \frac{1}{6}d^2Z\Gamma = \frac{d^2}{6\tau} \quad (2.24)$$

with the mean residence time of an atom on a certain lattice site $\tau = 1/Z\Gamma$. For example, a face-centered cubic lattice with lattice constant a has the coordination number $Z = 12$ and a jump length of $d = a\sqrt{2}/2$. In this case, Equation 2.24 would give $D = 12\sqrt{2}\Gamma$.^[55]

The atomic jump from one atom to a neighboring site, either a vacancy or interstitial site, requires the jumping atom to squeeze between surrounding atoms, inhibiting the jump. The energies necessary to promote a jump are usually higher than the available thermal energy of $k_B T$. At these temperatures, atoms oscillate around their lattice positions. Only occasionally will large displacements result in a successful jump of the diffusing atom. The nature of these activation events is infrequent in relation to the lattice vibrations. After one successful jump, the activated atom becomes unactivated again, until another activation event occurs, resulting in a series of discrete jumps. The jump rate depends on the Gibbs free energy of migration ΔG_m , which is the difference between the energy of the saddle-point barrier and the equilibrium position of the diffusing atom (see Figure 2.9) and can be expressed as^[55]

$$\Gamma = \nu_0 \exp\left(-\frac{\Delta G_m}{k_B T}\right) \quad (2.25)$$

with the attempt frequency ν_0 , which is of the order of the Debye frequency of the lattice, with typical values in the range of 10^{12} s^{-1} to 10^{13} s^{-1} . Equation 2.25 is characteristic for an Arrhenius-type dependence on temperature.^[55]

The hopping of solute atoms in a crystal lattice are universal for the diffusion

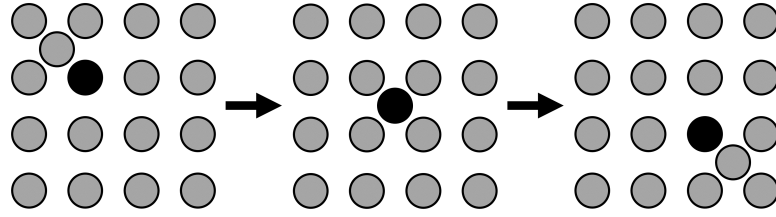


FIGURE 2.10: The interstitialcy mechanism, illustrated by a collinear jump of a self-interstitial atom A_i , and a solute atom B (black sphere); the solute atom alternates between occupying a substitutional lattice site B_s and an interstitial site B_i . Adapted with permission from Mehrer, H., *Diffusion in Solids*, 1st ed.; Springer-Verlag: Berlin, Germany, 2007; p 101.^[55] Copyright Springer-Verlag 2007.

process. However, many mechanisms are possible for the motion of atoms, some of which will be introduced in the following. The simplest form of diffusion is the direct interstitial mechanism. Small solute atoms, e.g. H, C, N, and O, compared to larger solvent atoms of the crystal lattice, can occupy interstitial sites of the host lattice and diffuse by jumping from one interstitial site to a neighboring one. The geometry of the interstitial site depends on the host lattice. For example, in a face-centered cubic lattice the solute atoms can occupy octahedral and tetrahedral sites. In case of the direct interstitial mechanism, the diffusion is independent of any defects in the lattice and the activation energy for diffusion is independent of any defect formation energies.^[55]

The indirect interstitial mechanism, also referred to as the interstitialcy mechanism, has an interstitial atom as the diffusion-mediator. Here, a solute atom B (black sphere in Figure 2.10) occupies a lattice site of the host lattice A (grey spheres), called a substitutional site B_s . An extra atom of the matrix atom species A occupies an interstitial position, referred to as a self-interstitial A_i . This self-interstitial atom moves in unison with the solute atom B and replaces it on the lattice site, so that the solute atom now occupies an interstitial site B_i *et cetera*. This is a collective mechanism, as at least two atoms move simultaneously.^[55]

Yet, the dominant diffusion mechanism in metals for matrix atoms, as well as for substitutional solute atoms, is the vacancy mechanism. Here, an atom moves through the lattice by exchanging positions with a neighboring vacancy, as illustrated in Figure 2.11. This is a thermally induced effect, as the concentration of monovacancies C_{1V} depends on the temperature^[55]

$$C_{1V} = \exp\left(-\frac{G_{f,1V}}{k_B T}\right) \quad (2.26)$$

with the Gibbs free energy of a monovacancy formation $G_{f,1V}$. The exchange jump rate Γ_{ex} of a vacancy-mediated jump is then^[55]

$$\Gamma_{\text{ex}} = \omega_{1V} C_{1V} \quad (2.27)$$

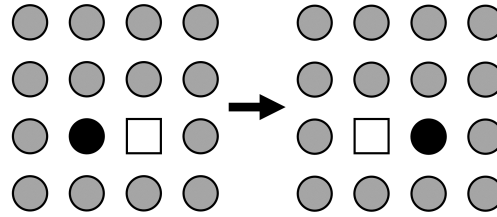


FIGURE 2.11: Monovacancy diffusion mechanism, in which a solute atom B (black sphere) changes position with a vacancy V (white square). Adapted with permission from Mehrer, H., *Diffusion in Solids*, 1st ed.; Springer-Verlag: Berlin, Germany, 2007; p 99.^[55] Copyright Springer-Verlag 2007.

with the exchange rate between an atom and a vacancy ω_{1V} . The total jump rate $\Gamma_{\text{ex,tot}}$ again depends on the amount of neighboring atoms, given by the coordination number Z , with $\Gamma_{\text{ex,tot}} = Z\Gamma_{\text{ex}}$.^[55]

Some solvent lattices may allow for the solute atoms to either occupy interstitial or substitutional sites, called hybrid solutes. In this case, solute atoms can diffuse *via* one of the interstitial-substitutional exchange mechanisms, illustrated in Figure 2.12. Usually, the diffusivity of solute atoms is much higher in the interstitial configuration. Yet, the solubility of the solute atoms in the host lattice in the interstitial configuration is much lower compared to the substitutional state.^[55] Therefore, solute atoms may diffuse rapidly *via* interstitials as B_i , and change over to the substitutional state B_s to be incorporated into the host lattice. The incorporation into the host lattice can occur by occupying a vacancy V according to^[55]



This is denoted as the dissociative mechanism. In case the incorporation into the host lattice involves the creation of a self-interstitial A_i , it is referred to as the kick-out mechanism, since the incorporation of the solute atom leads to the displacement of a lattice atom^[55]



The dominant diffusion mechanism in metals has been introduced as vacancy-mediated, which is also true for semiconductors. Although, due to their strong covalent bonding character, semiconductors exhibit relatively high formation enthalpies of point defects, such as vacancies and self-interstitials. Thus, the amount of point defects in thermal equilibrium are orders of magnitude lower in semiconductors, compared to metals.^[55] Furthermore, some crystal structures, i.e. diamond and zinc blende, favor the incorporation of solute atoms *via* interstitials. As a consequence, interstitial diffusion and interstitial-substitution exchange diffusion (dissociative and kick-out mechanism) are more common in semiconductors than in metals.^[55]

In ionic compounds, a cationic lattice site can form a self-interstitial and a cation vacancy. This disorder is referred to as Frenkel disorder, and a pair of self-interstitial and cation vacancy is called a Frenkel pair.^[55]

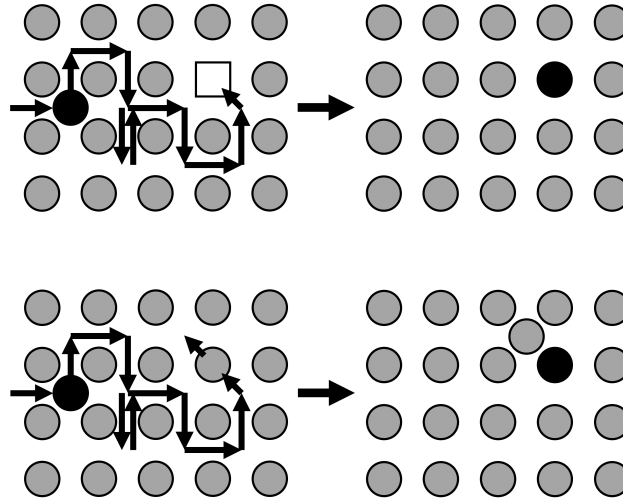


FIGURE 2.12: The two possible interstitial-substitutional exchange mechanisms with the initial conditions on the right with a solute atom in an interstitial position B_i (black sphere), moving through a lattice of A atoms (grey spheres): on top, the dissociative mechanism, in which an interstitial atom B_i occupies a vacancy, and on the bottom, the kick-out mechanism, in which the solute atom occupies a lattice site, creating a self-interstitial A_i ; both mechanisms result in a substitutional solute B_s . Adapted with permission from Mehrer, H., *Diffusion in Solids*, 1st ed.; Springer-Verlag: Berlin, Germany, 2007; p 103.^[55] Copyright Springer-Verlag 2007.

2.2.3 Cation Exchange

In ionic crystals, anions are usually larger than cations due to their valence electrons. As a consequence, anions have lower diffusivities than cations. The rigid anionic sublattice allows guest cations to enter the host lattice and exchange cations thereof.^[26] A successful CE reaction is characterized by a topotactic transformation, in which the anionic framework is maintained, and the initial crystal morphology is retained.^[23]

A CE reaction with a host lattice AC, consisting of anions A^- and cations C^+ , exposed to a solution of guest ions X^+ can be written as^[23]



For simplicity, this describes an isovalent system, in which one monovalent cation is exchanged for another; though non-isovalent systems are possible as well.^[23] The thermodynamics of such a CE reaction can be split into four elemental steps^[26]



The dissociation and association energies of Equations 2.31 and 2.33 describe the

crystal energy, made up of the lattice and surface energies. Equations 2.32 and 2.34 describe the desolvation of the guest ion and solvation of the host ion in the reaction solution.^[26] The energy balance of the four partial reactions dictates whether a CE reaction is probable. If the host cation is solvated more strongly in the reaction solvent than the guest cation, the reaction is likely to proceed. The solvation energy usually has the highest impact on the total released energy of a reaction and is therefore the main driving force of a CE.^[23,26]

The affinities of different metal ions to solvents and ligands can be predicted with Pearson's concept of hard and soft acids and bases (HSAB theory).^[61] Acids and bases are divided into two categories: hard and soft. Hardness can be described as the "resistance to deformation or change."^[62] Lewis bases are divided into the two categories depending on their donor atoms. A donor atom with high polarizability and low electronegativity is easy to oxidize (soft base), while an atom featuring a low polarizability and high electronegativity is hard to oxidize, hence is characterized as a hard base.^[23,61] *Vice versa*, the characterization of a Lewis acid depends on the acceptor atom. A soft acid exhibits an acceptor atom with a low positive charge and a large size, whereas a hard acid has a high positive charge and a small size.^[23,61] The HSAB theory predicts the affinity of hard acids to hard bases, forming ionic compounds, while soft acids prefer soft bases, which result in compounds with covalent binding character.^[61] In order to quantify the hardness of various cations, ligands and solvents, Parr and Pearson introduced the concept of absolute hardness η in 1983.^[62] Guided by this theory, it is plausible that, for example, cations acting as soft acids, like Cu^+ with an absolute hardness of $\eta = 6.25$,^[63] can be exchanged by cations behaving as harder acids, like In^{3+} with an absolute hardness of $\eta = 13$,^[63] in the presence of ligands or solvents acting as soft bases, like tertiary phosphines ($\eta \approx 6$)^[64].

Due to the small size of NCs, the surface-to-volume ratio increase can lead to a substantial change in the thermodynamics and accelerate reaction kinetics of a CE.^[29] For instance, the CE with Ag^+ in CdSe was observed to be up to $100\times$ faster in NCs compared to the bulk.^[65]

Depending on the miscibilities of the host lattice and incoming cations, many outcomes of a CE reaction are possible. In case of a high miscibility, a small amount of guest cations can yield a homogeneous solution of guest ions in the host lattice, yielding doped NCs, while a high amount of guest ions can result in the formation of an alloy.^[23,26] In contrast, immiscibility of host lattice and guest ions can lead to the formation of a reaction zone on the surface of a NC, moving towards the center, resulting in a core/shell NHC.^[23,29] Besides core/shell NHCs, segmented NHCs can be formed, e.g. Janus particles^[66] or multi-segmented NHCs.^[32]

Chapter 3

Scope

The field of colloidal NC syntheses is well-established with a large body of work, especially for binary NC compositions.^[7,8,19,67–69] But due to the health risks associated to some elements of the II–VI and IV–VI classes of semiconductors, e.g. Cd, Hg and Pb,^[70,71] the potentially more environmentally friendly class of I–III–VI semiconductors was chosen as a subject matter. CuInS₂ represents an attractive alternative to semiconductors containing hazardous heavy metals (e.g. CdSe or PbTe) with similar optical properties and possible applications, e.g. as an absorber material for quantum dot or thin film photovoltaics, light-emitting devices and in bio-medical systems.^[72] However, the direct synthesis of such ternary NCs is still challenging, as reactivities of three precursor compounds need to be balanced to achieve control over the desired size, shape, composition and crystal structure. Copper sulfide NCs pose as ideal candidates for template structures, as they are thoroughly studied in literature,^[73–75] have an interesting and complex phase diagram,^[76,77] and can be produced in a wide range of sizes and morphologies.^[78,79] Copper sulfide NCs can then determine the size and shape acting as a template structure, which can be altered post-synthetically *via* cation exchange (CE), to produce the desired CuInS₂ NCs.

The aim of this project was to perform CE reactions with anisotropic rod-shaped Cu_{2-x}S NCs as templates, and produce CuInS₂ NRs, maintaining the template size and shape, characteristic of a successful CE. The scope of this work included the kinetic analysis of the CE reaction and set out to elucidate the reaction mechanism, especially in anisotropic NCs, and substantiate the findings with quantifiable values for the activation energy of the rate-limiting step of the reaction.

In order to comprehensively analyze the CE reaction and collect reliable data, a wide range of intermediate compositions at various temperatures below and above the phase transition temperature of the template Cu_{2-x}S NRs needed to be produced. With rigid and reproducible data the effect of the phase transition on the kinetics was to be studied.

The size and shape evolution during the CE reaction from Cu_{2-x}S to CuInS₂ was to be examined *via* transmission electron microscopy (TEM) and high-resolution transmission electron microscopy (HRTEM), the compositional evolution was to be tracked *ex situ via* energy-dispersive X-ray spectroscopy (EDX) measurements, and

the crystallographic changes were to be studied *via* X-ray powder diffraction (XRD).

A kinetic model was to be prepared from elemental composition data acquired *via* energy-dispersive X-ray spectroscopy (EDX).

Chapter 4

Cu_{2-x}S Nanocrystals as Starting Particles for Cation Exchange Reactions

Cation exchange reactions at the nanoscale can be studied based on many different systems. It is possible to start with a binary compound and exchange the cationic species to obtain a different binary compound. It is also possible to start with a ternary system, exchange one or two cationic species, and again obtain a ternary system. But it is also feasible to introduce a third cationic species into a binary compound, resulting in a ternary system. In case of the present work, the starting material is a binary copper sulfide compound. Indium is introduced during the cation exchange reaction, so that the product is a ternary copper indium sulfide.

The kinetics of such a reaction is not only influenced by the crystal structure, but also by the crystallite's size and form. By choosing an elongated NC shape, the kinetics in an anisotropic environment can be investigated. Even though a rod-like shape is thermodynamically less stable than a sphere, in conditions of high chemical potential, anisotropic shapes can be produced. By choosing weak stabilizing surface ligands like amines or *n*-thiols, one-dimensional growth of nanorods (NRs) can be promoted. In the here presented case, *tert*-dodecanethiol simultaneously acted as the sulfur source and as a stabilizing ligand for copper sulfide NRs. The thermal decomposition of *tert*-dodecanethiol during the growth reaction can either take place in solution, or on the surface of already formed NCs, which increases the reactivity and growth rate. With highly reactive facets perpendicular to the growth direction (Cu- or S-rich (100) facets), one-dimensional growth is strongly favored.^[80]

In the following chapter the Cu_{2-x}S NRs, used for CE reactions discussed in Chapter 5, are introduced. In order to claim comparability between CE experiments with different starting samples, it is necessary to establish that all batches of Cu_{2-x}S NRs are similar as well. If their sizes, compositions and crystal structures are comparable, it is reasonable to assume that the CE behavior is independent of the choice of starting sample.

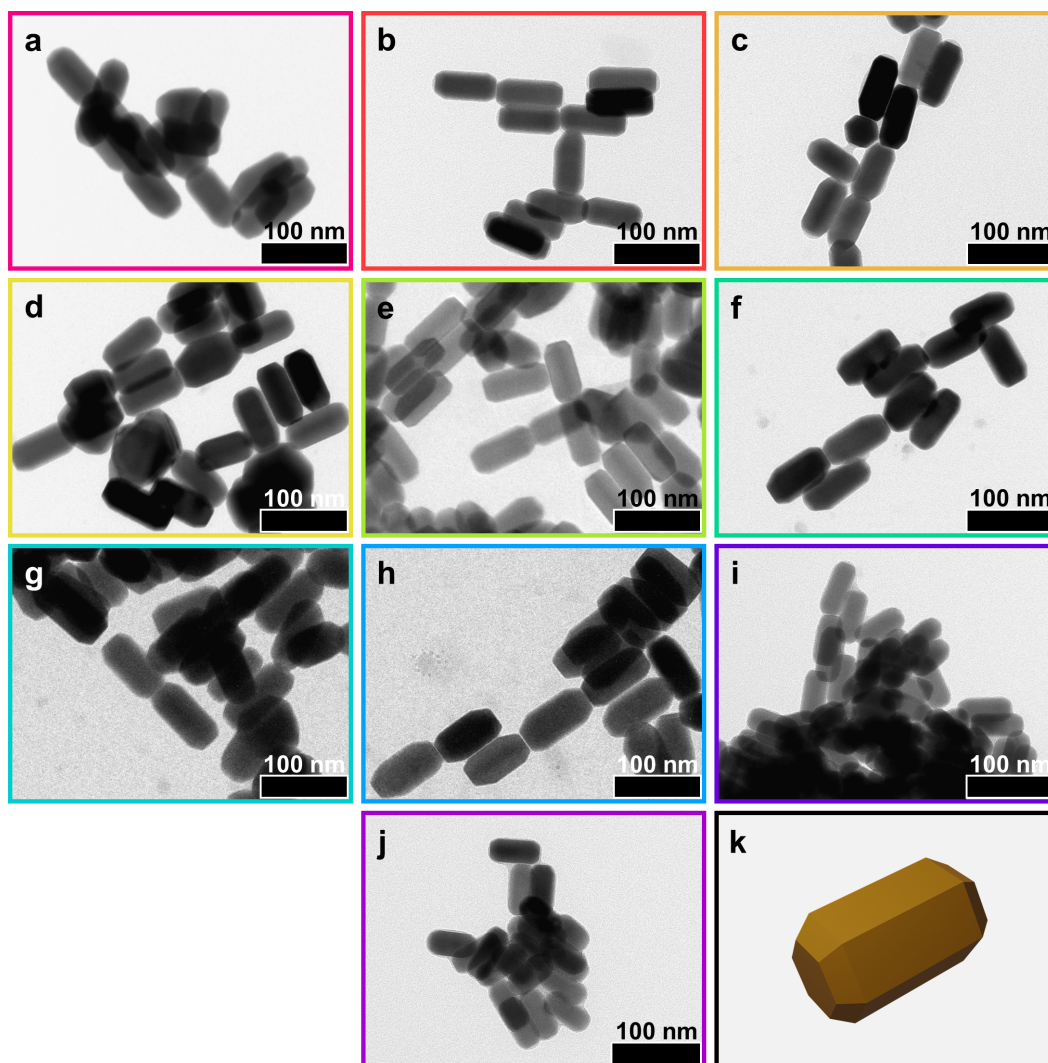


FIGURE 4.1: TEM micrographs of Cu_{2-x}S starting samples (a) 231018-A, (b) 291018-A, (c) 291018-B, (d) 160419-A, (e) 180520-B, (f) 050620-B, (g) 010621-A, (h) 010621-B, (i) 270921-A, (j) 270921-B, and (k) a rendered three-dimensional representation of the typical NR shape.

4.1 Permanent Properties: Morphology, Composition and Crystal Structure

All Cu_{2-x}S NR starting samples for subsequent CE reactions have been prepared in a one-pot thermal decomposition approach. The synthetic protocol was adapted from a hot injection synthesis demonstrated by Kruszynska *et al.*^[80] (see Chapter 7.1 for the experimental details).

Combining copper(I)acetate with *tert*-dodecanethiol in 1-octadecene as the solvent and Cyanex as an additional ligand yielded NCs with a rod-like shape. Figures 4.1a–j show transmission electron microscopy (TEM) micrographs of all Cu_{2-x}S samples used for the CE reactions discussed in Chapter 5. The NRs were homogeneous in size over individual sample batches and in shape over all batches. The typical

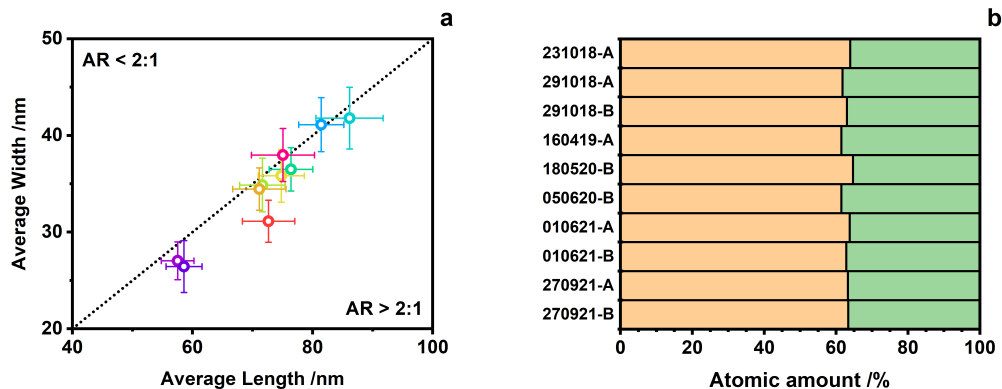


FIGURE 4.2: (a) Average sizes of all NR samples, in corresponding colors to Figure 4.1 (the individual size distributions with respect to each individual data point are presented in the appendix in Figure A.1); the dashed black line denotes an AR of 2 : 1 (samples with an AR above 2 : 1 are below the dashed line and *vice versa*). (b) Depiction of the average atomic compositions of all individual Cu_{2-x}S NR samples, obtained by EDX measurements in a scanning electron microscopy (SEM), with atomic amounts of Cu in orange and S in green.

shape was a hexagonal prism with truncated corners on both ends of the NR, depicted in the rendered image in Figure 4.1k

All NR samples exhibited similar aspect ratios (ARs) between 2.0 : 1 and 2.3 : 1, with an arithmetic mean (hereinafter referred to as mean or average) of $2.1 \pm 0.1 : 1$ (length to width). The dotted black line in Figure 4.2a represents the exact AR of 2 : 1 and illustrates the similarity of ARs over all NR samples. The NRs of sample 270921-A had the smallest average size with a length of 58.6 ± 3.0 nm and width of 26.4 ± 2.7 nm. The NRs with the largest average size have been produced in sample 010621-A with a length of 86.1 ± 5.6 nm and width of 41.8 ± 3.2 nm. Even though the sizes between the smallest and largest sample batches differed slightly, no strongly varying results were to be expected as a consequence: Zhao *et al.* calculated the exciton Bohr radius in Cu_{2-x}S , assuming that the relative dielectric constant ϵ is about 10 to 15, to 3–5 nm.^[81] This is well below the dimension of all NR sample batches.

In addition to the similarity of all starting sample batches in crystallite size, all NR samples exhibited similar ratios of Cu to S (see Figure 4.2b). All samples were under-stoichiometric with a slight Cu-deficiency, with compositions close to stoichiometric Cu_2S with 66 atomic percent (hereinafter referred to as %) and 33% S. In such a crystal phase Cu would have an oxidation number of +1 and S of -2.

With a complex phase diagram of the Cu–S system, numerous crystal phases came into consideration to match the diffraction data of the presented Cu_{2-x}S samples.^[76] A representative starting sample (270921-B) is shown in Figure 4.3 with six possible X-ray powder diffraction (XRD) reference patterns. The diffraction data set in Figures 4.3a–b are depicted with the stoichiometric Cu_2S phases of high and low chalcocite. These reference data sets did not match the main reflections of the experimental data. The reference reflections were shifted to smaller values of 2θ , especially in reference to the reflections with the highest measured intensities at

37.6° , 46.4° and 48.7° . Therefore, these references did not model the experimental data well. The reference patterns shown in Figures 4.3e–f represent two understoichiometric Cu_{2-x}S phases with digenite $\text{Cu}_{1.8}\text{S}$ and anilite $\text{Cu}_{1.75}\text{S}$. Even though the reflection at 46.4° was well matched by the digenite and anilite pattern with 46.2° and 46.4° , respectively, no reference reflection corresponded to the highest measured intensity reflection at 48.7° . Moreover, many reflections of the references, e.g. at 27.8° and 32.2° for digenite and 27.9° and 32.3° for anilite, were not present in the measured diffractogram. In contrast, reference reflections of the slightly less understoichiometric phases of djurleite $\text{Cu}_{1.94}\text{S}$ and roxbyite $\text{Cu}_{1.81}\text{S}$ in Figures 4.3c–d described the measured data to a higher degree. While most reflections of the reference data set of roxbyite were in reference to the measured reflections, many were shifted towards larger values of 2θ . The best model of the experimental data was achieved by the reference pattern of djurleite, which matched the main reflections at 37.6° , 46.4° and 48.7° closely with 37.6° , 46.3° and 48.7° . The crystal structure of djurleite has been solved by Evans in the space group $\text{P}2_1/n$ with a monoclinic cell ($a = 26.897 \text{ \AA}$, $b = 15.745 \text{ \AA}$, $c = 13.565 \text{ \AA}$, $\beta = 90.13^\circ$), containing 248 Cu atoms and 128 S atoms.^[82]

Figure 4.4 demonstrates that all starting samples exhibited similar diffraction patterns. Sample 231018-A was an exception with a double peak at 46.4° and 46.9° and a peak at 49.0° , which was shifted to larger values of 2θ compared to the reference reflection of djurleite at 48.7° . Therefore, this sample is more aptly described by the reference pattern of roxbyite $\text{Cu}_{1.81}\text{S}$. Even though roxbyite is slightly more Cu-deficient than djurleite, both crystal phases are comparable, since roxbyite has a "structure [that] has Cu in coordinations very similar to those of djurleite and low chalcocite. . ."^[83] The remaining samples were in accordance to the reference diffraction pattern of djurleite and featured similar reflection positions and intensity ratios. The djurleite reference reflections highlighted by the extended light grey lines in Figure 4.4 emphasize this and correspond to the highest intensities of the measured reflection patterns.

In summary, all prepared NC samples shared the same rod-like morphology with ARs close to 2.1 and had comparable sizes, well over the confinement regime. Additionally, samples had similar Cu-deficient compositions, which were in agreement to the determined reference diffraction pattern of djurleite. Due to the homogeneity of the presented starting samples, it was assumed that an individual starting sample would not affect the outcome of an experiment when compared to another experiment with the same parameters and a different starting sample. The results suggest that CE experiments with the presented starting samples would be universally comparable among each other.

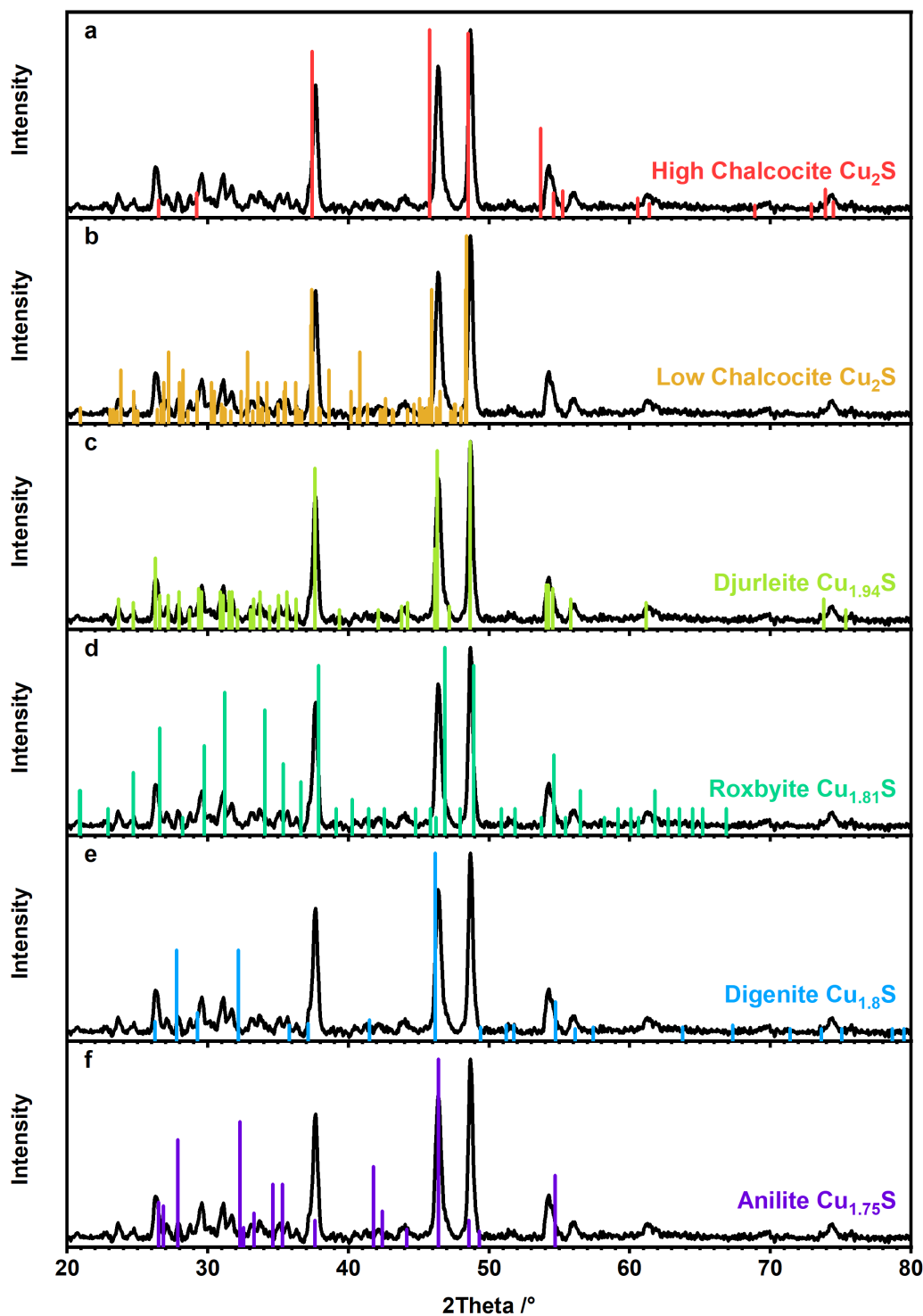


FIGURE 4.3: Comparison of reference diffraction data sets of stoichiometric and under-stoichiometric copper sulfide phases from the ICDD to match a representative Cu_{2-x}S NR sample (270921-B). (a)–(f) All show the same diffractogram of sample 270921-A, with the reference patterns of (a) high chalcocite Cu_2S (PDF no. 00-026-1116), (b) low chalcocite Cu_2S (PDF no. 00-033-0490), (c) djurleite $\text{Cu}_{1.94}\text{S}$ (PDF no. 00-023-0959), (d) roxbyite $\text{Cu}_{1.81}\text{S}$ (PDF no. 00-023-0958), (e) digenite $\text{Cu}_{1.8}\text{S}$ (PDF no. 00-047-1748) and (f) anilite $\text{Cu}_{1.75}\text{S}$ (PDF no. 00-022-0250).

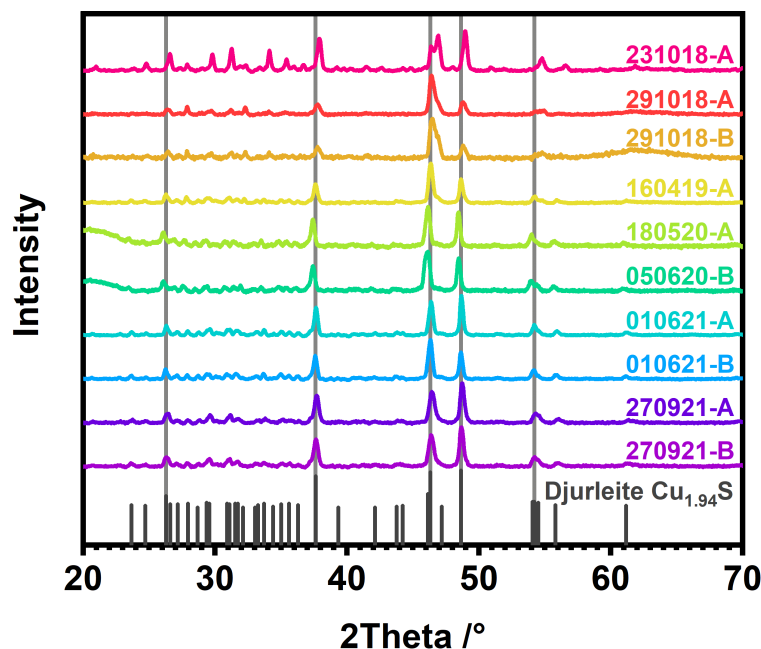


FIGURE 4.4: Comparison of all Cu_{2-x}S starting samples with the diffraction reference pattern of djurleite $\text{Cu}_{1.94}\text{S}$ (PDF no. 00-023-0959) in grey; with some characteristic reflections extended in a lighter grey at 26.3° , 37.6° , 46.3° and 48.7° , corresponding to the planes with Miller indices of (800), (804), (080) and (1204), respectively.

4.2 Impermanent Properties: Thermal Stability, Oxidative Decay and Aging

Djurleite has a lower symmetry than the stoichiometric Cu_2S high chalcocite phase. However, both phases have a hexagonally close-packed anionic S sublattice^[84] and it has been reported that (bulk) djurleite undergoes a phase transition at 93°C to a mixture of high digenite and high chalcocite.^[76,82,85,86] The high chalcocite phase is described as a solid-liquid hybrid phase^[87] due to an unusually high diffusion coefficient of Cu cations in a rigid anionic S lattice.^[88,89]

In order to investigate the temperature-dependent crystal properties on a nano-scaled system, a liquid djurleite NR sample in a sealed capillary was heated from room temperature to 50°C , 100°C , 150°C and 200°C and cooled back down to room temperature again. Figure 4.5 shows the *in situ* XRD measurements, which revealed a phase transition from djurleite to a mixture of djurleite and high chalcocite. At 50°C no shifts of reflection positions could be observed. A shifting onset towards smaller values of 2θ was noticeable, e.g. around 46° and 48° , at 100°C . With higher temperatures, at 150°C , a splitting of reflection peaks was apparent, which could be attributed to reference reflections of djurleite and high chalcocite, indicating the existence of djurleite and high chalcocite as two distinct crystal phases. The peak splitting was even more pronounced at 200°C . Here, clear double peaks could be

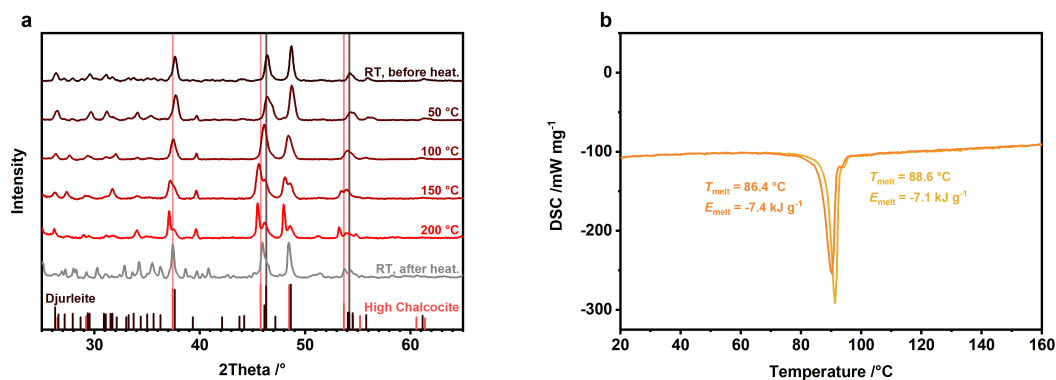


FIGURE 4.5: (a) *In situ* temperature-dependent XRD patterns of a djurleite NR sample, heated from room temperature (RT, before heating) to 200 °C, and cooled down to room temperature again (RT, after heating); with reference patterns of djurleite (PDF no. 00-023-0959) in dark brown, with lines extending two distinct reflections at 46.3° and 54.2° with Miller indices of (080) and (880), respectively, and the stoichiometric Cu₂S phase high chalcocite (PDF no. 00-026-1116) in light red, with lines extending three distinct reflections at 37.4°, 45.8° and 53.7° with Miller indices of (102), (110) and (112). (b) Two cycles of DSC measurements of the djurleite NR sample 080222-B (sample properties can be found in Appendix A.1.2) to investigate T_{pt} ; shown are the second and third measurements in orange and yellow, respectively, with the obtained melting temperatures and energies thereof.

observed around 37° and 38°, 45° and 47° and 48° and 49°, supporting the hypothesis of two distinct crystal phases of djurleite and high chalcocite over the phase transition temperature (T_{pt}). It should be noted, that diffractograms as a whole shifted towards smaller values of 2θ as a result from the heating during the *in situ* measurement. After the sample was cooled down to room temperature again, the double peaks disappeared and reflections shifted back close to the initial positions, indicating a reversible process. Presumably, this phase transition, accompanied by the emergence of a solid-liquid hybrid structure with a high diffusion coefficient of Cu in high chalcocite,^[87–89] also occurred during the injection of the NR suspension into the reaction solution to initiate any given CE reaction. The exact temperature of the phase transition was investigated further by differential scanning calorimetry (DSC) measurements. A djurleite NR sample was heated from 20 °C to 160 °C repeatedly and the phase transition temperatures were determined to 86.4 °C and 88.6 °C, with a mean T_{pt} of 87.5 ± 1.1 °C, corroborating the aforementioned XRD measurements.

In order to further evaluate the stability of the starting samples, batch 180520-B was split: One part was kept in a nitrogen-filled glovebox as a control sample, while the other part was exposed to ambient conditions over a period of eleven weeks. The crystal structure evolution was evaluated *via* regular XRD measurements. The diffraction pattern in Figure 4.6a was still in accordance to the reference pattern of djurleite after one day of ambient atmosphere exposure. However, after one week of continued exposure, the emergence of a shoulder at 46.6° became evident. The shoulder increased in intensity, relative to the (080) reflection of djurleite at 46.3°, with continued exposure. In contrast, the (1204) reflection at 48.7° decreased in intensity. Figure 4.6c shows the diffractograms of the exposed sample in red and

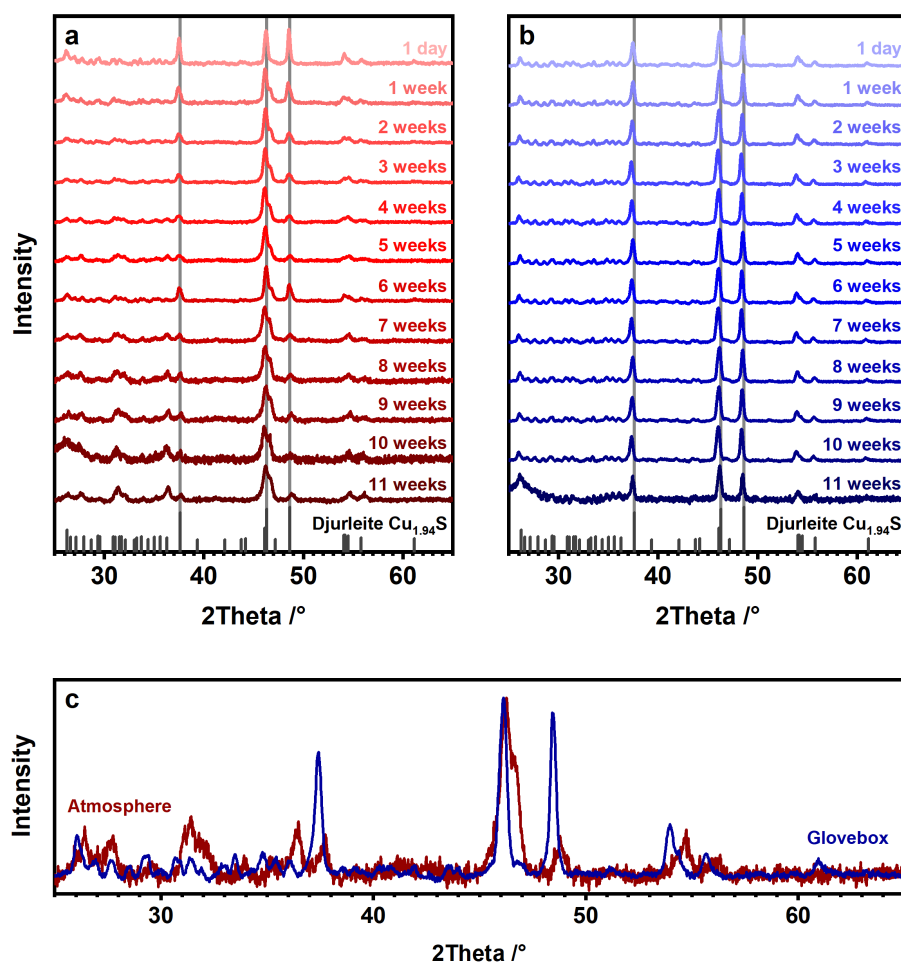


FIGURE 4.6: Evolution of diffraction patterns in sample 180520-B over the course of eleven weeks due to (a) atmosphere exposure of the stirred colloidal NR suspension in an open vial and (b) the control experiment with the same sample stirred in a nitrogen-filled glovebox, with the reference reflection pattern of djurleite (PDF no. 00-023-0959) in grey and lighter grey lines extending three distinct reflections at 37.6° , 46.3° and 48.7° with Miller indices of (804), (080) and (1204). (c) The diffraction patterns from (a) and (b) after nine weeks in direct comparison to illustrate the changes in the diffractogram of the sample exposed to ambient conditions, e.g. the emergence of a shoulder at 46.5° .

the glovebox-stored sample in blue after nine weeks in greater detail, and thus illustrates the differences further: Reflection positions of the exposed sample are shifted to larger values of 2θ , when compared to the control experiment. The emergence of new reflections and the shifting of existing ones was not observable in the control experiment in 4.6b. Reflection positions in the diffractograms did not change considerable over the course of eleven weeks, and the intensity ratios remained consistent as well. As a consequence, all starting sample batches were stored in a nitrogen-filled glovebox and handled under Schlenk-conditions to ensure that no exposure to ambient atmosphere would occur.

Chapter 5

Cation Exchange

The CE reaction from Cu_{2-x}S to CuInS_2 was studied in elongated NRs. In regard to the mechanism of CE reactions, some fundamental questions are still not fully answered and could be better pursued in an anisotropic system: Do precursor molecules have different affinities to the various crystallographic facets on the NC surface? Is ion transport to the surface a rate-limiting factor, the rearrangement on the surface or the ion-diffusion inside the NCs? Is the ion-diffusion inside the NC isotropic or affected by the crystallography of the system?^[90]

Time and temperature were the two parameters to control the CE reactions, discussed in Section 5.1 on the insights gathered from this specific reaction, while the conclusions thereof are discussed further in Section 5.2 in order to analyze the kinetics and to propose a reaction mechanism. The crystal phase transition temperature (T_{pt}) of the starting material djurleite will be of particular interest to explain the reaction kinetics. In its first part, Section 5.3 on special conditions for the CE reaction addresses this specific temperature region, while the second part introduces UV light as a third reaction parameter to further manipulate the reaction.

It should be noted, that some data discussed hereinafter was also subject to the publication of the author and colleagues, published in 2023 in the Journal ACS Nano.^[91]

5.1 Insights into the Cation Exchange Reaction

Key to a successful CE reaction is the size and shape retention of the starting crystallites. Assuming the exchange is limited to only the cations, the change to the size and morphology is expected to be minor, since the anionic part of the starting NCs should remain relatively stable over the period of the reaction. The morphology evolution of a CE reaction at 40°C , i.e. below the phase transition temperature (T_{pt}) of djurleite, is shown in Figure 5.1. The starting sample (Figures 5.1a–b) exhibited the typical rod-like and faceted shape, as described in Section 4. Additionally, samples after one week (Figures 5.1c–d) and two weeks (Figures 5.1e–f) are shown, with 1.7% and 2.6% In incorporated, respectively. Generally, the NR shape was retained in both samples, but the surface roughness increased with reaction time. After two

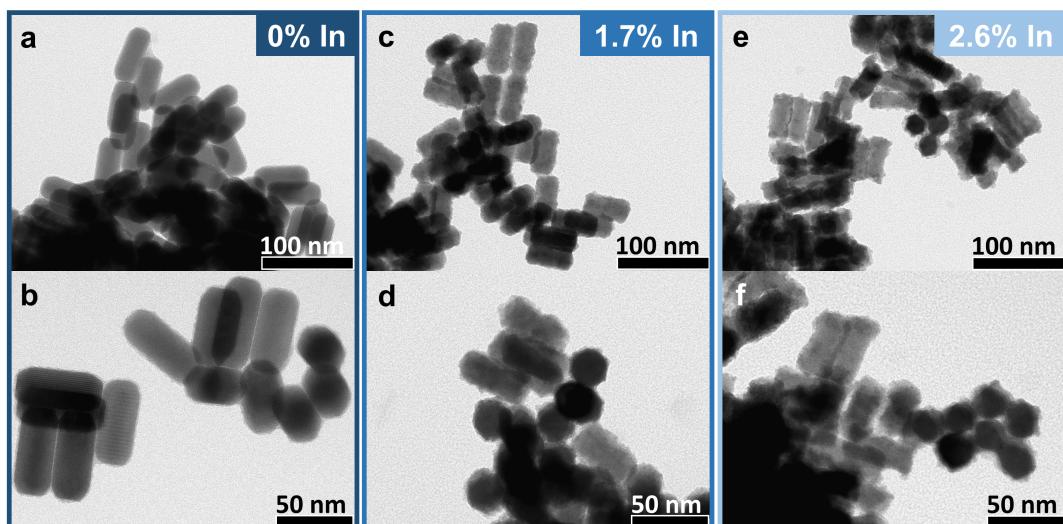


FIGURE 5.1: TEM micrographs of (a–b) the Cu_{2-x}S starting sample 270921-A for a CE reaction at 40°C with reaction times of (c–d) seven days with 1.7% In incorporation and (e–f) fourteen days with 2.6% In incorporation.

weeks of continued exposure to the In precursor in the reaction solution, small islands became visible on the surface, which could originate either from depositions of incoming In or outgoing Cu.

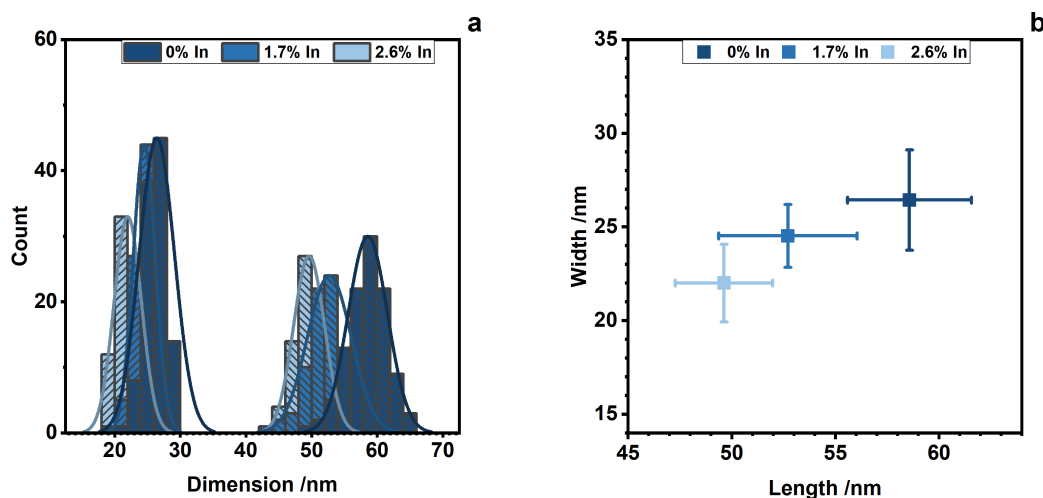


FIGURE 5.2: (a) size distribution histograms of the CE reaction at 40°C and (b) the mean sizes of those three samples, all in corresponding colors to the same samples shown above in figure 5.1.

The size distributions of these samples are shown in Figure 5.2. NRs considerably diminished in length and width over the reaction time of two weeks. The size decreased about 15.4% in length and 16.7% in width, from a length of 58.6 ± 3.0 nm and a width of 26.4 ± 2.7 nm before the exchange to a length of 49.6 ± 2.4 nm and a width of 22.0 ± 2.1 nm after fourteen days. An even decrease in particle length and width with regard to the minor In incorporation over the extended reaction time suggests either an unbalanced in- and out-flux of ions, or the etching of NRs due to

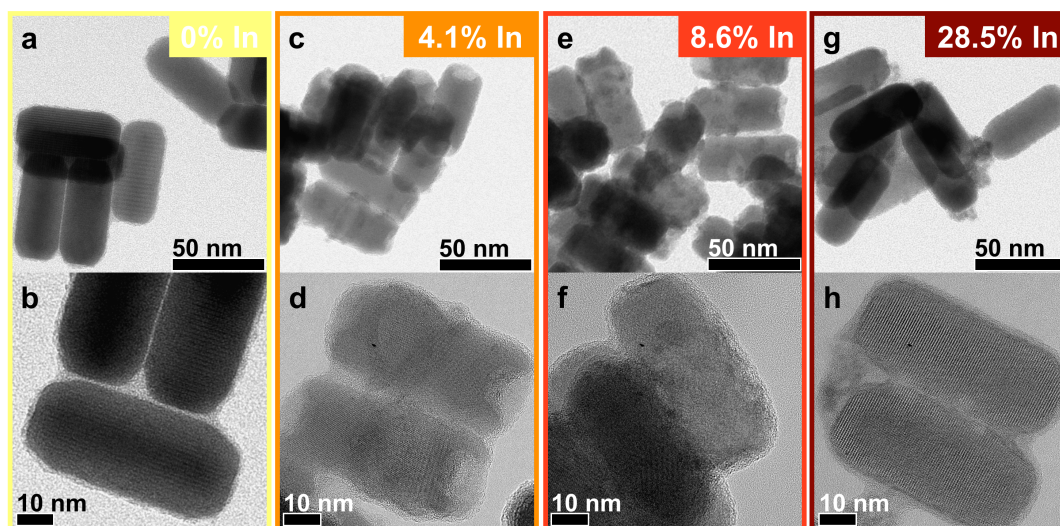


FIGURE 5.3: TEM micrographs of a CE reaction at 120 °C with (a–b) the starting sample 270921-A, two intermediate samples with a reaction time of (c–d) 3 min and (e–f) 5 min, and a fully exchanged sample after 60 min of reaction time, with the respective In incorporation from EDX data in the top right corners.

the presence of trioctylphosphine (TOP) in the reaction solution. Even though TOP is needed as a Cu extractant, if more Cu ions are extracted than In ions are incorporated into the lattice, particles could shrink over time as a result.

The morphology evolution of a CE reaction at 120 °C, above T_{pt} of djurleite, is shown in Figure 5.3. After 3 min of reaction time, already 4.1 % In has been incorporated into the NRs, and 8.6 % after 5 min. Similar to the reaction at 40 °C, below T_{pt} , the surface roughness increased. Further, it seems that the tips of the NRs have been hollowed out partially, especially visible in Figure 5.3d. Small depositions in the form of islands on the surface could be observed as well, apparent in Figure 5.3e. In contrast to the CE reaction below the phase transition temperature, a full CE was achieved with 28.6 % In. Surprisingly, the faceting of the starting sample returned after the full CE was reached and the surface roughness vanished. Here, the morphology was comparable to that of the starting sample. While the caveats at the tips of the NRs disappeared after the full exchange, it could still hint at unbalanced in- and out-fluxes of the incoming and outgoing ionic species. Alivisatos *et al.* discussed the necessary regimes for the Kirkendall effect, i.e. hollowing of NCs,^[92] and Mu *et al.* documented this for hollow CuInS₂ nanodisks.^[93] They stated, that surface ligands must be displaced in order to adsorb the In precursor species, which acts as an energetic barrier for the exchange process. This energy barrier can inhibit the in-diffusion of In ions into the NC and lead to a higher out-diffusion rate of Cu ions in respect to the in-diffusion of In ions. The size evolution can indicate, whether the in- and out-diffusion rates were in balance during a CE reaction.

Figure 5.4 shows that NRs decreased in length and width, but not to the same degree as after one or two weeks at 40 °C (see Figure 5.2). NRs decreased in length from 58.6 ± 3.0 nm before the exchange to 55.3 ± 3.0 nm after 24 h reaction time and

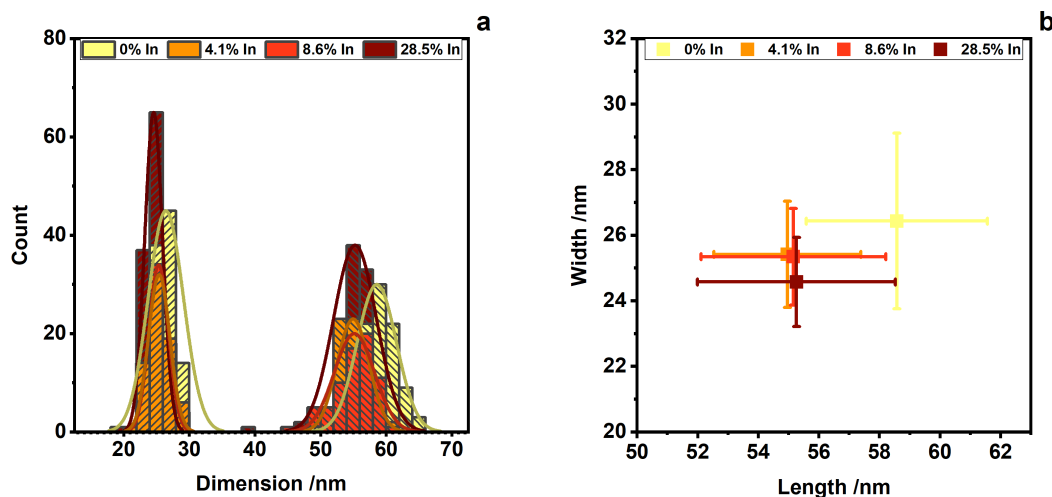


FIGURE 5.4: (a) Size distribution histograms of the CE reaction at 120 °C and (b) the mean sizes of these samples, all in corresponding colors to the samples shown above in Figure 5.3.

from 26.4 ± 2.7 nm to 24.6 ± 1.4 nm in width after the CE. This is equal to a decrease in length of 5.6% and in width of 6.8%, respectively. In part, this size decrease can be explained by a lattice compression during the reaction. Along djurleite's growth direction, its a -axis, the anionic sublattice is made up of S^{2-} layers with a distance of 3.36 Å.^[82] Djurleite's a -axis, coinciding with the wurtzite $CuInS_2$ c -axis, has to compress by 4.2% to match the S^{2-} layer distance of 3.22 Å.^[94] This matches the observed decrease in length of 5.6% well and supports the reduction in size due to a lattice compression. By approximating the amount of atoms per NR before the reaction and after the full exchange after 24 h the compression hypothesis could be supported. The amount of atoms per NR was calculated with the product of the amount of unit cells per NR and the amount of atoms per unit cell (the exact calculation can be found in Appendix A.2.1). It resulted in values of the same order of magnitude, with $2.1 \cdot 10^6 \pm 5.4 \cdot 10^5$ atoms before the exchange and $2.5 \cdot 10^6 \pm 4.4 \cdot 10^5$ after full exchange, corroborating the lattice compression hypothesis. However, the lattice compression along the b -axis from djurleite with 1.97 Å^[82] to 1.95 Å^[94] in wurtzite $CuInS_2$ only translates to a compression of 1.0%, which is not supported by the observed compression of 6.8%. A full exchange at 120 °C was reached already after 60 min, but the reaction was allowed to proceed for 24 h, to observe long-term effects of continued exposure to heat and the In precursor in the reaction solution. These long-term effects on the particle size can be seen in Figure 5.4b. Even though the particle length decreased initially, it remained stable over the depicted 24 h, concurrent with the hypothesized lattice compression, the particle width seemed to continually decrease over time. In addition to trioctylphosphine oxide (TOPO) in the form of the TOPO-InCl₃ precursor, TOP, a soft Lewis base with $\eta \approx 6$ eV,^[64] was present in the reaction solution to help extract Cu⁺ ions, a soft Lewis acid with $\eta = 6.25$ eV.^[63] While tips of the NRs are terminated with S^{2-} facets and relatively stable against TOP, the sides are terminated with both Cu⁺ and S^{2-} ions. With prolonged exposure

of the NRs to TOP and TOPO, an etching of the sides seems reasonable. In combination with the high diffusion rate of Cu^+ ions, it seems likely that additional Cu had been extracted after the CE was completed, resulting in further width decrease over prolonged exposure to the etching species in the reaction solution, as well as a slight Cu-deficiency in the fully exchanged NRs.

Here, an exchange is considered to be complete, if the atomic composition of the exchanged CuInS_2 NRs is close to the stoichiometric ratio of 25 % Cu, 25 % In and 50 % S. Further evidence to support the claim of full CE of the samples with stoichiometric (or In-rich) CuInS_2 compositions with a wurtzite structure, was the determination of the band gap energy E_g . The Tauc method assumes that the energy-dependent absorption coefficient \mathcal{A} can be expressed as^[95]

$$(\mathcal{A} \cdot h\nu)^{1/f} = \mathcal{B} (h\nu - E_g) \quad (5.1)$$

with the Planck constant h , photon frequency ν and a constant \mathcal{B} . The factor f depends on the nature of the electron bands and possible electronic transitions. In case of a direct transition, i.e. a direct semiconductor, f equals 0.5, an indirect transition has a factor of 2.^[95] CuInS_2 is a direct semiconductor^[72] with a calculated bulk band gap energy of 1.45 eV^[22] and experimental findings in literature of ~ 1.5 eV.^[38,96,97] The linear region in the Tauc plot in Figure 5.5 was fitted and extrapolated to determine the x -axis intercept, denoting the band gap energy. This yielded a value of 1.45 eV, consistent with literature values.

Further evidence of fully exchanged NRs can be seen in the absorbance characteristics and the diffraction patterns. The evolution of the UV-Vis-NIR spectra at a reaction temperature of 150 °C is shown in Figure 5.6a. The starting Cu_{2-x}S NRs featured a strong absorbance in the near-infrared (NIR) region. Djurleite is a Cu-deficient phase, which leads to an excess in free carriers in the valence band. The carriers can be excited by the electromagnetic field to oscillate collectively. This localized surface plasmon resonance (LSPR) is mostly controlled *via* the free hole density.^[98] With ongoing CE and increasing In incorporation into the lattice, the LSPR band (observable at wavelengths above 1000 nm) reduced in intensity and was almost completely suppressed after 30 min, with an In incorporation of 24.6 %, and vanished after 60 min of reaction time and an In incorporation of 25.2 %, i.e. complete exchange. While the LSPR band disappeared with ongoing CE, a band edge feature appeared, with the emergence after 7.5 min of reaction time at a wavelength of 755 nm, and continually increased in intensity with time. This band edge feature is consistent with observations in literature of CuInS_2 .^[99–102] By integrating the areas under the individual

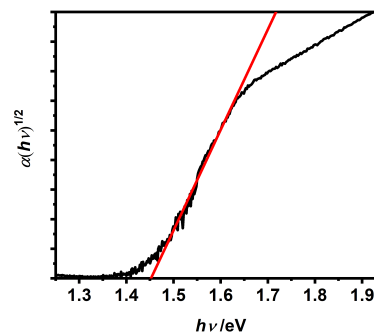


FIGURE 5.5: Tauc plot, calculated from the absorbance spectrum of the 60 min sample, depicted in Figure 5.6.

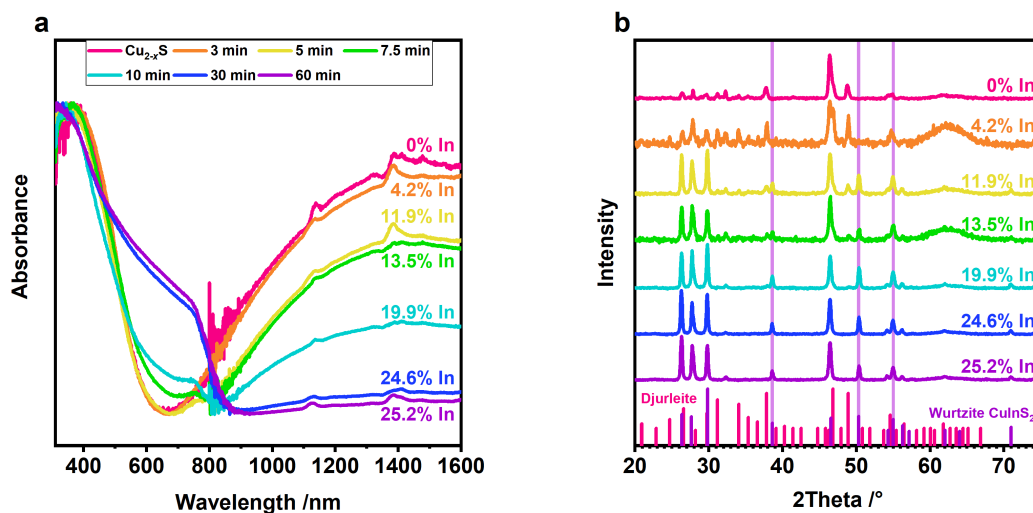


FIGURE 5.6: (a) Absorbance spectra of a CE reaction at 150 °C with reaction times from 3 min to 60 min, with the starting sample in magenta and (b) powder diffractograms of the same samples, with the reference patterns of djurleite PDF no. 00-023-0959 in magenta and of wurtzite CuInS₂ (calculated with Diamond 4.5 with lattice parameters from Pan *et al.*^[94], see Table A.1 in Appendix A.2) in purple, with extended lines highlighting three distinct reflections at 38.6°, 50.3° and 55.0° with Miller indices of (0 1 2), (0 1 3) and (1 2 2).

curves between 650 nm and 1600 nm, a linear trend could be observed in the area decrease in the first 10 min of the reaction, while the fully exchanged samples after 30 min and 60 min do not follow this trend, as depicted in the appendix in Figure A.4.

The crystallographic progress of the CE reaction at 150 °C is presented in Figure 5.6b with the diffraction pattern evolution. Corresponding in color to Figure 5.6a, the starting sample in magenta matched the reference pattern of djurleite Cu_{1.94}S (PDF no. 00-041-0959), while the diffractogram with 25.2% In, after a reaction time of 60 min, in purple, matched the calculated reference pattern of wurtzite CuInS₂ (calculated with Diamond 4.5 with lattice parameters from Pan *et al.*^[94]), indicating a full exchange based on the incorporated atomic amount of In, the quenched LSPR, as well as the diffraction pattern matching wurtzite CuInS₂. The transition to CuInS₂ was further considered a complete exchange, as no reflections that could have been attributed to djurleite Cu_{1.94}S remained after 60 min of reaction time. A further transformation of the crystal phase, in which all Cu ions would have been exchanged with In ions, resulting in an In₂S₃ phase, was not observed and was also not expected. Since djurleite and wurtzite CuInS₂ share a hcp S²⁻ anionic sublattice,^[103] but all three temperature-dependent phases of β-, α- and γ-In₂S₃ have a ccp anionic sublattice,^[104,105] the transition from djurleite Cu_{1.94}S to wurtzite CuInS₂ is strongly favored over the transition to In₂S₃. In case of the transition from low chalcocite Cu₂S to the low-temperature β-In₂S₃ phase, which is stable until 717 K,^[105] the anionic sublattice would have to switch from hcp to ccp, resulting in the shift of every four out of six S²⁻ layers of 58% of a S-S distance.^[106] The transition from djurleite to

wurtzite CuInS_2 was evident early in the reaction, after 3 min and 4.2 % In incorporation, with the appearance of the characteristic $(\bar{1}22)$ reflection at 55° , originating from wurtzite CuInS_2 . Further reflections emerged after 5 min of reaction time with 11.9 % In incorporated into the lattice, with the (012) and (013) reflections at 38.6° and 50.3° , respectively, highlighted in purple in Figure 5.6b. All characteristic reflections from djurleite, as well as from wurtzite CuInS_2 , de- and increased in intensity, but did not shift in position. If the underlying reaction mechanism was an alloying process, In^{3+} ions would diffuse through the entire NR and gradually change the lattice parameters, until the fully exchanged CuInS_2 phase was reached. The constantly changing lattice parameters would result in a continual shift of reflection positions, which was not observable here. Rather, a core/shell or a Janus-type reaction mechanism seems likelier. In both instances, the crystal phases of the starting material and of the exchanged phase would not mix, except at interface layers. Both crystal phases would contribute to the measured diffractogram signal, but since the CE reaction would not be accompanied by a gradual change in lattice parameters, but instead of the presence of both phases in the NRs at the same time, the diffraction pattern contribution of each phase would only change in reflection intensity, not in reflection position. The intensity contribution of an individual phase is then proportional to the amount of that phase in the individual NR, or in case of an ensemble measurement, as it is presented here, in all NRs of the sample. The likely presence of both crystal phases is indicated in the double peak in the 3 min sample (orange diffractogram in Figure 5.6b), with the contribution of djurleite's (080) reflection at 46.3° and the $(\bar{1}20)$ reflection of wurtzite CuInS_2 at 46.6° .

Further differences in intermediate samples with reaction conditions below and above T_{pt} were investigated *via* EDX elemental mapping and are shown in Figure 5.7. Maps of a partially exchanged sample after two weeks of reaction time at 40°C revealed that the 2.6 % In in the sample in Figure 5.7b (In is represented in green) was only present on the edges of the NRs, suggesting In could not diffuse into the volume of the NRs and that only surface layers were transformed to CuInS_2 , as illustrated in the sketch of Figure 5.7a. Figures 5.7d–f show elemental maps of intermediate samples at a reaction temperature of 120°C after 3 min (4.1 % In) and 5 min (8.6 % In). In contrast to the sample under T_{pt} , samples over T_{pt} featured bands of In along the short side of the NRs, suggesting that In ions were able to diffuse deeper than a few surface layers into the volume of the rods. Both djurleite and wurtzite CuInS_2 exhibit alternating Cu and S layers along the long axis of the NRs (a -axis of djurleite and c -axis of wurtzite CuInS_2 , respectively). Considering the unusually high diffusion constant of Cu in high chalcocite,^[87] diffusion through the Cu layers along the a - b -plane seems favored compared to the diffusion through the S layers along the c -axis. This behavior has been observed in similar experiments in the literature before.^[107,108] The bands seem to increase in width with ongoing reaction time and higher atomic amounts of In in the samples (compare Figures 5.7c–e), until In was distributed homogeneously over the entire NRs in the fully exchanged sample with

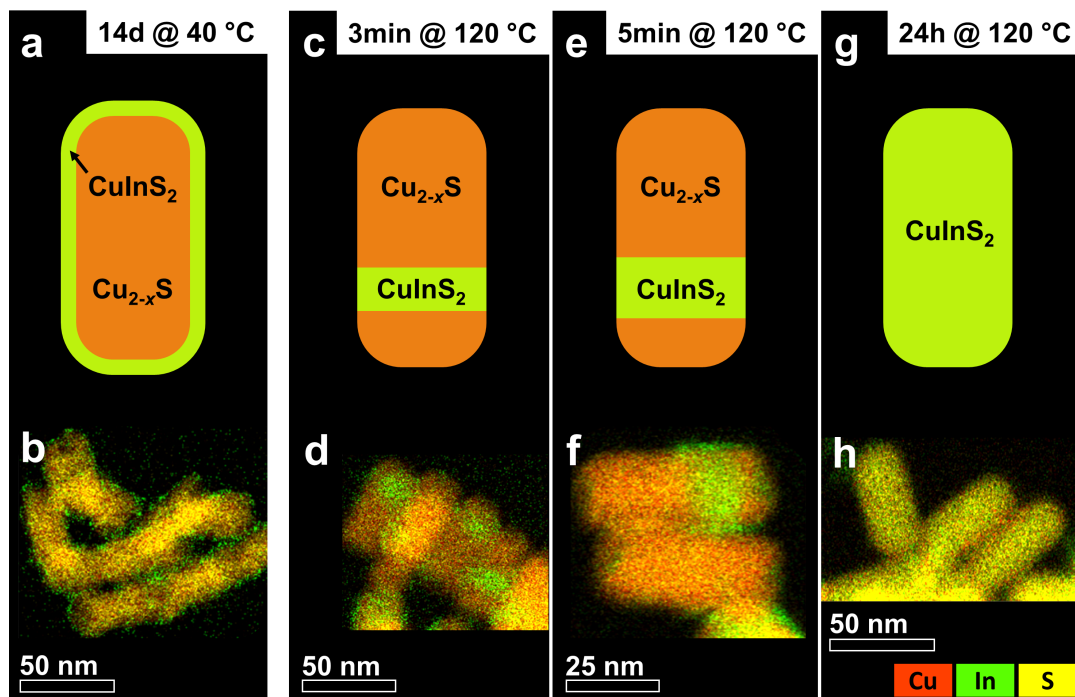


FIGURE 5.7: Schematic representation (top row) and the underlying EDX elemental mapping images from high-resolution transmission electron microscopy (HRTEM) (bottom row) of the differences in In incorporation into NRs (a–b) under T_{pt} at 40 °C after 14 d with 2.6 % In incorporated and over T_{pt} at 120 °C after (c–d) 3 min (4.1 % In), (e–f) 5 min (8.6 % In) and (g–h) 24 h (28.1 % In), with schematic representations of the exchange (a) at the surface and (c, e, g) in the volume of the NRs.

28.5%, suggesting the successful and complete transformation to CuInS₂ under size and shape retention of the original djurleite starting sample.

In order to confirm, that the In bands in Figures 5.7d–e were actually caused by the CE and the transformation of the crystal lattice, and are not only due to surface deposition of In, a HRTEM micrograph of the sample shown in Figure 5.7f was analyzed *via* FFT to determine the crystal phases. In order to differentiate between the djurleite and wurtzite phase, the FFT of the micrograph shown in Figure 5.8a was compared to the FFT of the circled area in that figure. By determining the differences between the two FFTs (*via* the free and open-source graphics editor GIMP 2.10.12, for details of the process see Appendix A.2.4), Figure 5.8b was obtained. Thus, reflections originating from djurleite could be excluded. The remaining reflections could be matched to the wurtzite CuInS₂ phase, with reflections matching Miller indices of (002) and (020). Thus, the existence of a distinct wurtzite phase inside the djurleite NR could be established.

In summary, the observation of the CE from djurleite to wurtzite CuInS₂ revealed the phase transition temperature (T_{pt}) to be of crucial significance to reach full exchange of the NRs. Above T_{pt} , NRs featured a mixture of djurleite and high chalcocite, a phase characterized by an unusually high Cu diffusivity.^[87] Below T_{pt} , no complete exchange could be observed and In was only detectable on the surface of the NRs, with increasing surface roughness, likely caused by In depositions on the

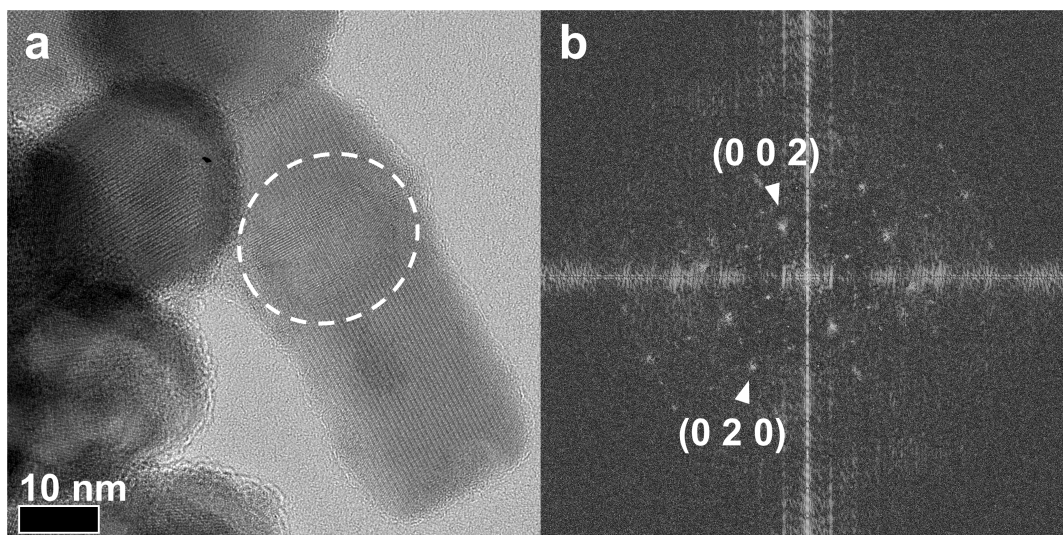


FIGURE 5.8: (a) TEM micrograph of the sample shown in Figure 5.7f, stemming from a CE reaction with the starting sample 270921-A at 120 °C after 5 min of reaction time, with 8.6 % In incorporated and (b) the FFT of the left image, representing the differences between the entire image and the circled area in a, with arrows pointing towards the (002) reflections with a d -spacing of 3.22 Å and the (020) reflections with a d -spacing of 1.69 Å.

surface as well as surface etching *via* the Cu-extracting agent TOP. Yet, the successful CE to wurtzite CuInS₂ could be demonstrated above T_{pt} under size and shape retention, with compositions determined *via* EDX measurements of stoichiometric ratios, or slightly In-rich compositions. The full exchange was further validated by means of powder diffraction, showing only reflections corresponding to the wurtzite phase, a quenched LSPR, typical for CuInS₂, and the calculation of the band gap energy, matching reports from literature of calculated and measured values. Fully exchanged CuInS₂ NRs were very stable in the reaction solution, even with long exposure, and seemed only to decrease slightly in size, mainly due to the lattice compression as a result of the transformation to the wurtzite lattice, featuring shorter S layer distances along wurtzite's c -axis. The transformation was characterized by the formation of In bands along the short axes of the NRs and was likely due to the increased Cu diffusion rate in the Cu layers, coinciding with the a - b -plane of the NRs, and proceeding comparably slow along the c -axis.

In the following section, the CE reactions are presented in a broad temperature region, in order to elucidate the significance of the phase transition from djurleite to a mixture of djurleite and high chalcocite, and the impact on the kinetics of such a reaction. From this, a CE mechanism shall be proposed.

5.2 Kinetics and Diffusion Mechanism

In order to analyze the CE reaction progress from djurleite to wurtzite CuInS₂ in greater detail, the shift in atomic percentages of Cu, S and In during the CE reactions

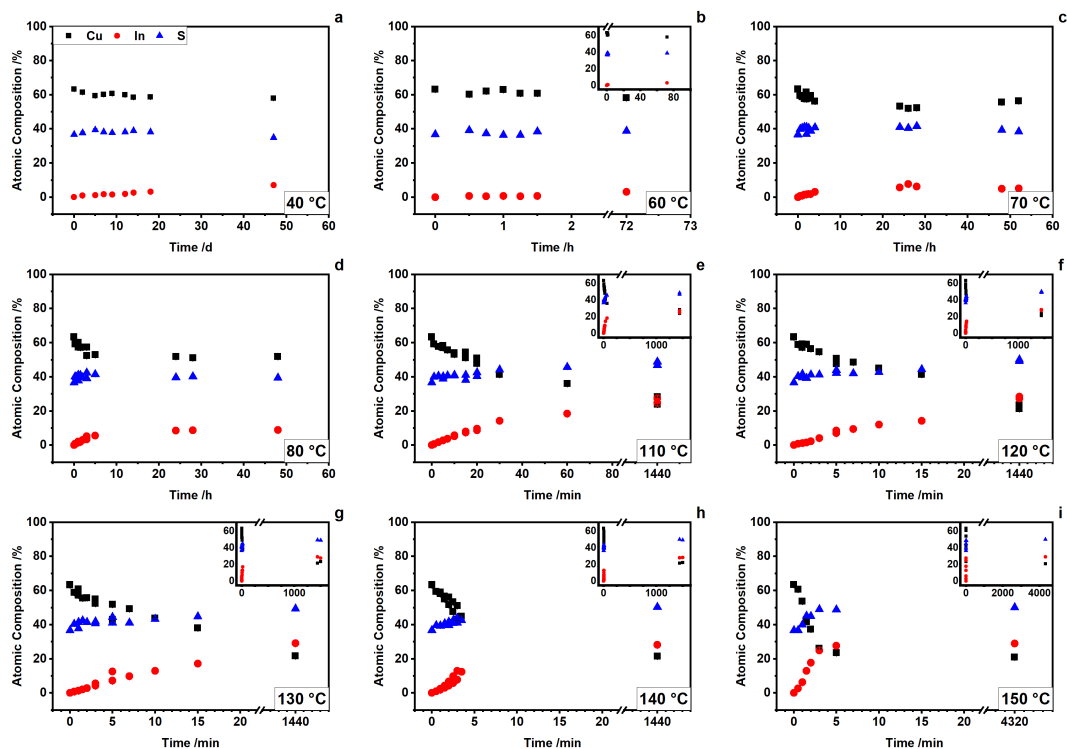


FIGURE 5.9: Progress of In incorporation into NRs during CE reactions, represented by the varying atomic percentages of Cu (black squares), S (blue triangles) and In (red circles), collected in a SEM *via* EDX measurements of ensemble samples from CE reactions below T_{pt} at (a) 40 °C, (b) 60 °C, (c) 70 °C and (d) 80 °C, and above T_{pt} at (e) 110 °C, (f) 120 °C, (g) 130 °C, (h) 140 °C and (i) 150 °C; with interrupted abscissas in b and e–i and insets in those plots to show the reaction progress to scale. The presented data originates from experiments carried out with the two starting samples 270921-A and -B. Some reaction conditions have been duplicated in order to establish the reproducibility of the experiments, hence some plots show two data points for each element at certain reaction times.

was tracked and probed *ex situ* at various temperatures below and above the phase transition temperature (T_{pt}) by collecting EDX data from ensemble samples.

Figure 5.9 shows the evolution of the atomic compositions of CE reactions between 40 °C and 150 °C. A linear rise of the In incorporation with time was observable in all samples. In samples under T_{pt} a saturation of the In incorporation manifested below the expected value of 25 % for fully exchanged and stoichiometric CuInS_2 NRs. After 47 d at 40 °C the In amount was at 7.1 %, and at 5.8 % and 8.8 % after 24 h at 70 °C and 80 °C, respectively. The CE reaction at 60 °C did not seem to be saturated at the longest observed reaction time of 72 h. In reference to the findings in Section 5.1, relating to the elemental mapping, In seemed only to be present near the surface of the NRs in the samples under T_{pt} (see Figure 5.7b). By estimating the fraction of one or more layers of surface atoms in relation to the total amount of atoms per NR, the measured atomic percentages of In led to conclusions about the diffusion depths of In^{3+} during the CE and the amount of layers that might have been exchanged in the process. An average NR of the starting sample 270921-A contained $2.1 \cdot 10^6$ atoms, with 8.2 % of atoms in the first layer, 15.9 % in the second and

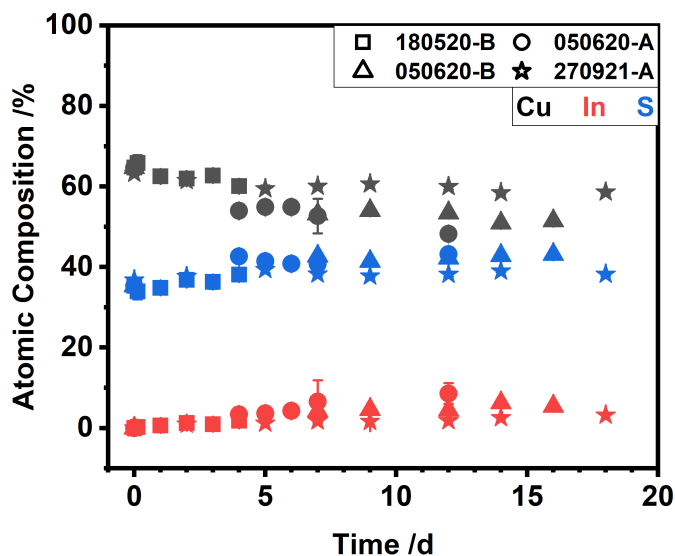


FIGURE 5.10: Progress of the Cu, In and S incorporation into NRs during CE reactions at 40 °C. Reactions have been carried out with the same parameters and four different starting samples, identified by the four data point shapes.

23.3% in the third (see calculations in Appendix A.2.3). In a perfectly exchanged and stoichiometric surface layer of CuInS_2 , one of every four atoms would be In, which would contribute to the EDX signal. So if, for example, a given sample was made up of 5.8% In, and it was assumed that the detected In signal originated only from surface layers composed of stoichiometric CuInS_2 , the proportion of atoms in that surface phase must be four times the atomic amount of In. A CuInS_2 shell containing $4 \times 5.8\% = 23.2\%$ of the total amount of atoms in a NR is approximately equivalent to a CuInS_2 phase with a depth of three surface layers, very close to the calculated value of 23.3% for the surface fraction of three layers. An In saturation of 7.1% would equal a surface fraction of 28.4%, and matched the calculated value of 30.3%, corresponding to four exchanged surface layers. The In saturation of the CE reaction at 80 °C even suggested an extent of the exchanged surface phase of five layers. Replications of a CE reaction at 40 °C (see Figure 5.10) with the same conditions but different starting samples supported the previous observations. The In incorporation in all samples at 40 °C was consistently linear in the first seven days of the reaction, and the atomic amounts were consistent as well. Between nine and eighteen days of reaction time the conformity of the incorporated In amount for a given reaction time varied slightly more between individual starting samples, but was still in close agreement. The variation could either be a result of different diffusion depths at a given time, or due to the different sizes of the starting samples. A smaller NR will have more atoms on its surface in relation to its volume, compared to a larger NR. Thus, for the same amount of exchanged surface layers, the amount of In would be higher in a small NR, compared to a larger one. Moreover, the variation could be an indicator for the onset of the saturation regime.

In conclusion, the CE at reaction conditions below T_{pt} seemed to follow a core/shell mechanism, in which only surface layers were exchanged to CuInS_2 . The reaction seemed to self-limit before a full exchange could be reached, and a shell with a depth of only three to five layers was exchanged, before the CE converged.

In contrast, all experiments above T_{pt} resulted in fully exchanged samples with atomic amounts of In between 24.8% and 29.0%. Atomic amounts above 25% are not uncommon and it is well documented in the literature, that CuInS_2 can tolerate off-stoichiometry and In-surpluses well.^[72,109–111] Even with long exposures of the NRs to a surplus of In in the reaction solution at elevated temperatures, the composition remained stable and close to stoichiometric CuInS_2 . As predicted, the shared anionic hcp sublattice prevented a further exchange to In_2S_3 , even after three days of reaction time at 150 °C.

A consistently observable trend in all CE reactions was the linear rise in In incorporation. Reactions with rates independent of the precursor concentration, here the In concentration expressed as $[\text{In}]$, typically follow a rate law of zero order^[45]

$$-\frac{d[\text{In}]}{dt} = k \quad (5.2)$$

with the rate constant k . In order to support the hypothesis, that this CE reaction indeed follows a zero order rate law, a linear rise in In incorporation should still be observable for conditions with increased precursor concentration in the reaction solution. And indeed, Figure 5.11 demonstrates the linear behavior of the In incorporation, regardless of the In precursor concentration. Yet, the increased concentration also led

to an increased slope of the linear regression (dark red) in Figure 5.11. This concentration-dependence suggests no real zero order reaction rate. More likely, the reaction is limited by the incorporation of In into the NRs. Nevertheless, a higher In precursor concentration affected the reaction rate and accelerated the cation exchange. Since the rate of In incorporation is relatively slow, and In is present in a large excess in the reaction solution, the In concentration can be approximated as constant. Thus, the reaction should more aptly be described as pseudo-zero order by^[45]

$$-\frac{d[\text{In}]}{dt} = k' \quad (5.3)$$

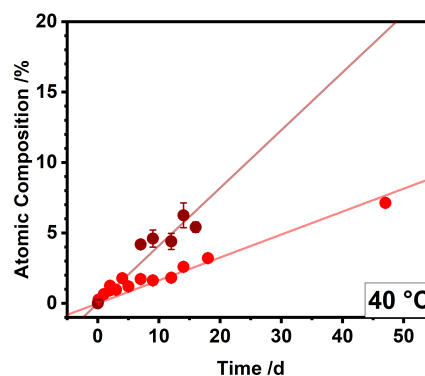


FIGURE 5.11: In incorporation of a CE reaction at 40 °C with data points originating from a reaction with the regular In precursor concentration in red, and a CE reaction with the same reaction parameters, except a threefold increase in In precursor concentration (in dark red), with linear regressions to illustrate the linear behavior, with coefficients of determination of 0.95 for the regular reaction and 0.97 for the reaction with three times the amount of In precursor.

with the new rate constant $k' = k [\text{In}]$, and with $k' \gg k$.

By fitting the linear regions of the In incorporations, presented in Figure 5.9, rate constants could be extracted from each individual reaction temperature between 40 °C and 150 °C. The temperature-dependence of the rate constants $k(T)$ can be described as^[45]

$$k(T) = Fe^{-\frac{E_a}{RT}} \quad (5.4)$$

with the reaction temperature T , a pre-exponential factor F , the activation energy of the reaction E_a and the universal gas constant R . By taking the natural logarithm, Equation 5.4 can be expressed as^[45]

$$\ln k = \frac{-E_a}{R} \left(\frac{1}{T} \right) + \ln F \quad (5.5)$$

which has the form of a typical linear equation $y = mx + b$. Thus, the slope of the natural logarithm of the rate constants plotted against the inverse reaction temperature yields the activation energy. This plot is commonly referred to as an Arrhenius plot. The Arrhenius plot obtained from the data shown in Figure 5.9 is presented in Figure 5.12. The linear regressions to determine the individual rate constants were only obtained from the linear regions of each data set. Regions of saturation were excluded from these calculations, as they would have skewed the results. As detailed previously in Section 5.1, the CE reactions were strongly influenced by the phase transition temperature (T_{pt}) and it stands to reason to fit regions below and above the phase transition temperature separately, determined by DSC measurements to an average of 87.5 ± 1.1 °C. This resulted in an activation energy for CE reactions conducted below T_{pt} of 128 ± 24 kJ mol⁻¹, while the activation energy above T_{pt} was determined to be 37 kJ mol⁻¹ lower, with 91 ± 10 kJ mol⁻¹. The hypothesis of an influence of T_{pt} was further corroborated by the point of intersection of the two linear regression curves at 0.00273 K⁻¹, which is equal to 93.2 °C and is thus in good agreement with the experimentally determined phase transition temperature.

Kawai and Okamoto calculated the activation energy for the motion of Cu vacancies as 0.24 eV^[86] (23.2 kJ mol⁻¹). Since the activation energy in the present work was calculated based on the diffusion of In³⁺ ions with an ionic radius of 62 pm,^[112] compared to the slightly smaller radius of Cu⁺ with 60 pm,^[112] it stands to reason that a larger ionic radius would inhibit the diffusion *via* interstitials or vacancies more than a smaller ionic radius would, resulting in a higher activation energy. But more importantly, the difference between the calculated activation energy and the energy calculated for the motion of Cu vacancies could indicate that the diffusion itself may not actually constitute the rate-limiting step of the CE reaction (further discussion on the rate-limiting step follows below). Differences in the activation energies suggest that the phase transition from djurleite to a mixture of djurleite and high chalcocite above T_{pt} indeed led to higher Cu⁺ ion mobilities, and thus likely higher In³⁺ mobilities as well. And even though djurleite is already a Cu-deficient copper sulfide

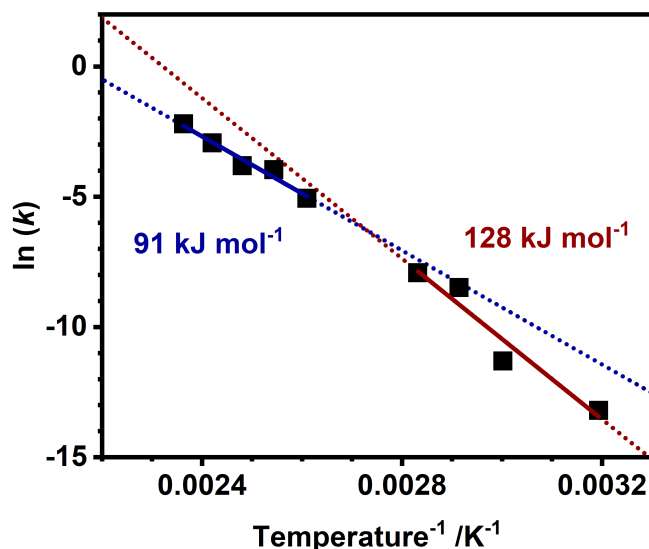


FIGURE 5.12: Arrhenius plot to determine the activation energies of the CE below and above T_{pt} . Rate constants were obtained from linear regressions of the EDX data presented in figure 5.9. The rate constants were plotted and the slopes of the individual linear regressions were proportional to the activation energies. The activation energy below T_{pt} was $128 \pm 24 \text{ kJ mol}^{-1}$ (linear regression line in red, extended with dots to visualize the intersection), the activation energy above T_{pt} was $91 \pm 10 \text{ kJ mol}^{-1}$ (linear regression line in blue). The point of intersection was at 0.00273 K^{-1} , which equals $93.2 \text{ }^\circ\text{C}$.

phase with eight vacancies per unit cell^[74,113] at conditions below T_{pt} , the phase transition to high chalcocite accompanied by high Cu diffusivities^[82,114] still resulted in a distinctly different reaction outcome. Therefore, the differences can not only be explained by varying amounts of vacancies below and above T_{pt} .

Figure 5.13a illustrates the observed behavior during CE reactions schematically. Below T_{pt} , only surface layers are exchanged to CuInS_2 , while at reaction temperatures above T_{pt} , bands of CuInS_2 emerged along the short axis of the NRs, which grew in size along the long axis of the NRs until the CE was completed. This evolution during the CE can be explained with the crystal structures of the involved species. All phases share a similar anionic sublattice: Djurleite has a distorted hexagonally close-packed (hcp) sublattice,^[82] while high chalcocite and wurtzite CuInS_2 both have a hcp S^{2-} sublattice.^[115,116] The exchange *via* a shell formation is possible, as well as favored, from the side of the NRs at conditions below T_{pt} , because djurleite and wurtzite only have a small mismatch of the ABAB stack of S layers along djurleite's a -axis of 1.0%, while the mismatch between high chalcocite and wurtzite is slightly larger with 4.6% along the b -axis (illustrated by the red lines in Figure 5.13). The lattice mismatch does not intrinsically inhibit the formation of a CuInS_2 shell for temperatures above T_{pt} , but as will be shown in the following, other factors promote the CE inside the NRs more. The diffusion of In^{3+} ions from the side of the NRs is further favored, compared to the tips, as large ligands with steric hindrances employed in the reaction, i.e. TOP, TOPO and *tert*-dodecanethiol,

can pack denser on curved surfaces, like the NR tips, compared to the less densely packed sides, which are then more accessible for the In-precursors to adsorb on the surface.^[108] For temperatures above T_{pt} , the observed formation of wurtzite bands along the short side of the NRs coincides with the b - c -plane of high chalcocite, which features partially occupied Cu lattice sites, denoted by partially filled spheres in Figure 5.13b. The diffusivity along this plane has been described in literature as liquid-like^[87] and thus strongly promotes the diffusion of In^{3+} ions inside the Cu plane (b - c -plane), compared to the diffusion through the S planes, along the c -axis. This in-plane diffusion has also already been reported in literature.^[108,117-121] Additionally, after the diffusion of the first In^{3+} ion into a djurleite NR to an energetically favorable lattice site for the initial exchange, the formation of one reaction front in the NR minimizes the interfacial area with the non-exchanged phase of the NR.^[118] This is further justified by the higher self-diffusivity of In^{3+} ions inside the wurtzite phase due to the ion's lower coordination, compared to it in the djurleite or high chalcocite phase, promoting the formation of one band of CuInS_2 per NR.

In order to determine the rate-limiting step of the CE reaction, the activation energy, i.e. the sum of the formation energy of the species diffusing into the NR and the energy barrier of its migration, must be evaluated. While CE reactions with a diffusion mechanism based on interstitial sites feature activation energies typically in the range of 30 kJ mol^{-1} to 40 kJ mol^{-1} ,^[123] a vacancy-mediated diffusion mechanism is usually in the order of 100 kJ mol^{-1} .^[23] With the determined activation energies of $128 \pm 24 \text{ kJ mol}^{-1}$ and $91 \pm 10 \text{ kJ mol}^{-1}$ below and above T_{pt} , respectively, a vacancy-mediated diffusion mechanism seems likely. The rate-limiting step is then either the creation of more vacancies, because the initial amount was too low in the NRs to drive the CE, or the energy barrier of diffusion *via* vacancies itself. As only surface layers were exchanged below T_{pt} , the diffusion of In^{3+} ions must be limited. Above T_{pt} , and with the emergence of high chalcocite, the diffusivity through the Cu layers increased, while the diffusion through the S layers was slow in comparison. Since djurleite was still present in the NRs above T_{pt} , an activation energy reduction of 37 kJ mol^{-1} seems reasonable. But with only eight Cu vacancies per 376 atoms in the djurleite unit cell^[103] and no vacancies in the high chalcocite Cu_2S unit cell, the creation of additional vacancies must be the rate-limiting step.

5.3 Special Conditions for Cation Exchange Reactions

The following section aims to examine special conditions for the CE reaction from Cu_{2-x}S to CuInS_2 . The kinetics have been discussed above, postulating the phase transition temperature (T_{pt}) as a key factor in guiding the exchange of either surface layers, or the entire volume of NRs during the exchange. In Section 5.3.1 special attention is paid to the threshold temperature right at T_{pt} , at which the djurleite phase transforms to a mixture of djurleite and high chalcocite. Section 5.3.2 then

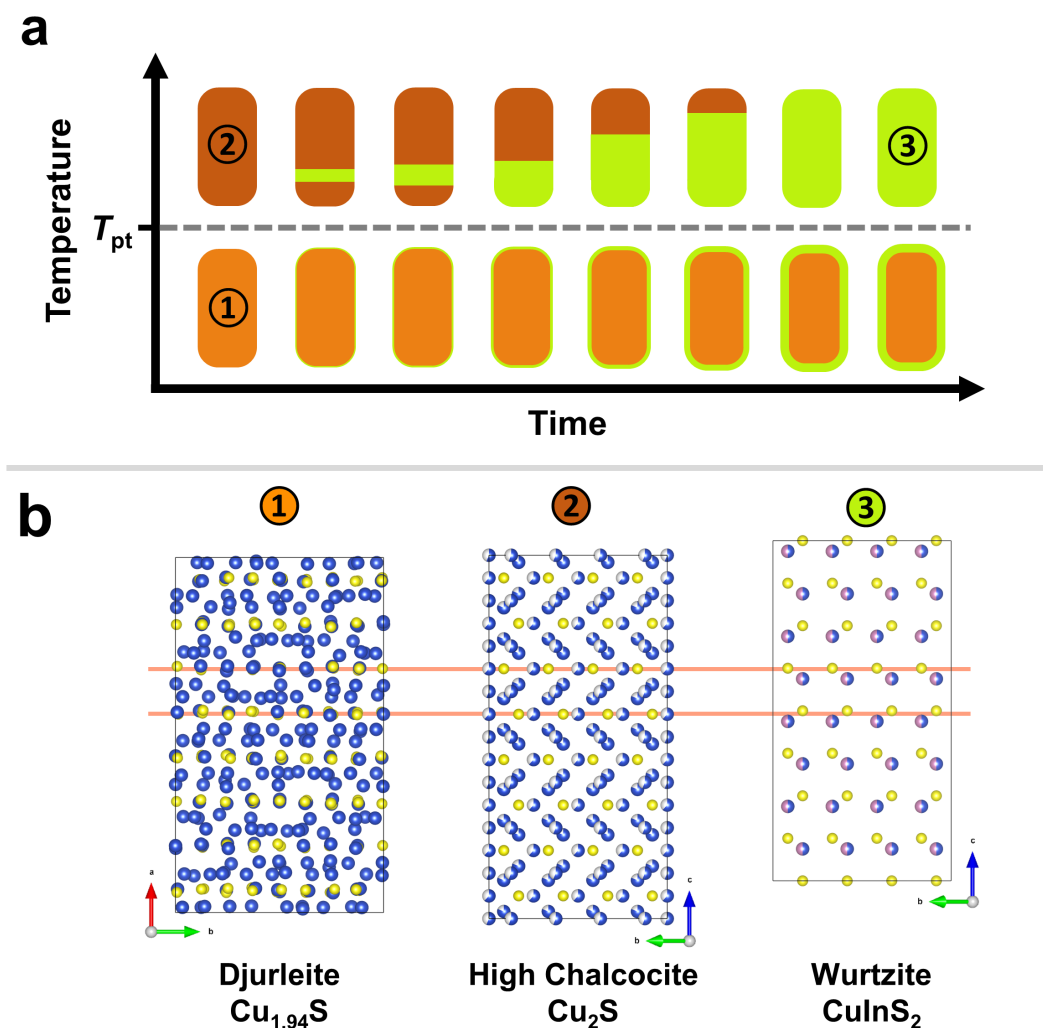


FIGURE 5.13: (a) Schematic of the NR evolution during CE reactions below and above T_{pt} . Only some surface layers of the djurleite crystal phase (①) were transformed to the wurtzite $CuInS_2$ phase (③) below T_{pt} , while the CE above T_{pt} resulted in the crystal phase transformation into a mixture of djurleite and high chalcocite (②) and proceeded *via* the formation of wurtzite $CuInS_2$ bands. (b) Comparison of the three above mentioned crystal structures (blue spheres represent Cu, yellow represents S and purple In) with ① one unit cell of djurleite, and 4×4 unit cells of ② high chalcocite (with partially filled blue spheres, representing the partial occupations of the respective lattice site) and ③ wurtzite $CuInS_2$ (with two-colored spheres representing the statistical occupation of all lattice sites with either Cu or In with a probability of 50%^[122]). The correlation of the anionic S sublattice is illustrated by the two red horizontal lines.

introduces an entirely new parameter, in addition to time and temperature, to influence the reaction outcome, by studying the CE under exposure to ultraviolet (UV) light.

5.3.1 Cation Exchange Near the Phase Transition Temperature

The study of the CE from $Cu_{2-x}S$ to $CuInS_2$ revealed the crucial role of the phase transition temperature on the phase transition and the associated difference in the diffusion of In^{3+} ions inside the NRs. DSC measurements determined the average

phase transition temperature to $87.5 \pm 1.1^\circ\text{C}$, while the Arrhenius plot suggested a phase transition temperature of 93.2°C . In order to study the CE at the threshold of the phase transition, a CE temperature of 90°C was chosen.

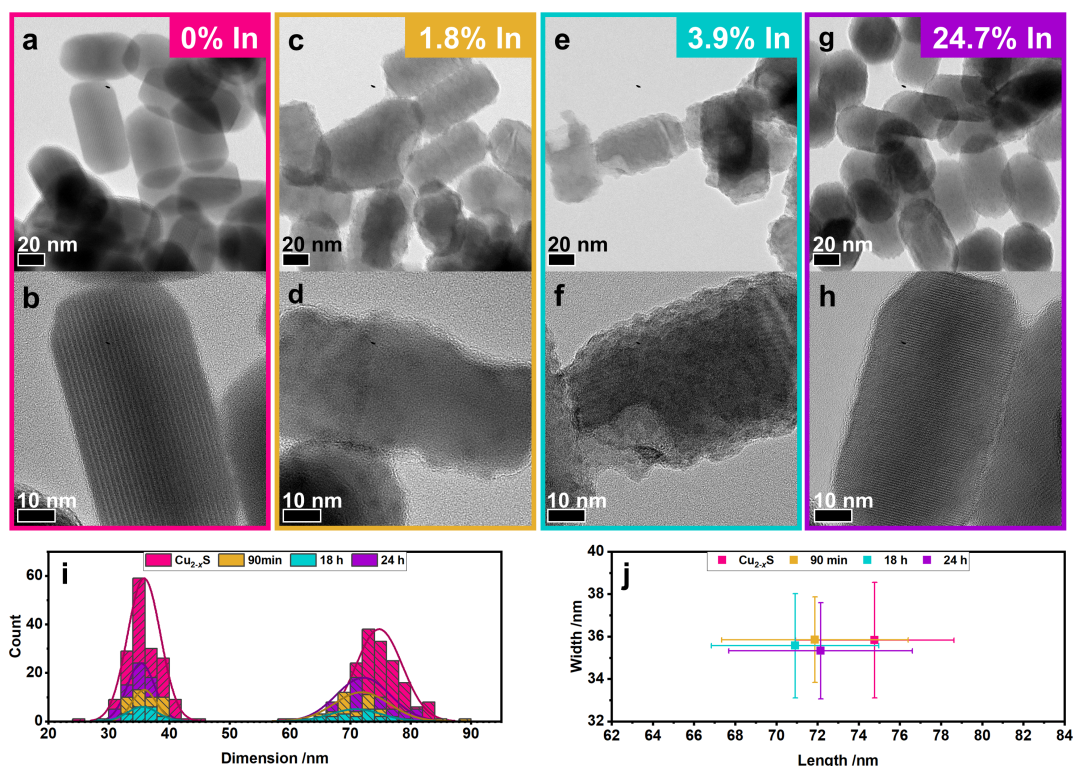


FIGURE 5.14: TEM micrographs of (a–b) the starting sample 160419-A, and of samples after a CE reaction at 90°C after (c–d) 90 min with 1.8% In, (e–f) after 18 h with 3.9% In and after 24 h with 24.7% In, (i) with the size distribution histograms of the four samples and (j) the mean sizes in corresponding colors.

TEM micrographs in Figure 5.14 revealed a morphology evolution similar to that observed for samples above T_{pt} , as shown in Figure 5.3. As observed before (see Figure 5.3), the surface roughness of the NRs increased with ongoing reaction time, but regained smooth and faceted surfaces after 24 h of reaction time with 24.7% In, indicating a full and successful exchange to CuInS_2 . Similarly, the average NR length decreased from 74.8 ± 3.8 nm before the reaction to 72.1 ± 4.5 nm after 24 h. The width decreased marginally from 35.8 ± 2.7 nm to 35.3 ± 2.7 nm, within the margins of error. The decrease in length was in line with the expected anionic lattice compression of 4.2% along the a -axis of djurleite. The S layers along djurleite's b -axis had to compress 1.0%, matching the observed width decrease of 1.4%. In contrast to reactions above T_{pt} at 120°C (see Figure 5.4), which yielded fully exchanged NRs, the width did not decrease beyond the expected value of the lattice compression for the reaction at 90°C . One reason could be milder reaction conditions, impeding the extraction of Cu^+ ions by TOP and TOPO.

During reaction times up to 6 h, the In incorporation into the NRs (see Figure 5.15a) proceeded linearly, as with all other observed experiments. Between 18 h and

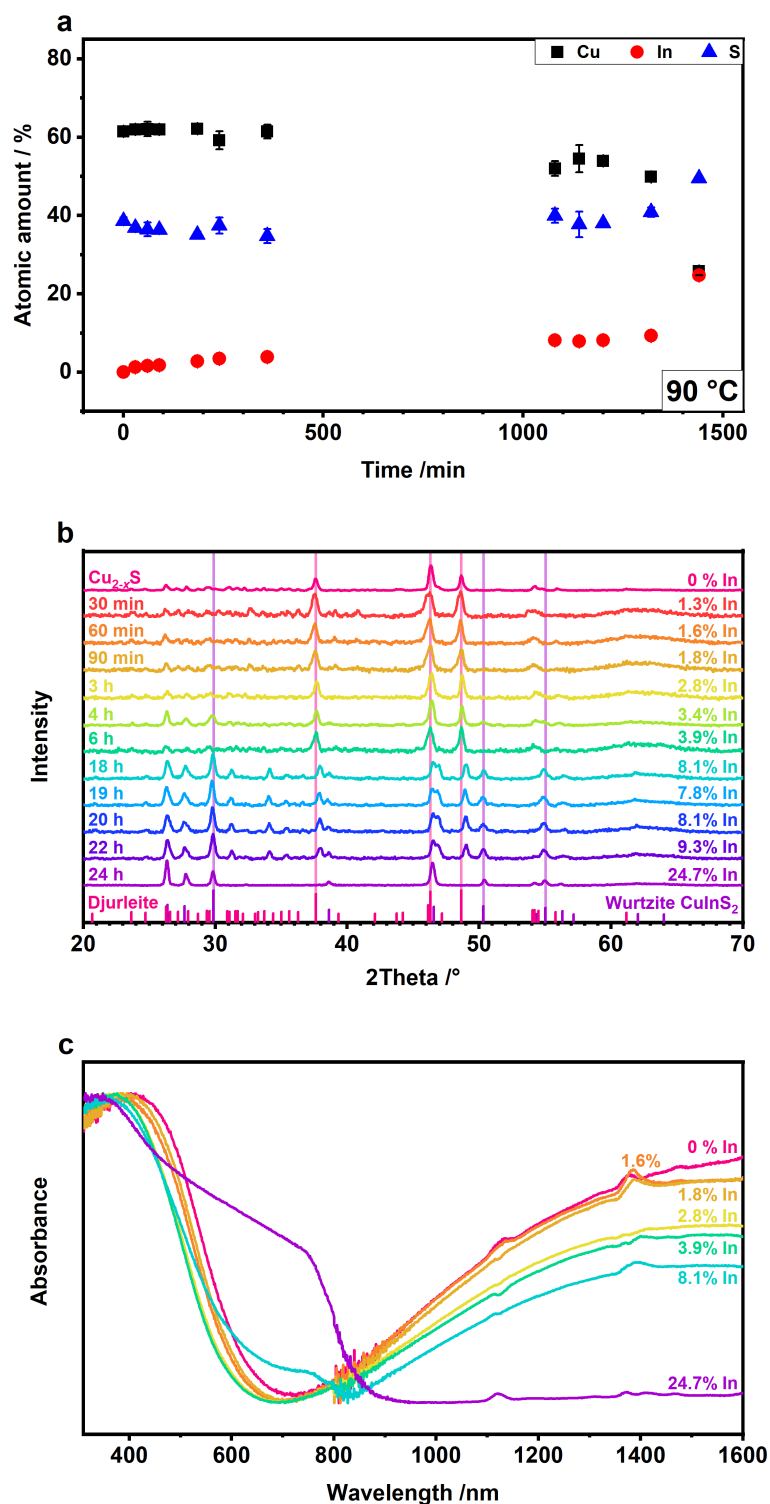


FIGURE 5.15: Evolution of (a) the atomic composition of Cu (black cubes), In (red circles) and S (blue triangles), (b) the powder diffraction patterns with reference patterns of djurleite (PDF no. 00-023-0959) in magenta, with lines extending characteristic reflections at 37.6° , 46.3° and 48.7° with Miller indices of (804), (080) and (1204), respectively, and of wurtzite CuInS_2 (calculated with Diamond 4.5 with lattice parameters from Pan *et al.*^[94], see Table A.1 in Appendix A.2) in purple, with extended lines highlighting three distinct reflections at 29.9° , 50.3° and 55.0° with Miller indices of (011), (013) and (122), respectively, and (c) the absorption spectra of the djurleite NR starting sample 160419-A and from samples of the CE reaction at 90°C between 30 min and 24 h.

22 h the linear increase of the In atomic amount stagnated and a saturation of approximately 8% In incorporation set in. However, between 22 h and 24 h the In incorporation jumped from 9.3% to 24.7%, indicating a full exchange to CuInS_2 . In fact, the composition after 24 h is almost perfectly stoichiometric with $\text{Cu}_{1.04}\text{In}_{1.00}\text{S}_2$. Such a rapid increase of In, deviating from the typical linear increase of In incorporation, has not been observed under any other reaction conditions. This feature seems unique to the volatile conditions at the phase transition temperature (T_{pt}).

The evolution of the powder diffraction pattern, shown in Figure 5.15b, featured only reflections associated to the starting phase of djurleite until a reaction time of 6 h with In amounts of 3.9%. No reflection shifting could be observed, clearly visible at the marked reflection positions of 37.6° , 46.3° and 48.7° . Unchanging reflection positions reinforces the assumption, that In^{3+} ions did not diffuse into the volume of the NRs under T_{pt} , but rather exchanged only a few surface layers. As explained before, two distinct crystal phases of djurleite and wurtzite in individual NRs result in a superposition of two sets of reflections, relating to the two phases, while an alloying process would result in a constant shifting of reflection positions, due to a constant shift in lattice parameters. After 18 h of reaction time, reflections matching to wurtzite CuInS_2 emerged and characteristic wurtzite reflections emerged, e.g. at 26.4° , 27.7° , 29.9° and 50.3° . In addition, double peaks formed, relating to djurleite and wurtzite, for example between 46° and 47° . The emergence of wurtzite reflections coincides with the onset of the In incorporation and hence the saturation thereof. The saturation could indicate, that the highest possible amount of surface layers had been exchanged, constituting a sufficient layer thickness of the wurtzite phase, to contribute to the diffraction signal.

The absorbance spectra in Figure 5.15c somewhat support this reasoning. The steady incorporation of In into the surface layers of the NRs increasingly suppressed the LSPR, until it fully disappeared after 24 h of reaction time. In addition, the vanishing of all djurleite reflections from the diffractogram of the 24 h suggest a full exchange to wurtzite CuInS_2 . In accordance to the emergence of wurtzite reflections in the diffractograms, an absorption shoulder at 750 nm appeared (close to the shoulder observed in Figure 5.6 at 755 nm), suggesting a substantial amount of CuInS_2 in the partially exchanged NRs.

The amount of In was related to its occurrence in the NRs *via* elemental mapping. Figure 5.16a reveals, that after 90 min reaction time, in the regime of linear increase of the atomic In amount in the particles, In was only present on the surface of the NRs. Surprisingly, in the regime of In saturation, after 18 h of reaction time with 8.1% In, some NRs featured surface depositions of In (Figure 5.16b), while others exhibited Janus-like distribution of In, forming bands likely comprised of wurtzite CuInS_2 , so far only observed with reaction temperatures above T_{pt} .

This concurrent occurrence of the two earlier proposed reaction mechanisms for below and above T_{pt} , self-limited CE of several NR surface layers and diffusion into the NR volume with the formation of wurtzite bands along the short particle axes

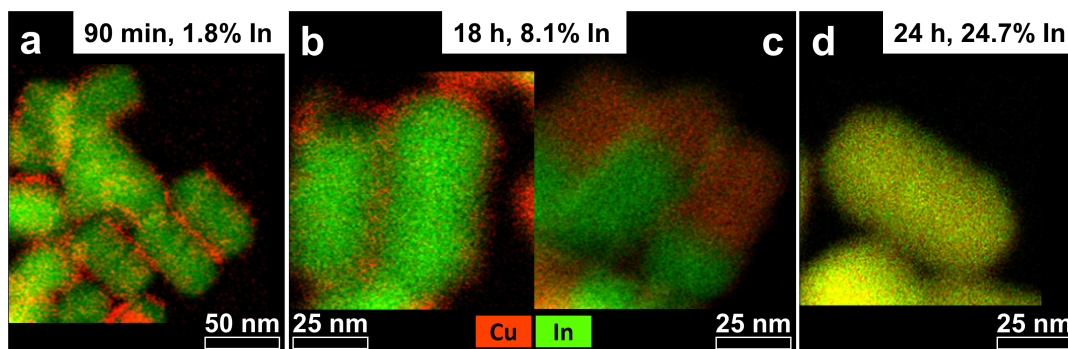


FIGURE 5.16: EDX maps visualizing the progress of In incorporation into djurleite NRs during a CE at 90 °C. Intermediate samples after (a) 90 min and (b) 18 h of reaction time, and (c) a fully exchanged sample after 24 h, with Cu represented in red and In in green.

resulting in fully exchanged NRs, respectively, seems to be unique to the very small temperature region below and at T_{pt} . It seems likely that NRs were in the djurleite phase, as the CE reaction proceeded in the typical linear fashion of In incorporation and reached the saturation regime, characteristic of the self-limiting exchange of surface layers to the wurtzite phase. But as the final product of the reaction after 24 h was made up of only fully exchanged NRs, confirmed by the stoichiometric composition *via* EDX, the diffraction pattern with reflections relating only to the wurtzite phase, and the complete suppression of the LSPR in the absorbance spectrum, it seems plausible that the NRs could have transitioned spontaneously to a mixture of djurleite and high chalcocite towards the end of the saturation regime, in order to reach full CE.

5.3.2 UV Light Influence

It was shown that the phase transformation of djurleite had a key role in the CE mechanism. Tao *et al.* could show that a phase transformation could also be induced by tuning the carrier concentration from low chalcocite to high chalcocite.^[124] This phenomenon could also be observed in the case of djurleite NRs. Figure 5.17 demonstrates that the FFTs on the right of the real space images on the left change with increasing electron beam dose. This process was reversible and reproducible. In theory, electron beam illumination could lead to "ionization, heating, electrostatic charging and knock-on damage"^[124] in a crystal. But the publication could rule out ionization as the cause for the phase transformation, since they observed no differences in the fine structures of the Cu-L edges in the low and high chalcocite phases in electron-energy-loss spectra. Moreover, heating as a result of the electron beam exposure was also eliminated, due to the reversible and oscillatory nature of the transition. The knock-on damage was assumed to have, if any, only a minor effect on the phase transition. Therefore, it was concluded that the reason for the observed phase transition must be induced by electrostatic effects.^[124]

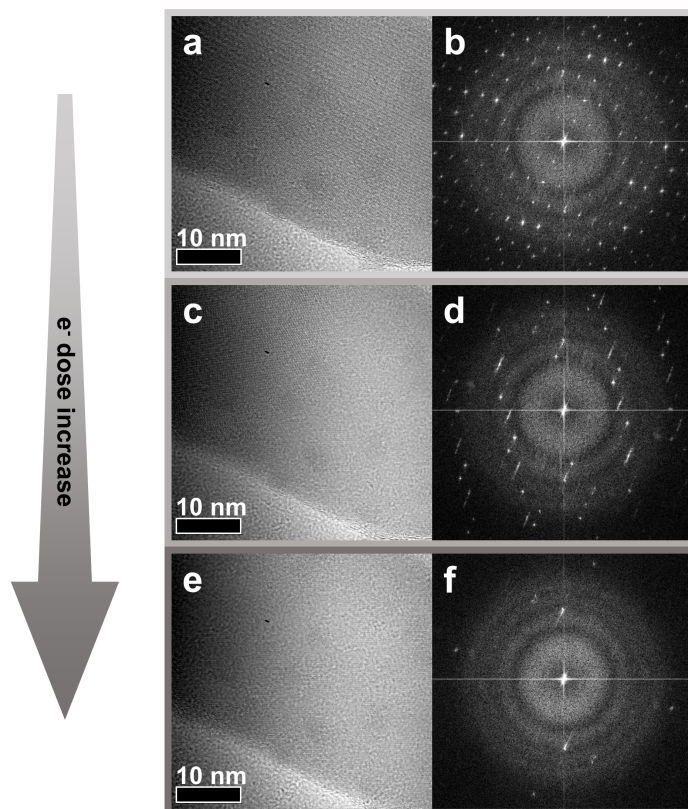


FIGURE 5.17: (a, c, e) Sample 160419-A was observed in the HRTEM under increasing electron beam doses from a to e, with (b, d, f) the corresponding FFTs to the micrographs on the left.

Electron illumination of a sample generates secondary and Auger electrons, which exhibit different escape depths, depending on the material properties. Semiconductors, e.g. low chalcocite and djurleite, have lower escape depths, compared to insulators, like high chalcocite. As a result of the escaping electrons, electron holes are left in the NCs, which would either accumulate on the surface of semiconducting NCs, or in the insulating case would be distributed in the entire volume of a NC. This renders the insulating high chalcocite phase energetically favorable in the case of high electron beam doses, and can induce a phase transition to high chalcocite below its phase transition temperature (T_{pt}).^[124]

For a more practical experimental setup, the electron beam was to be substituted with a light source. In order to still excite enough charge carriers to promote the above-mentioned phase transition, electromagnetic waves must carry energies above that of the band gap energy of a given semiconductor. If an incident electromagnetic wave is of sufficient energy, an electron can be excited from the valence into the conduction band, generating an exciton, i.e. an excited electron and a hole. Djurleite has a reported band gap between 1.2 eV to 2.2 eV.^[78,125–127] Therefore, UV light with a wavelength of 365 nm and an energy of 3.4 eV—above djurleite’s band gap energy—was chosen and a reactor holding four 9 W UV lights (see Appendix A.2.5 for details) was built.

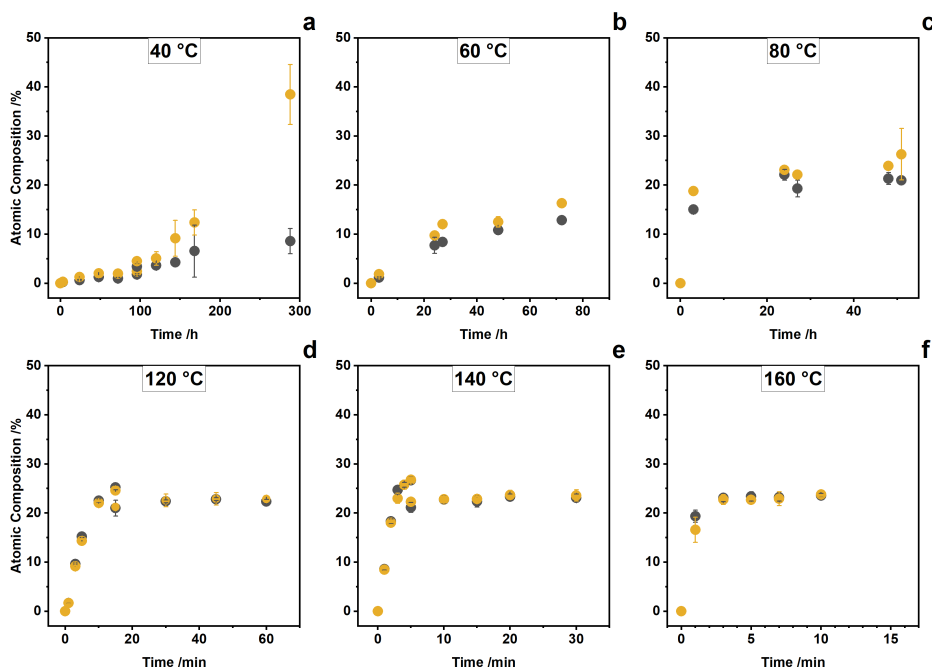


FIGURE 5.18: In incorporation into the djurleite NR starting sample 160419-A, with reaction temperatures of (a) 40 °C, (b) 60 °C, (c) 80 °C, (d) 120 °C, (e) 140 °C and (f) 160 °C. The reference experiments are plotted in dark grey and the UV illuminated experiments in yellow.

CE reactions were carried out in the same fashion as experiments described before, with the addition of UV light as a third parameter to time and temperature. In order to eliminate any other possible influences on the reaction outcome, experiments were divided into a UV illuminated and a reference group under previously used ambient light conditions. UV illuminated experiments of any time and temperature always entailed a reference experiment with the exact same djurleite NR starting sample and In precursor solution.

Figure 5.18 shows the In incorporation into djurleite NRs from 40 °C to 160 °C, i.e. three experimental conditions below and three above T_{pt} . The UV illuminated experiments exhibited differences, but also similarities to the reference experiment. Similarities could be observed, firstly, in the typical linear In incorporation at early reaction times; and secondly, in the saturation of In incorporation below 25 % below T_{pt} and close to 25 % above T_{pt} . Here, all experiments at 120 °C, 140 °C and 160 °C showed a saturation approximately between 23 % and 27 %. (Steps in the data in Figures 5.18d–e are due to data points stemming from two experiments, sometimes resulting in slightly varying atomic amounts in samples, even under the exact same conditions.) Differences between the UV illuminated and reference experiments are reflected in the In incorporation below djurleite’s phase transition temperature. It appears, as if more In was incorporated into the NRs in the UV illuminated experiments at any given time at 40 °C, 60 °C and 80 °C (Figures 5.18a–c). Since these differences were observed in all three cases and were consistent in all conducted experiments below T_{pt} , an effect of the UV light exposure on the kinetics seems plausible. No significant difference in In incorporation was discernible above T_{pt}

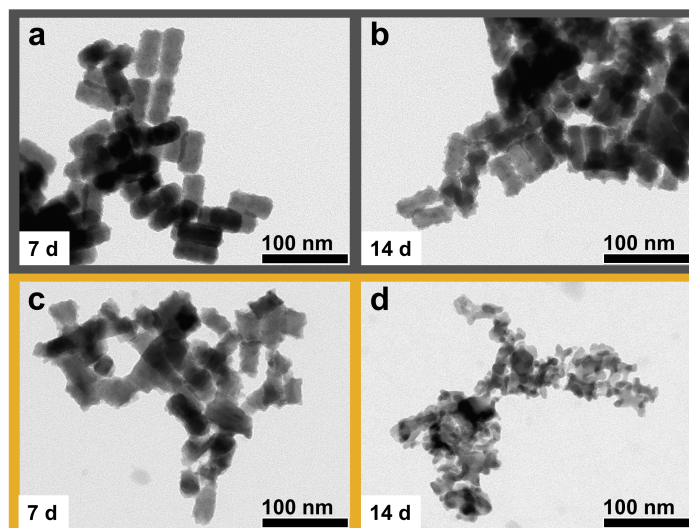


FIGURE 5.19: TEM micrographs of samples from CE reactions at 40 °C, with (a) the reference experiment after 7 d and (b) after 14 d reaction time, and (c) the UV illuminated experiments after 7 d and (d) after 14 d reaction time.

(Figures 5.18d–f). In contrast to earlier experiments, the CE at 80 °C likely resulted in fully exchanged NRs for the UV illuminated and the reference experiments alike. Even though the saturation was around 21 % in the reference experiment, the saturation remained consistent over 27 h, suggesting a slightly under-stoichiometric CuInS_2 phase as the final product. This could also indicate, that the phase transition temperature in this particular NR sample was closer to 80 °C, compared to previously studied samples. The largest difference between the UV and reference experiment was apparent at 40 °C. After 288 h (12 d) of reaction time, an In saturation likely set in with 8.6 %, while the UV illuminated reaction yielded an In incorporation of 38.5 %. This value seems high, even considering the ability of wurtzite CuInS_2 to tolerate off-stoichiometry.

TEM micrographs from samples of the experiment at 40 °C carried out with and without UV illumination provide insight into the reason for the unexpectedly high In incorporation. The morphologies of the unlit samples (Figures 5.19a–b) were typical for reaction times of these durations. The surface roughness increased with ongoing reaction time, comparable to the CE reaction also carried out at 40 °C, discussed before in reference to Figure 5.1. Even with continually increasing surface roughness over a period of two weeks, the rod-like shape was still apparent. In contrast, the NR shape was considerably corroded over time in the UV illuminated samples (Figures 5.19c–d). After one week of UV light exposure, rod-like shapes were still present, albeit severely deformed. And after two weeks of reaction time under UV light, no rod-like shape could be discerned. This could indicate, firstly, that the anionic sublattice was either rearranged or completely broken up after two weeks of continued exposure to UV light; and secondly, that surface ligands have been either partially removed, damaged or completely destroyed, rendering their functionality to stabilize NRs void. In any case, this reaction outcome did not meet the criteria for a

successful CE and will not be considered as such. Yet, in case of the UV illuminated experiment exposed for 7 d, the structure of the anionic sublattice was seemingly retained and can be considered a successful partial CE. But the TEM micrographs suggest, that the exposure to UV light limits the longevity of NRs considerably.

Likewise to previously observed experiments, EDX data featured a some linear behavior of the In incorporation. By fitting the linear regions, rate constants could be determined and plotted. The resulting Arrhenius plots from the reference experiments and the UV illuminated experiments are shown in Figure 5.20. Since the exposure to UV light had—albeit a small—effect under djurleite’s phase transition temperature, data points below and above T_{pt} were again fitted individually, to reveal possible different activation energies. And indeed, these Arrhenius plots generally resemble characteristics observed previously in Figure 5.12, with different slopes above and below T_{pt} . The fits of the linear regressions from the reference experiment in Figure 5.20a intersect at 0.00280 K^{-1} , translating to $84.1\text{ }^{\circ}\text{C}$. In case of the UV illuminated experiment, the intersection was at 0.00275 K^{-1} , which equals $91.1\text{ }^{\circ}\text{C}$. Both values are consistent with the previously determined phase transition temperature from DSC measurements of $87.5 \pm 1.1\text{ }^{\circ}\text{C}$ and $93.2\text{ }^{\circ}\text{C}$ from the intersection of the Arrhenius plot in Figure 5.12. Thus, the results from Figure 5.20 can be considered reliable to some degree.

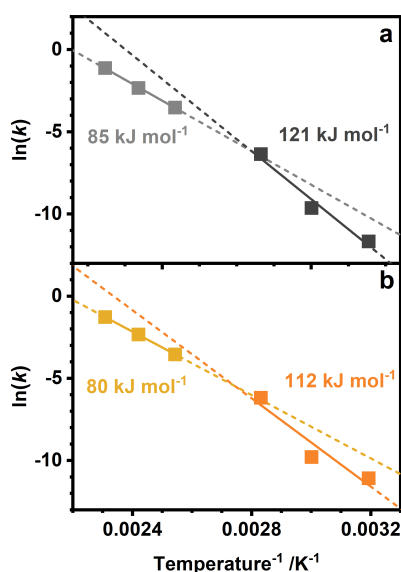


FIGURE 5.20: Arrhenius plot of (a) the reference experiments with linear regressions below T_{pt} in dark grey and above T_{pt} in light grey, and (b) the UV illuminated experiments with linear regressions below T_{pt} in orange and above T_{pt} in yellow, with extended dashed lines to visualize the points of intersection.

In regard to the effect of UV light exposure, the calculated activation energies are lower, both for below and above T_{pt} . However, the magnitude of the effects are minor. The difference in activation energy between the UV-exposed and reference experiment are 9 kJ mol^{-1} below T_{pt} (UV: $112 \pm 35\text{ kJ mol}^{-1}$; reference: $121 \pm 21\text{ kJ mol}^{-1}$). Above T_{pt} , the difference amounted to only 5 kJ mol^{-1} , with $80 \pm 1\text{ kJ mol}^{-1}$ in the UV illuminated case, and $85 \pm 3\text{ kJ mol}^{-1}$ in the case of the reference experiment. The small difference above T_{pt} is plausible, since the desired effect of illumination with UV light was to trigger a phase transition below T_{pt} , and as such, the effect of UV illumination above T_{pt} should be negligible, since the phase transition would have already been induced thermally anyway. But even though the difference in activation energy between the UV and reference experiment

is marginally higher below T_{pt} with 9 kJ mol^{-1} , compared to 5 kJ mol^{-1} above T_{pt} , the consideration of the margins of error, which are rather high in some cases, calls the effect of UV exposure into question.

Yet, an argument in favor of an effect of UV light exposure could be made as well. Let it be supposed, that the exposure of a CE reaction with UV light triggered a phase transition of djurleite below its usual T_{pt} . As a result, the activation energy would be lowered, compared to no exposure with UV light, but—importantly—no difference would be observable above T_{pt} , since the phase transition would already have occurred due to the passing of the phase transition temperature. Hence, the difference of activation energies between the two experiments should only be affected by the lowering of the activation energy below T_{pt} in the UV experiment. For the purpose of clarification, let ΔE_a be the difference of activation energies between the activation energy below T_{pt} , $E_{a\downarrow}$, and the activation energy above T_{pt} , $E_{a\uparrow}$

$$\Delta E_a = E_{a\downarrow} - E_{a\uparrow}. \quad (5.6)$$

As a result, the difference of activation energies of the UV-exposed experiment is $\Delta E_{a,\text{uv}} = 32 \text{ kJ mol}^{-1}$. In line with this reasoning, the effect of the UV light exposure can be calculated by the differences of activation energies

$$\Delta E_{a,\text{ref}} - \Delta E_{a,\text{uv}} = 36 \text{ kJ mol}^{-1} - 32 \text{ kJ mol}^{-1} = 4 \text{ kJ mol}^{-1}. \quad (5.7)$$

Even though the effect seems minor, the previously presented data could support these findings: The calculated activation energies in the previous section were $E_{a\downarrow} = 128 \pm 24 \text{ kJ mol}^{-1}$ and $E_{a\uparrow} = 91 \pm 10 \text{ kJ mol}^{-1}$, with a difference $\Delta E_a = 37 \text{ kJ mol}^{-1}$. In case of the reference experiment presented in this section, the difference was very similar with $\Delta E_a = 36 \text{ kJ mol}^{-1}$. The calculation of the activation energies rely on a large amount of data. Since the differences in activation energies are an almost exact match, these experiments constitute a solid experimental reproduction and support the previous findings. Following this argument, the small difference in activation energy between the non-illuminated and the UV experiment could indeed indicate an actual effect and the measurable reduction of the activation energy below T_{pt} as a result of UV light illumination.

Since arguments could be presented for and against the existence of an effect from UV light exposure on the CE reactions, no final conclusion can be drawn from the presented data. Uncertainty regarding the existence of the effect of UV light to trigger a phase transition below T_{pt} remains, as some experiments could not even reproduce the observed differences in In incorporation between the UV and the reference group.

Chapter 6

Summary

This work set out to examine the cation exchange (CE) from Cu_{2-x}S to wurtzite CuInS_2 in anisotropic nanocrystals (NCs). Slightly Cu-deficient djurleite nanorods (NRs) were chosen as an exemplary system. Djurleite NRs could be synthesized in a highly reproducible manner, yielding rods with aspect ratios of 2.1, with faceted surfaces and a hexagonal prism morphology. The crystal structures were consistent between individual NR batches and had comparable stoichiometries. This conformity allowed the treatment of all djurleite NR starting batches for subsequent CE reactions as interchangeable, without the need to differentiate between individual batches to justify certain reaction outcomes. Copper sulfide has a complex phase diagram and features a phase transition of bulk djurleite at 93°C .^[76,82,85,86] The phase transition temperature (T_{pt}) could be specified for djurleite NRs at a slightly lower temperature of $87.5 \pm 1.1^\circ\text{C}$, and resulted in a phase transition from djurleite to a mixture of djurleite and high chalcocite. This phase transition distinctly affected the kinetics and exchange mechanism of the reactions.

CE reactions were studied in a wide parameter range, from 40°C to 160°C , with reaction times between one minute and 47 days. Below T_{pt} , no full exchange could be observed. The atomic amount of In converged towards a saturation value, and In could only be detected at the surface of the NRs. The process was self-limiting in nature and resulted in the exchange of only approximately the first five surface layers. NRs were continuously etched with ongoing reaction times by trioctylphosphine (TOP) and trioctylphosphine oxide (TOPO), which were present in the reaction solution in order to stabilize the particles, as well as to facilitate the Cu extraction from the NRs, resulting in a length and width decrease over time.

Conversely, above T_{pt} full CE could be achieved. A successful CE would be characterized by the retention of the parent particle's morphology. A full CE, then, would be characterized by either the complete exchange of all atoms of one species, or by completely changing the crystal structure of the parent particles. In case of the CE reaction with djurleite, the final product was expected to be wurtzite CuInS_2 , since the anionic sublattices of both the djurleite and wurtzite phases are hexagonally close-packed. If all Cu atoms were to be exchanged with In, resulting in In_2S_3 , the anionic sublattice would be required to change its configuration from hexagonally close-packed to face-centered cubic, which is energetically unfavorable.

As observed with CE reactions below T_{pt} , the surface roughness of NRs also increased in experiments conducted above T_{pt} . But surprisingly, the surface roughness decreased distinctly after full CE and the faceting observed in the starting samples returned. A size decrease in length could be attributed to a lattice compression of S layers along the long axis of the NRs, following from the transformation to wurtzite. A decrease in particle width was likely the result from etching by TOP and TOPO, based on the continuous width decrease over time, while the decrease in length was constant. It was assumed that etching of the NR's tips was inhibited, as these facets are terminated by S layers, while the sides of the NRs featured both Cu and S, and could thus promote etching by Cu-affine molecules. The full transformation of djurleite NRs to the wurtzite CuInS_2 phase could be confirmed *via* diffraction patterns, featuring reflections only relating to the wurtzite phase, and atomic composition measurements, revealing nearly stoichiometric ratios of Cu, In and S. The quenching of the localized surface plasmon resonance (LSPR), characteristic of Cu-deficient copper sulfide phases, further indicated a full CE, and the determined band gap energy of 1.45 eV matched reported values in the literature. Elemental mapping of partially exchanged NRs confirmed the hypothesis of In only diffusing into the surface layers below T_{pt} , while revealing the emergence of In bands along the short axes of NRs above T_{pt} . These bands consisted of wurtzite CuInS_2 , which could be confirmed by comparing the lattice reflections in fast Fourier transforms (FFTs) of high-resolution transmission electron microscopy (HRTEM) micrographs of the exchanged bands to the unexchanged parts of the NRs. These wurtzite bands were always spanning the entire width of NRs and increased in length with time, until NRs were fully exchanged to CuInS_2 . Fast diffusion of In along the short NR axes stemmed from the special properties of the emerging high chalcocite phase above T_{pt} . Literature reports unusually high Cu diffusivities in high chalcocite, likely facilitating In diffusion inside the Cu layers perpendicular to the long axis of the NRs.^[87] Cu planes are separated by layers of the more rigid anionic S sublattice, through which the In diffusion is slower. An initial diffusion through the tips of NRs could not be observed and seems unlikely as well, since large ligands on the NR's surface like TOPO with steric hindrances can pack closer on a curved surface, i.e. near and at the tips, compared to less densely packed regions, favoring adsorption of the In precursor from the side of the NRs.

Atomic composition measurements revealed a reoccurring feature in all experiments, below and above T_{pt} : The In incorporation consistently evolved linearly at early reaction times, until a saturation regime manifested below 25 % In incorporation for experiments performed below T_{pt} , and around 25 % In for conditions above T_{pt} . The linear behavior suggested a pseudo-zero order rate law. The rate constants were determined from linear regressions and charted in an Arrhenius plot, from which activation energies of the rate-limiting steps could be extracted. The activation energy below T_{pt} was higher than above T_{pt} , confirming the observations of differing CE mechanisms below and above T_{pt} . Below T_{pt} , the activation energy was

calculated to be 128 kJ mol^{-1} , and to 91 kJ mol^{-1} above T_{pt} , amounting to a difference of 37 kJ mol^{-1} as a result of the phase transition. The results were further substantiated by the calculated phase transition temperature from the Arrhenius plot with 93.2°C , in accordance to the experimentally determined value of $87.5 \pm 1.1^\circ\text{C}$. Activation energies around 100 kJ mol^{-1} point towards a vacancy-mediated diffusion mechanism. Since djurleite has only eight vacancies per 376 atoms in a unit cell,^[103] and only surface layers could be exchanged below T_{pt} , the rate-limiting step was likely the creation of additional vacancies. This reasoning is in line with a reduction of the activation energy of 37 kJ mol^{-1} after the phase transition, as djurleite was still present in the phase mixture above T_{pt} , which increased the diffusivity of In through the Cu layers, but not through the S layers.

In conclusion, the complete CE from djurleite to wurtzite CuInS_2 in anisotropic NRs could be demonstrated successfully, under size and morphology retention. The limited amount of Cu vacancies in the djurleite phase inhibited the full CE, and instead only allowed surface layers to be exchanged to the wurtzite phase. The temperature-induced phase transition from djurleite to a phase mixture of djurleite and high chalcocite had a crucial effect on the CE mechanism and enabled the diffusion of In ions into the volume of the NRs. This resulted in the formation of wurtzite bands, which increased in size until a complete transformation to CuInS_2 was reached.

Chapter 7

Experimental Methods

7.1 Cu_{2-x}S Nanocrystal Synthesis

It is of paramount interest to produce monodisperse and rod-shaped nanocrystals with high reproducibility yielding similar Cu_{2-x}S stoichiometries. The hot injection and thermal decomposition methods are two possible approaches to achieve these goals. Here, the Cu_{2-x}S synthesis *via* thermal decomposition was adapted from the hot injection approach described by Kruszynska *et al.*^[80]

In a typical synthesis 0.363 g (2.00 mmol) copper(I)acetate (99%, abcr), stored in a glovebox under nitrogen atmosphere, was combined in a three-neck flask with 10 mL 1-octadecene (technical grade, 90%, Sigma-Aldrich), 7.5 mL *tert*-dodecanethiol (technical grade, $\geq 97\%$, Sigma-Aldrich) and 4 mL Cyanex (vacuum-conditioned for two hours prior) under nitrogen atmosphere. The reaction solution was then stirred under vacuum for one hour. Thereafter, the mixture was placed under nitrogen and kept at 130 °C for 30 min, at which point the solution color changed from a turbid, dark green to a clear amber color, sometimes even changing to a darker amber hue. The temperature was then raised to the growth temperature of 180 °C. The reaction was allowed to proceed for 15 min. The resulting product was rapidly cooled to room temperature with a water bath and washed three times in a glovebox by precipitation with a 1:1 (v:v) mixture of methanol and butanol in a centrifuge for 10 min at $10000 \times g$ and redispersed in toluene.

7.2 Cation Exchange Reaction

Cation exchange For a typical cation exchange reaction an entire batch of Cu_{2-x}S NCs was dried under nitrogen flow and redispersed in 20 mL 1-octadecene (technical grade, 90%, Sigma-Aldrich), resulting in a concentration (relative to copper) of 0.15 mol L^{-1} . 2.0 mL (0.30 mmol Cu) of that solution was placed in a three-neck flask and diluted with 8 mL 1-octadecene. The mixture was stirred under vacuum for an hour. Afterwards, the solution was set under nitrogen atmosphere and heated to the desired reaction temperature.

Then, similar to a hot injection, 2.0 mL (0.60 mmol In) indium stock solution (described in the following paragraph) and 0.20 mL trioctylphosphine (technical grade,

90%, Sigma-Aldrich) were swiftly injected into the flask. The reaction was typically allowed to proceed for a few minutes up to several days. Aliquots were taken in regular intervals.

The product was washed three times under ambient conditions by precipitation with a 1:1 (v:v) mixture of methanol and butanol in a centrifuge for 10 min at $10000 \times g$ and redispersed in toluene.

Indium stock solution The aforementioned indium stock solution was the solely used In source for all performed CE reactions. For a typical stock solution 14.5 g (37.5 mmol) trioctylphosphine oxide (99%, Sigma-Aldrich) and 1.67 g (7.50 mmol) indium(III) chloride (99.999%, trace metals basis, Sigma-Aldrich, stored in a nitrogen-filled glovebox) were placed in a three-neck flask. Under nitrogen atmosphere 25 mL 1-octadecene was added, resulting in a concentration of 0.30 mol L^{-1} . The mixture was stirred under vacuum for one hour. Afterwards, the flask was placed under nitrogen again and heated to $170 \text{ }^\circ\text{C}$ for 30 min. The stock solution was then continuously stirred and kept at $40 \text{ }^\circ\text{C}$ to ensure that trioctylphosphine oxide would not precipitate.

7.3 Characterization Methods

The following section list the various characterization methods utilized in this work, with specifications of the measurement instruments and detailing the sample preparation protocols.

7.3.1 Differential Scanning Calorimetry

DSC was used to determine the phase transition temperature of a djurleite NR sample. Data was obtained from a NETZSCH DSC 204 F1 Phoenix heat-flux calorimeter.

DSC sample preparation A concentrated NR suspension was dried under nitrogen flow and transferred into an aluminium crucible (weighed before and after sample filling), and closed with an aluminium lid *via* a sealing press. A measurement protocol was specified to heat the sample with a rate of 1 K min^{-1} from $20 \text{ }^\circ\text{C}$ to $160 \text{ }^\circ\text{C}$ and subsequently cool down the sample to $20 \text{ }^\circ\text{C}$ with the same (but negative) rate, concluding one cycle. The protocol included three cycles. The first cycle was discounted, as it is usually shifted relative to following measurements. The reasoning is the contact area between the sample and the heating element, which is usually maximized during during the first measurement cycle, resulting in reproducible results after the first cycle.

7.3.2 Energy-Dispersive X-ray Spectroscopy

EDX was used to measure the atomic composition of ensemble NR samples and to map the atomic composition of individual NRs. The atomic compositions were obtained either *via* HRTEM or SEM, and atomic composition maps were acquired *via* HRTEM.

EDX measurements *via* HRTEM were obtained from a JEOL JEM-2200FS (UHR) equipped with a JEOL JED-2300T analyzer with a 50 mm² Si(Li) detector, at an acceleration voltage of 200 kV.

EDX measurements *via* SEM were acquired with a Zeiss MA 10, equipped with an Oxford Instruments INCAx-act analyzer with a 10 mm² Si drift detector, usually operated at an acceleration voltage of 10 kV. The measurements in the SEM were performed over a wide area (usually 10⁷ nm² to 10⁸ nm²) on multiple sample locations (usually 5 to 10), in order to include several thousand NRs in the data acquisition.

EDX sample preparation Samples measured *via* SEM were prepared by drop-casting 10 μ L to 30 μ L of a concentrated NR suspension in toluene onto a small Si wafer piece, usually about 25 mm², letting excess liquid evaporate, and repeating the process until a visibly thick layer was obtained. Sample preparation for TEM measurements are specified below in Section 7.3.3.

7.3.3 Transmission Electron Microscopy

Conventional TEM micrographs were captured with a JEOL JEM-1011 microscope operating at an acceleration voltage of 100 kV. HRTEM measurements were carried out on a JEOL JEM-2200FS (UHR), equipped with a CESCOR and CETCOR corrector, working at an acceleration voltage of 200 kV.

TEM sample preparation Samples for TEM and HRTEM investigation were prepared likewise: 10 μ L of a diluted NR suspension in toluene were drop-casted on a Cu or Ni grid (400 mesh) and excess liquid was removed from the bottom with a filter paper.

7.3.4 UV-Vis-NIR Spectroscopy

Absorbance spectra were measured with a Varian Cary 500 spectrometer. In order to eliminate the influence of scattering from turbid samples on the absorbance, a labsphere DRA-CA-5500 was employed as an integrating sphere.

UV-Vis-NIR spectroscopy sample preparation Samples for absorbance measurements were prepared by washing the NR suspension in toluene with a 1:1 (v:v) mixture of butanol and methanol and centrifugation at 10000 \times g. The supernatant was

discarded and the NRs were redispersed in 1,1,2-trichloroethene, a solvent with minimal absorption in the NIR region.

7.3.5 X-ray Diffraction

Diffraction patterns were acquired with a Philips X'Pert Pro MPD diffractometer with a Bragg-Brentano geometry, equipped with a Philips high intensity ceramic sealed tube (3 kW) as a Cu K α X-ray source with a wavelength of 1.5405 Å.

XRD sample preparation XRD samples were prepared by drop-casting a concentrated NR suspension in toluene on a Si wafer substrate. The solvent was evaporated and the drop-casting process was repeated until a visibly thick layer was formed. Temperature-dependent measurements were obtained by preparing sealed quartz capillaries containing a concentrated NR suspension.

Appendix A

Supporting Information

A.1 Supporting Information regarding Chapter 4

A.1.1 Size Distributions of Starting Samples

Presented in the following are the size distributions of all individual starting samples, discussed in Section 4.1. The particle sizes plotted in Figure 4.2a are based upon these data.

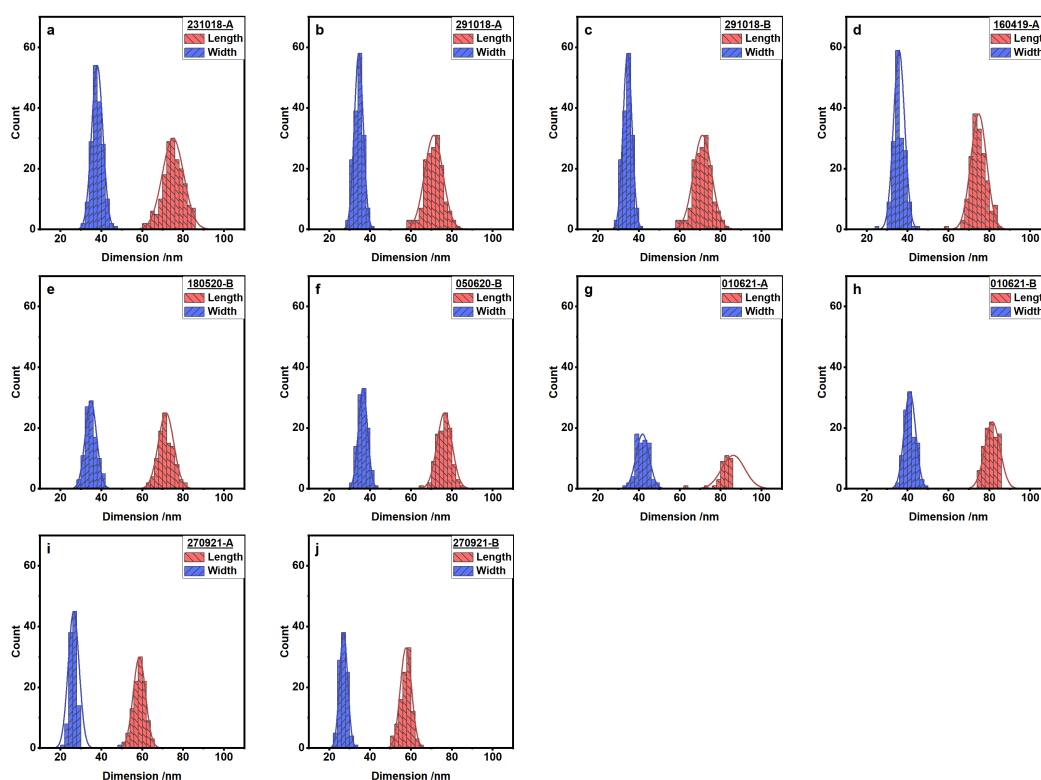


FIGURE A.1: Particle size distribution histograms of samples (a) 231018-A, (b) 291018-A, (c) 291018-B, (d) 160419-A, (e) 180520-B, (f) 050620-B, (g) 010621-A, (h) 010621-B, (i) 270921-A and (j) 270921-B.

A.1.2 Properties of Sample 080222-B

Sample 080222-B was used for the DSC measurements. As the sample was not used for other CE experiments, it is not presented in Chapter 4, but instead introduced

here. The sample had a typical composition, determined *via* EDX measurement, of 64.2 % Cu and 35.8 % S, resulting in a Cu-deficient composition of $\text{Cu}_{1.79}\text{S}$. The Cu-deficient composition was in agreement to the crystal phase, which was identified as djurleite, as seen in Figure 4.

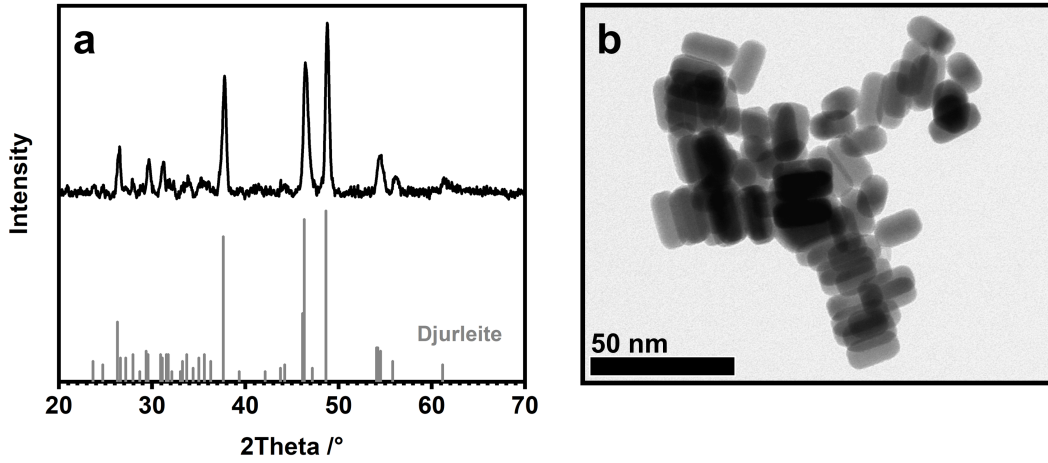


FIGURE A.2: (a) Powder diffraction pattern of sample 080222-B in black, with the djurleite $\text{Cu}_{1.94}\text{S}$ reference pattern (PDF no. 00-023-0959) in grey and (b) a TEM micrograph of the same sample, showing the typical rod-like morphology.

A.2 Supporting Information regarding Chapter 5

A.2.1 Calculation of Atoms in a NR Before and After a CE Reaction

The amount of atoms before an exchange, of sample 270921-A, and after the exchange with a reaction time of 24 h at 120°C , was calculated to determine if the hypothesis of a lattice compression explaining the particle size decrease after the reaction was plausible.

The amount of atoms per NR $N_{\text{atom,NR}}$ can be expressed as the product of the number of unit cells per NR $N_{\text{uc,NR}}$ and the amount of atoms per unit cell $N_{\text{atom,uc}}$

$$N_{\text{uc,NR}} = \frac{V_{\text{NR}}}{V_{\text{uc}}} \quad (\text{A.1})$$

$$N_{\text{atom,NR}} = N_{\text{uc,NR}} \cdot N_{\text{atom,uc}} \quad (\text{A.2})$$

with the cell parameters of djurleite and wurtzite CuInS_2 shown in Table A.1. To calculate the volume of a NR, the shape of a NR was approximated by a cylinder with

$$V_{\text{NR}} = \pi \cdot \left(\frac{W}{2}\right)^2 \cdot L \quad (\text{A.3})$$

with the width of a NR W and the length L .

The calculations were performed with the lengths and widths obtained from the size distribution histograms shown in Figure A.3. The results of the calculations are

shown in Table A.2. The amounts of atoms per NR are the same order of magnitude for both samples, and values are within the other samples respective margin of error.

TABLE A.1: Lattice parameters of djurleite $\text{Cu}_{1.94}\text{S}$ and wurtzite CuInS_2 .^[82,94] Note that CuInS_2 has only two atoms per unit cell, because the cations occupy the same lattice site, each with a probability of 50%.

	Djurleite $\text{Cu}_{1.94}\text{S}$	Wurtzite CuInS_2
Crystal system	monoclinic	hexagonal
Space group	$P 2_1/n$	$P 6_3 m c$
a	26.897 Å	3.897 Å
b	15.745 Å	3.897 Å
c	13.565 Å	6.441 Å
α	90°	90°
β	90.13°	90°
γ	90°	120°
Atoms per unit cell	376	2
Unit cell volume	5.74 nm ³	0.021 nm ³
Density	5.75 g cm ⁻³	4.75 g cm ⁻³

TABLE A.2: Results of the calculations for the amount of numbers of atoms per NR, with the volume of a NR V_{NR} , the number of unit cells per NR $N_{\text{uc,NR}}$ and the number of atoms per NR $N_{\text{atom,NR}}$.

Sample	Size of NR /nm	$V_{\text{NR}}/\text{nm}^3$	$N_{\text{uc,NR}}$	$N_{\text{atom,NR}}$
270921-A	58.6±3.0 26.4±2.7	$3.21 \cdot 10^4$ $\pm 8.15 \cdot 10^4$	$5.58 \cdot 10^3$ $\pm 1.42 \cdot 10^3$	$2.10 \cdot 10^6$ $\pm 5.36 \cdot 10^5$
CE@120_24h	55.3±3.3 24.6±1.4	$2.63 \cdot 10^4$ $\pm 4.58 \cdot 10^3$	$1.25 \cdot 10^6$ $\pm 2.18 \cdot 10^5$	$2.50 \cdot 10^6$ $\pm 4.35 \cdot 10^5$

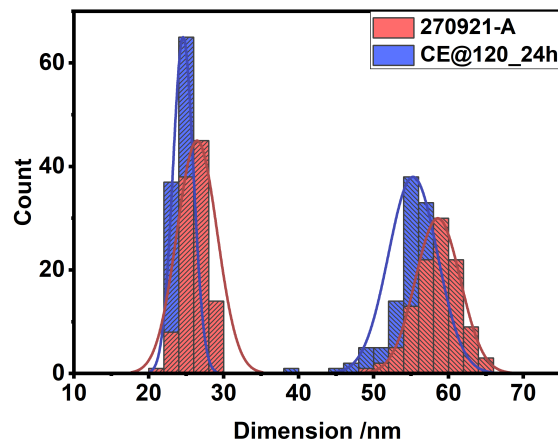


FIGURE A.3: Size distributions of starting sample 270921-A, before CE, and of a sample after a CE reaction at 120 °C after 24 h of reaction time, referenced in Table A.2.

A.2.2 Plot of the Absorbance Curve Integrals

The areas under the curves of Figure 5.6a were integrated between 650 nm and 1600 nm, and plotted against the reaction time in minutes in Figure A.4. The first data points follow a linear behavior, represented by a linear regression curve in grey.

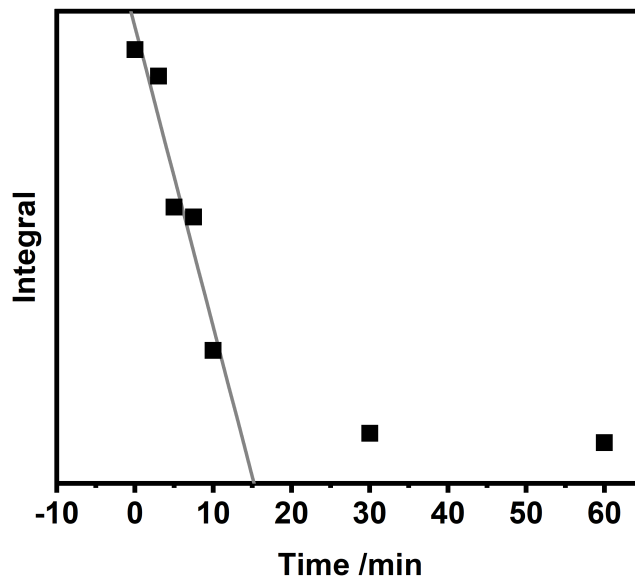


FIGURE A.4: Plot of the integrated areas of the individual absorbance curves, shown in Figure 5.6a, against the reaction time, with a linear regression of the first five data points in grey, with a coefficient of determination $R^2 = 0.92$.

A.2.3 Calculation of the Amount of Atoms on the Surface of a NR

In order to calculate the surface atoms of a NR, firstly, the amount of atoms in a NR $N_{\text{atom,NR}}$ (here of sample 270921-A, with the mean width of 26.4 nm and length of 58.6 nm) had to be calculated with Equation A.2, assuming a perfect cylindrical shape. The calculation of surface atoms was based on the assumption, that the expanse of a surface layer could be approximated by the length of the average length of a Cu-S bond distance in djurite of 2.48 Å.^[82] In order to calculate the amount of surface atoms in n layers, the volume of a hollow cylinder $V_{\text{NR,hollow}}$, representing the NR shell with a thickness of n layers, was calculated with

$$V_{\text{NR,hollow}} = V_{\text{NR}} - \left(\pi \cdot \left(\frac{W}{2} - 2nr_{\text{Cu-S}} \right)^2 \cdot (L - 2nr_{\text{Cu-S}}) \right). \quad (\text{A.4})$$

The calculated volumes were converted to number of atoms, by calculating the amount of unit cells per volume with Equation A.1, from which the atoms per volume were calculated with Equation A.2. From this, the volume ratios of the hollow

cylinders, i.e. volumes of one, two or three surface layers, to the total cylinder volume was calculated to represent the amount of surface atoms in n layers. The results are shown in Table A.3.

TABLE A.3: Results from the calculation of surface atoms in the first n layers of the average sized NR of sample 270921-A, with the volume of a NR V_{NR} and the the volume of the n number of layers, respectively, and the ratios of surface to volume atoms in percent.

	Volume /nm ³	Atoms in n Layers	Surface to Volume Ratio /%
NR	$3.21 \cdot 10^4$	$2.10 \cdot 10^6$	—
1 layer	$2.62 \cdot 10^3$	$1.71 \cdot 10^5$	8.16
2 layers	$5.10 \cdot 10^3$	$3.34 \cdot 10^5$	15.91
3 layers	$7.47 \cdot 10^3$	$4.89 \cdot 10^5$	23.27
4 layers	$9.70 \cdot 10^3$	$6.35 \cdot 10^5$	30.25
5 layers	$1.88 \cdot 10^4$	$7.73 \cdot 10^5$	36.84

A.2.4 Additional Information on the Crystal Phase Determination *via* FFT

In order to determine the FFT reflections of the suspected wurtzite band along the NR shown in Figure A.5a, the difference between the FFTs of the entire micrograph and the area of the suspected band (Figure A.5c) were determined. Thus, reflections originating from the djurleite phase (present in the micrograph A.5a from unexchanged parts of the intermediate sample with only 8.6 % In incorporated) could be excluded, leaving only reflections originating from a different phase than djurleite. These reflections in Figure A.5e could be matched to the wurtzite phase, by determining the associated Miller indices.

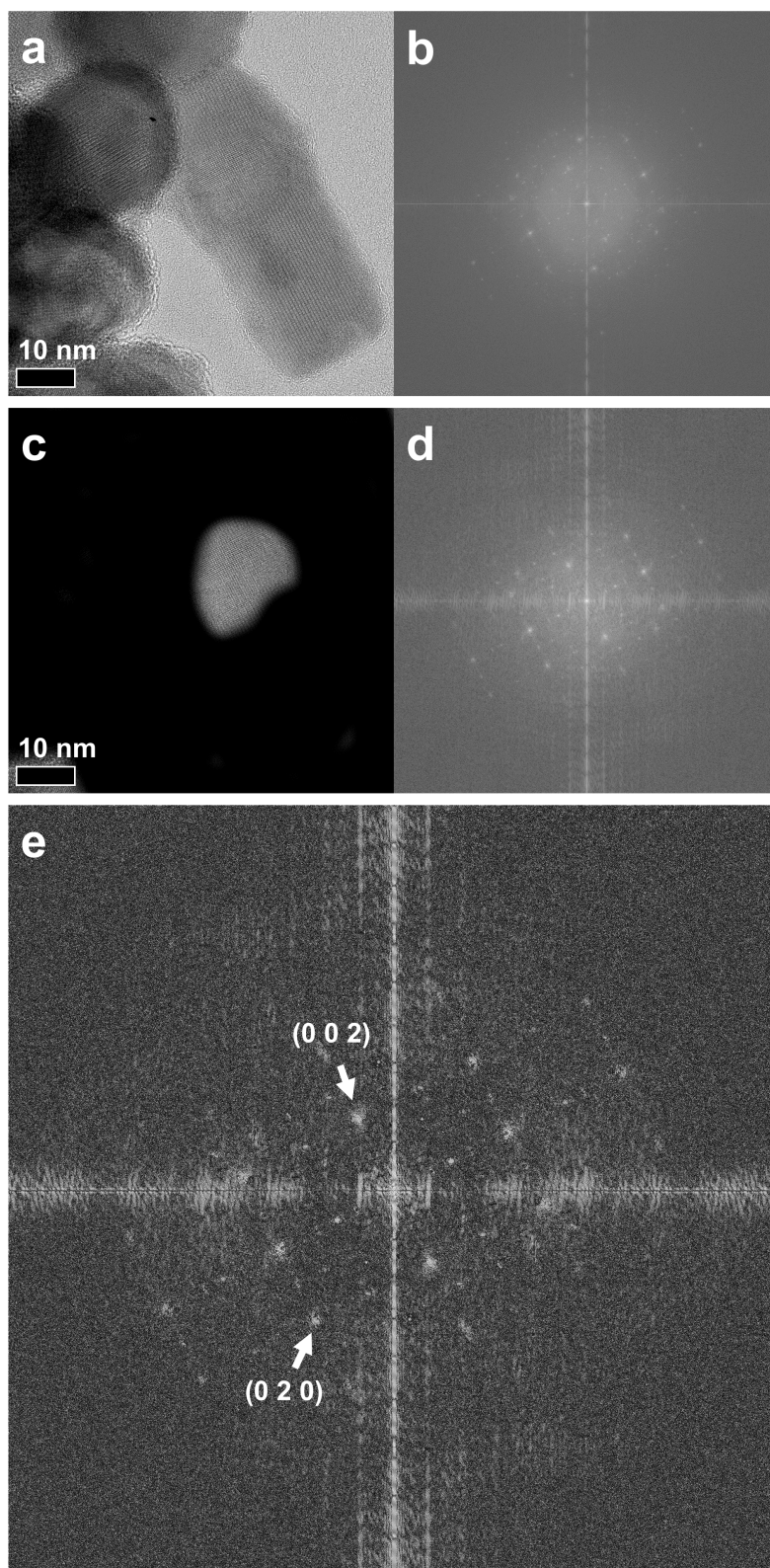


FIGURE A.5: (a) TEM micrograph, shown in Figure 5.8, of a CE reaction at 120 °C after 5 min and (b) the FFT thereof, (c) the area of suspected CE with the remaining area blackened and (d) the resulting FFT and (e) the difference of b and d.

A.2.5 Specifications regarding CE experiments under UV light Illumination

The UV reactor housed four Philips 9 W UV lights of the type PL-S BLB 2P Blacklight. The lamps emitted UV light with a wavelength of $\lambda = 365$ nm, as shown in the lamp spectrum in Figure A.6.

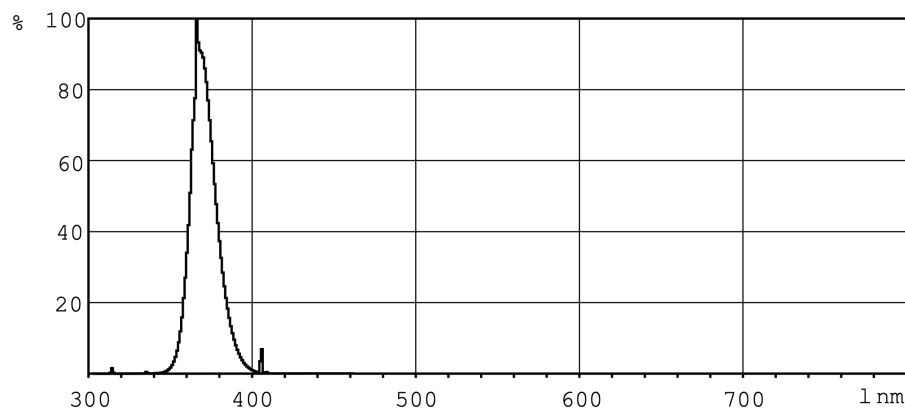








FIGURE A.6: Lamp spectrum for the employed UV lights from Philips, with a maximum emission wavelength of 365 nm.^[128]






Appendix B

Safety Data

The following table shows a list of utilized chemicals with hazard and precautionary statements.

TABLE B.1: A listing of all employed chemicals during the practical part of this work, including the GHS symbols, hazard and precautionary statements.^[129]

Substance	GHS Symbol	Hazard Statement(s)	Precautionary Statement(s)
1-Butanol		H226, H302, H315, H318, H335, H336	P210, P260, P280, P302+P352, P304+P340, P305+P351+P338
1-Octadecene		H304	P301+P310, P331, P405, P501
1,1,2-Trichloroethene		H315, H319, H336, H341, H350	P280, P302+P352, P305+P351+P338, P312, P403+P233, P501
Copper(I) acetate		H315, H319	P264, P280, P302+P352, P337+P313, P362+P364, P332+P313
Cyanex 923 ^[130]		H302, H314, H400, H410	P261, P273, P280, P301+P312, P302+P350, P305+P351+P338
Indium(III) chloride		H314, H372, H412	P260, P372, P280, P303+P361+P353, P305+P351+P338, P314

Substance	GHS Symbol	Hazard Statement(s)	Precautionary Statement(s)
Methanol		H225, H301+H311+H331, H370	P210, P233, P280, P301+P310, P303+P361+P353, P304+P340+P311
<i>tert</i> -Dodecanethiol		H315, H317, H410	P261, P264, P272, P273, P280, P305+P352
Toluene		H225, H304, H315, H336, H361d, H373, H412	P202, P210, P273, P301+P310, P301+P361+P353, P331
Tri- <i>n</i> -octylphosphine		H314	P264, P280, P301+P330+P331, P303+P361+P351, P304+P340, P305+P351+P338, P310
Tri- <i>n</i> -octylphosphine oxide		H315, H318, H412	P264, P273, P280, P305+P352, P305+P351+P338+P310

The following table lists information regarding carcinogenic, mutagenic and reprotoxic (CMR) chemicals of the above table B.1.

TABLE B.2: Employed chemicals which are classified under the CLP regulation (for classification, labelling and packaging) of the European Union (EC) No 1272/2008 as carcinogenic, mutagenic and reprotoxic (CMR) substances; the table is itemized by carcinogenic (K), mutagenic (M), teratogenic, i.e. damaging to embryological development (R_D) and fertility-impairing (R_F).^[131]

CAS number	Substance	Amount Used	K	M	R _D	R _F
79-01-6	Trichloroethene	1 L	1B	2		
67-56-1	Methanol	20 L	2			
108-88-3	Toluene	20 L			2	

Appendix C

Acknowledgements

An dieser Stelle möchte ich Personen danken, die zu einem erheblichen Teil zur Entstehung dieser Arbeit beigetragen haben.

An erster Stelle möchte ich mich bei Prof. Dr. Horst Weller für die Aufnahme in den Arbeitskreis bedanken, in dem ich unter hervorragenden Bedingungen kreativ arbeiten, forschen und denken durfte. Vielen Dank für das entgegengebrachte Vertrauen, die stetige Unterstützung, die freundliche Zusammenarbeit und die konstruktiven wissenschaftlichen Diskussionen.

Bei Prof. Dr. Alf Mews möchte ich mich für die Übernahme des Zweitgutachtens bedanken.

Insbesondere möchte ich mich bei Dr. Cristina Palencia Ramírez für die hervorragende Betreuung während meiner Forschungszeit, die kontinuierliche Unterstützung und Motivation, die zahlreichen hilfreichen Diskussionen und netten Gespräche, sowie die enge und freundliche Zusammenarbeit bedanken.

Des Weiteren möchte ich mich bei Dr. Tobias Vossmeier für seine Funktion als Co-Betreuer bedanken.

Weiterhin möchte ich dem Hamburg Centre for Ultrafast Imaging (CUI) für die finanzielle Unterstützung bei Dienstreisen und Weiterbildungen danken, sowie den Mitarbeitenden des CUI Offices und der Graduiertenschule für ihre organisatorische Unterstützung.

Marion Manin und Martina Krasa möchte ich für ihre freundliche und kompetente Hilfe bei jeglichen organisatorischen Anliegen danken.

Meinen Praktikant*innen Julia, Michael und Vi Quint danke ich für ihre wertvolle Arbeit im Labor und die Erhebung hilfreicher Daten.

Außerdem möchte ich mich bei Dr. Cristina Palencia Ramírez, Dr. Robert Seher und Jan Krohn bedanken, mit denen ich am DESY viele Strahlenzeiten an unterschiedlichen Beamlines organisiert, vor- und nachbereitet habe und viele aufregende Tages- und insbesondere Nachtschichten erleben durfte.

Vielen Dank an Andreas Kornowski, Robert Schön und Stefan Werner für die Anfertigung zahlreicher elektronenmikroskopischer Aufnahmen. Und vielen Dank an Almut Barck, Isabelle Nevoigt und Nina Schober für die Aufnahme von Röntgendiffraktogrammen.

Für die Einführung und Unterstützung bei der Bedingung des Transmissions-elektronenmikroskops möchte ich mich erneut bei Stefan Werner bedanken. Für die Einführung in die Rasterelektronenmikroskopie und die Hilfe bei Problemen beim Messen möchte ich Dr. Hauke Heller danken. Und für die Einführung in die TGA und DSC möchte ich Dr. Kathrin Hoppe danken.

Ferner möchte ich meinen Kolleginnen und -kollegen der ersten Stunde aus Büro 353 für die schöne und stets kreative Büroatmosphäre danken: Dr. Friederieke Gorris, Dr. Lasse Habercorn, Jan Krohn, Dr. Robert Seher und Dr. Sarah Wölper.

Weiterhin möchte ich mich bei meiner zweiten Bürogeneration bei Dr. Rieke Koll und Dr. Marius Schumacher für die tolle und kommunikative Zusammenarbeit bedanken.

Der dritten Generation in Büro 353 mit Julia Funk, Sebastian Graf und Sönke Wengler-Rust danke ich für die stets gute Stimmung und angenehme Arbeitsatmosphäre.

Außerdem möchte ich allen übrigen ehemaligen Mitgliedern des Arbeitskreises Bendix, Clemens, Daniel, Gregor, Hauke, Jil, Maik, Michael und Steffen, sowie den aktuellen Mitgliedern Agnes, Ahir, Artur, Elena, Finn, Hendrik, Jana, Julian, Markus, Nancy, Roger, Sebastian, Sophia und Svenja für die schöne und unterhaltsame Zeit, sowie die netten Gespräche danken.

Schließlich möchte ich mich bei meinen Freunden bedanken, die mein Leben außerhalb der Uni mit so viel Freude, Leben, Liebe, Lachen, Musik und Motivation füllen, und für ihre Unterstützung in allen erdenklichen Lebenslagen. Danke auch an meinen Vater Michael Thiel und Karl-Heinz Kroschowski. In ganz besonderem Maße möchte ich mich bei meiner Mutter Andrea Kroschowski für ihre immerwährende, unerschöpfliche und liebevolle Unterstützung bedanken. Und ein besonderer Dank an meine Freundin Celina, dass du immer für mich da bist und mein Leben bereicherst.

Appendix D

Declaration of Authorship

Hiermit versichere ich an Eides statt, die vorliegende Dissertation selbst verfasst und keine anderen als die angegebenen Hilfsmittel benutzt zu haben. Die eingereichte schriftliche Fassung entspricht der auf dem elektronischen Speichermedium. Ich versichere, dass diese Dissertation nicht in einem früheren Promotionsverfahren eingereicht wurde.

Hamburg, den 14.03.2023

Felix Thiel

Bibliography

- [1] Efros, A. L.; Efros, Al. L. Interband absorption of light in a semiconductor sphere. *Soviet Physics Semiconductors* **1982**, *16*, 772–775.
- [2] Rossetti, R.; Nakahara, S.; Brus, L. E. Quantum size effects in the redox potentials, resonance Raman spectra, and electronic spectra of CdS crystallites in aqueous solution. *The Journal of Chemical Physics* **1983**, *79*, 1086–1088.
- [3] Bastard, G.; Mendez, E.; Chang, L.; Esaki, L. Variational calculations on a quantum well in an electric field. *Physical Review B* **1983**, *28*, 3241.
- [4] Brus, L. E. Electron–electron and electron-hole interactions in small semiconductor crystallites: The size dependence of the lowest excited electronic state. *The Journal of Chemical Physics* **1984**, *80*, 4403–4409.
- [5] Weller, H.; Koch, U; Gutierrez, M; Henglein, A. Photochemistry of colloidal metal sulfides. 7. Absorption and fluorescence of extremely small ZnS particles (the world of the neglected dimensions). *Berichte der Bunsengesellschaft für physikalische Chemie* **1984**, *88*, 649–656.
- [6] Alivisatos, A. P.; Harris, A.; Levinos, N.; Steigerwald, M.; Brus, L. Electronic states of semiconductor clusters: Homogeneous and inhomogeneous broadening of the optical spectrum. *The Journal of Chemical Physics* **1988**, *89*, 4001–4011.
- [7] Bawendi, M. G.; Steigerwald, M. L.; Brus, L. E. The Quantum Mechanics of Larger Semiconductor Clusters (“quantum dots”). *Annual Review of Physical Chemistry* **1990**, *41*, 477–496.
- [8] Weller, H. Colloidal Semiconductor Q-Particles: Chemistry in the Transition Region Between Solid State and Molecules. *Angewandte Chemie - International Edition* **1993**, *32*, 41–53.
- [9] Ekimov, A. Growth and optical properties of semiconductor nanocrystals in a glass matrix. *Journal of Luminescence* **1996**, *70*, 1–20.
- [10] EU Commission, Commission recommendation of 18 October 2011 on the definition of nanomaterial (2011/696/EU). *Official Journal of the European Union* **2011**, *275*, 38.
- [11] EU Commission, Commission recommendation of 10 June 2022 on the definition of nanomaterial (2022/C 229/01). *Official Journal of the European Union* **2022**, *229*, 1–5.

- [12] Talapin, D. V.; Lee, J.-S.; Kovalenko, M. V.; Shevchenko, E. V. Prospects of Colloidal Nanocrystals for Electronic and Optoelectronic Applications. *Chemical Reviews* **2010**, *110*, 389–458.
- [13] Holder, E.; Tessler, N.; Rogach, A. L. Hybrid nanocomposite materials with organic and inorganic components for opto-electronic devices. *Journal of Materials Chemistry* **2008**, *18*, 1064–1078.
- [14] Xia, F.; Wang, H.; Xiao, D.; Dubey, M.; Ramasubramaniam, A. Two-dimensional material nanophotonics. *Nature Photonics* **2014**, *8*, 899–907.
- [15] Hirohata, A.; Takanashi, K. Future perspectives for spintronic devices. *Journal of Physics D: Applied Physics* **2014**, *47*, 193001.
- [16] Yan, Y.; Du, J. S.; Gilroy, K. D.; Yang, D.; Xia, Y.; Zhang, H. Intermetallic nanocrystals: Syntheses and catalytic applications. *Advanced Materials* **2017**, *29*, 1605997.
- [17] Ramos, A. P.; Cruz, M. A.; Tovani, C. B.; Ciancaglini, P. Biomedical applications of nanotechnology. *Biophysical Reviews* **2017**, *9*, 79–89.
- [18] Mekis, I.; Talapin, D. V.; Kornowski, A.; Haase, M.; Weller, H. One-Pot Synthesis of Highly Luminescent CdSe/CdS Core–Shell Nanocrystals via Organometallic and “Greener” Chemical Approaches. *Journal of Physical Chemistry B* **2003**, *107*, 7454–7462.
- [19] Yin, Y.; Alivisatos, A. P. Colloidal nanocrystal synthesis and the organic-inorganic interface. *Nature* **2005**, *437*, 664–670.
- [20] Peng, X.; Manna, L.; Yang, W.; Wickham, J.; Scher, E.; Kadavanich, A.; Alivisatos, A. P. Shape control of CdSe nanocrystals. *Nature* **2000**, *404*, 59–61.
- [21] Talapin, D. V.; Rogach, A. L.; Kornowski, A.; Haase, M.; Weller, H. Highly Luminescent Monodisperse CdSe and CdSe/ZnS Nanocrystals Synthesized in a Hexadecylamine–Trioctylphosphine Oxide–Trioctylphosphine Mixture. *Nano Letters* **2001**, *1*, 207–211.
- [22] Tomić, S.; Bernasconi, L.; Searle, B. G.; Harrison, N. M. Electronic and optical structure of wurtzite CuInS₂. *Journal of Physical Chemistry C* **2014**, *118*, 14478–14484.
- [23] Trizio, L. D.; Manna, L. Forging Colloidal Nanostructures via Cation Exchange Reactions. *Chemical Reviews* **2016**, *116*, 10852–10887.
- [24] Talapin, D. V.; Nelson, J. H.; Shevchenko, E. V.; Aloni, S.; Sadtler, B.; Alivisatos, A. P. Seeded Growth of Highly Luminescent CdSe/CdS Nanoheterostructures with Rod and Tetrapod Morphologies. *Nano Letters* **2007**, *7*, 2951–2959.
- [25] Palencia, C.; Seher, R.; Krohn, J.; Thiel, F.; Lehmkuhler, F.; Weller, H. An in situ and real time study of the formation of CdSe NCs. *Nanoscale* **2020**, *12*, 22928–22934.

- [26] Rivest, J. B.; Jain, P. K. Cation exchange on the nanoscale: An emerging technique for new material synthesis, device fabrication, and chemical sensing. *Chemical Society Reviews* **2013**, *42*, 89–96.
- [27] Zhou, H.; Sasahara, H.; Honma, I.; Komiyama, H.; Haus, J. W. Coated Semiconductor Nanoparticles: The CdS/PbS System's Photoluminescence Properties. *Chemistry of Materials* **1994**, *6*, 1534–1541.
- [28] Mews, A.; Eychmüller, A.; Giersig, M.; Schooss, D.; Weller, H. Preparation, Characterization, and Photophysics of the Quantum Dot Quantum Well System Cadmium Sulfide/Mercury Sulfide/Cadmium Sulfide. *Journal of Physical Chemistry* **1994**, *98*, 934–941.
- [29] Son, D. H.; Hughes, S. M.; Yin, Y.; Alivisatos, A. P. Cation Exchange Reactions in Ionic Nanocrystals. *Science* **2004**, *306*, 1009–1013.
- [30] Jeong, U.; Camargo, P.; Lee, Y.; Xia, Y. Chemical Transformation: A Powerful Route to Metal Chalcogenide Nanowires. *Journal of Materials Chemistry* **2006**, *16*, 3893–3897.
- [31] Camargo, P.; Lee, Y.; Jeong, U.; Z., Z.; Xia, Y. Cation Exchange: A Simple and Versatile Route to Inorganic Colloidal Spheres with the Same Size but Different Compositions and Properties. *Langmuir* **2007**, *23*, 2985–2992.
- [32] Steimle, B. C.; Fenton, J. L.; Schaak, R. E. Rational construction of a scalable heterostructured nanorod megalibrary. *Science* **2020**, *367*, 418–424.
- [33] Aldaye, F. A.; Palmer, A. L.; Sleiman, H. F. Assembling Materials with DNA as the Guide. *Science* **2008**, *321*, 1795–1799.
- [34] Balazs, A. C.; Emrick, T.; Russell, T. P. Nanoparticle Polymer Composites: Where Two Small Worlds Meet. *Science* **2006**, *314*, 1107–1110.
- [35] Boal, A. K.; Ilhan, F.; DeRouchey, J. E.; Thurn-Albrecht, T.; Russell, T. P.; Rotello, V. M. Self-assembly of nanoparticles into structured spherical and network aggregates. *Nature* **2000**, *404*, 746–748.
- [36] Glotzer, S. C.; Solomon, M. J. Anisotropy of building blocks and their assembly into complex structures. *Nature Materials* **2007**, *6*, 557–562.
- [37] Huynh, W. U.; Dittmer, J. J.; Alivisatos, A. P. Hybrid Nanorod-Polymer Solar Cells. *Science* **2002**, *295*, 2425–2427.
- [38] Leach, A. D.; Shen, X.; Faust, A.; Cleveland, M. C.; Croix, A. D. L.; Banin, U.; Pantelides, S. T.; Macdonald, J. E. Defect Luminescence from Wurtzite CuInS₂ Nanocrystals: Combined Experimental and Theoretical Analysis. *Journal of Physical Chemistry C* **2016**, *120*, 5207–5212.
- [39] Scheer, R.; Walter, T.; Schock, H.; Fearheiley, M.; Lewerenz, H. CuInS₂ based thin film solar cell with 10.2% efficiency. *Applied Physics Letters* **1993**, *63*, 3294–3296.

- [40] Ibach, H.; Lüth, H., *Festkörperphysik: Einführung in die Grundlagen*, 7. Auflage; Springer-Verlag: Munich, Germany, 2009.
- [41] Kittel, C., *Einführung in die Festkörperphysik*, 14. Auflage; Oldenbourg Verlag: Munich, Germany, 2006.
- [42] Yeh, C. Y.; Lu, Z. W.; Froyen, S.; Zunger, A. Zinc-blende–wurtzite polytypism in semiconductors. *Physical Review B* **1992**, *46*, 10086–10097.
- [43] Koo, B.; Patel, R. N.; Korgel, B. A. Synthesis of CuInSe₂ Nanocrystals with Trigonal Pyramidal Shape. *Journal of the American Chemical Society* **2009**, *131*, 3134–3135.
- [44] Suryanarayana, C.; Norton, M. G., *X-Ray Diffraction*, 1st ed.; Springer Science + Business Media: New York City, New York, 1998.
- [45] Atkins, P. W.; de Paula, J., *Physikalische Chemie*, 5. Auflage; WILEY-VCH Verlag GmbH & Co. KGaA: Weinheim, Germany, 2013.
- [46] Mayer, K. M.; Hafner, J. H. Localized Surface Plasmon Resonance Sensors. *Chemical Reviews* **2011**, *111*, 3828–3857.
- [47] De Mello Donegá, C., *Nanoparticles: Workhorses of Nanoscience*, 1st ed.; Springer-Verlag: Berlin, Germany, 2014.
- [48] Kwon, S. G.; Hyeon, T. Formation Mechanisms of Uniform Nanocrystals via Hot-Injection and Heat-Up Methods. *Small* **2011**, *7*, 2685–2702.
- [49] Thanh, N. T. K.; Maclean, N.; Mahiddine, S. Mechanisms of Nucleation and Growth of Nanoparticles in Solution. *Chemical Reviews* **2014**, *3*, 7610–7630.
- [50] Sugimoto, T., *Monodispersed Particles*, 2nd ed.; Elsevier: Amsterdam, Netherlands, 2019.
- [51] Klabunde, K. J.; Richards, R. M., *Nanoscale Materials in Chemistry*, 2nd ed.; John Wiley & Sons, Inc.: Hoboken, New Jersey, 2009.
- [52] LaMer, V. K.; Dinegar, R. H. Theory, Production and Mechanism of Formation of Monodispersed Hydrosols. *Journal of the American Chemical Society* **1950**, *72*, 4847–4854.
- [53] LaMer, V. K. Nucleation in Phase Transitions. *Industrial and Engineering Chemistry* **1952**, *44*, 1270–1277.
- [54] Murray, C. B.; Norris, D. J.; Bawendi, M. G. Synthesis and Characterization of Nearly Monodisperse CdE (E = S, Se, Te) Semiconductor Nanocrystallites. *Journal of the American Chemical Society* **1993**, *115*, 8706–8715.
- [55] Mehrer, H., *Diffusion in Solids*, 1st ed.; Springer-Verlag: Berlin, Germany, 2007.
- [56] Fick, A. Ueber diffusion. *Annalen der Physik* **1855**, *170*, 59–86.

- [57] Brown, R. Mikroskopische Beobachtungen über die im Pollen der Pflanzen enthaltenen Partikeln, und über das allgemeine Vorkommen activer Molecüle in organischen und unorganischen Körpern. *Annalen der Physik* **1828**, *90*, 294–313.
- [58] Einstein, A. Über die von der molekularkinetischen Theorie der Wärme geforderte Bewegung von in ruhenden Flüssigkeiten suspendierten Teilchen. *Annalen der Physik* **1905**, *4*.
- [59] Frenkel, J. I. Über die Wärmebewegung in festen und flüssigen Körpern. *Zeitschrift für Physik* **1926**, *35*, 652–669.
- [60] Wagner, C.; Schottky, W. Theorie der Geordneten Mischphasen. *Zeitschrift für Physikalische Chemie B* **1930**, *11*, 163–210.
- [61] Pearson, R. G. Hard and Soft Acids and Bases. *Journal of the American Chemical Society* **1963**, *85*, 3533–3539.
- [62] Parr, R. G.; Pearson, R. G. Absolute Hardness: Companion Parameter to Absolute Electronegativity. *Journal of the American Chemical Society* **1983**, *105*, 7512–7516.
- [63] Pearson, R. G. Absolute Electronegativity and Hardness: Application to Inorganic Chemistry. *Inorganic Chemistry* **1988**, *27*, 734–740.
- [64] Beberwyck, B. J.; Surendranath, Y.; Alivisatos, A. P. Cation Exchange: A Versatile Tool for Nanomaterials Synthesis. *Journal of Physical Chemistry C* **2013**, *117*, 19759–19770.
- [65] Chan, E. M.; Marcus, M. A.; Fakra, S.; ElNaggar, M.; Mathies, R. A.; Alivisatos, A. P. Millisecond Kinetics of Nanocrystal Cation Exchange Using Microfluidic X-ray Absorption Spectroscopy. *The Journal of Physical Chemistry A* **2007**, *111*, 12210–12215.
- [66] Zhang, J.; Chernomordik, B. D.; Crisp, R. W.; Kroupa, D. M.; Luther, J. M.; Miller, E. M.; Gao, J.; Beard, M. C. Preparation of Cd/Pb Chalcogenide Heterostructured Janus Particles via Controllable Cation Exchange. *ACS Nano* **2015**, *9*, 7151–7163.
- [67] Murray, C. B.; Kagan, C. R. Synthesis and Characterization of Monodisperse Nanocrystals and Close-Packed Nanocrystal Assemblies. *Annual Review of Material Science* **2000**, *30*, 545–610.
- [68] Talapin, D. V.; Rogach, A. L.; Haase, M.; Weller, H. Evolution of an Ensemble of Nanoparticles in a Colloidal Solution: Theoretical Study. *The Journal of Physical Chemistry B* **2001**, *105*, 12278–12285.
- [69] Cozzoli, P. D.; Pellegrino, T.; Manna, L. Synthesis, properties and perspectives of hybrid nanocrystal structures. *Chemical Society Reviews* **2006**, *35*, 1195–1208.

- [70] Jaishankar, M.; Tseten, T.; Anbalagan, N.; Mathew, B. B.; Beeregowda, K. N. Toxicity, mechanism and health effects of some heavy metals. *Interdisciplinary Toxicology* **2014**, *7*, 60.
- [71] Li, Z.; Ma, Z.; van der Kuijp, T. J.; Yuan, Z.; Huang, L. A review of soil heavy metal pollution from mines in China: pollution and health risk assessment. *Science of the Total Environment* **2014**, *468*, 843–853.
- [72] Kolny-Olesiak, J.; Weller, H. Synthesis and Application of Colloidal CuInS₂ Semiconductor Nanocrystals. *ACS Applied Materials and Interfaces* **2013**, *5*, 12221–12237.
- [73] Kriegel, I.; Jiang, C.; Rodríguez-Fernández, J.; Schaller, R. D.; Talapin, D. V.; Como, E. D.; Feldmann, J. Tuning the excitonic and plasmonic properties of copper chalcogenide nanocrystals. *Journal of the American Chemical Society* **2012**, *134*, 1583–1590.
- [74] Xu, Q.; Huang, B.; Zhao, Y.; Yan, Y.; Noufi, R.; huai Wei, S.; Xu, Q.; Huang, B.; Zhao, Y.; Yan, Y.; Noufi, R.; huai Wei, S. Crystal and electronic structures of Cu_xS solar cell absorbers. *Applied Physics Letters* **2012**, *100*, 061906.
- [75] Coughlan, C.; Ibáñez, M.; Dobrozhan, O.; Singh, A.; Cabot, A.; Ryan, K. M. Compound Copper Chalcogenide Nanocrystals. *Chemical Reviews* **2017**, *117*, 5865–6109.
- [76] Evans, H. T. Copper coordination in low chalcocite and djurleite and other copper-rich sulfides. *American Mineralogist* **1981**, *66*, 807–818.
- [77] Blachnik, R.; Müller, A. The formation of Cu₂S from the elements II. Copper used in form of foils. *Thermochimica Acta* **2001**, *366*, 47–59.
- [78] Han, W.; Yi, L.; Zhao, N.; Tang, A.; Gao, M.; Tang, Z. Synthesis and Shape-Tailoring of Copper Sulfide/Indium Sulfide-Based Nanocrystals. *Journal of the American Chemical Society* **2008**, *130*, 13152–13161.
- [79] Sun, S.; Li, P.; Liang, S.; Yang, Z. Diversified Copper Sulfide (Cu_{2-x}S) Micro-/Nanostructures: A Comprehensive Review on Synthesis, Modifications and Applications. *Nanoscale* **2017**, *9*, 11357–11404.
- [80] Kruszynska, M.; Borchert, H.; Bachmatiuk, A.; Rummeli, M. H.; Buechner, B.; Parisi, J.; Kolny-Olesiak, J. Size and Shape Control of Colloidal Copper(I) Sulfide Nanorods. *ACS Nano* **2012**, *6*, 5889–5896.
- [81] Zhao, Y.; Pan, H.; Lou, Y.; Qiu, X.; Zhu, J.; Burda, C. Plasmonic Cu_{2-x}S Nanocrystals: Optical and Structural Properties of Copper-Deficient Copper(I) Sulfides. *Journal of the American Chemical Society* **2009**, *131*, 4253–4261.
- [82] Evans, H. T. The crystal structures of low chalcocite and djurleite. *Zeitschrift für Kristallographie* **1979**, *150*, 299–320.
- [83] Mumme, G.; Gable, W. The Crystal Structure of Roxbyite, Cu₅₈S₃₂. *The Canadian Mineralogist* **2012**, *50*, 423–430.

- [84] Evans, H. T. Crystal Structure of Low Chalcocite. *Nature Physical Science* **1971**, 232, 69–70.
- [85] Roseboom, E. H. An investigation of the system Cu-S and some natural copper sulfides between 25° and 700° C. *Economic Geology* **1966**, 61, 641–672.
- [86] Okamoto, K.; Kawai, S. Electrical Conduction and Phase Transition of Copper Sulfides. *Japanese Journal of Applied Physics* **1973**, 12, 1130–1138.
- [87] Wang, L.-W. High Chalcocite Cu₂S: A Solid-Liquid Hybrid Phase. *Physical Review Letters* **2012**, 085703, 1–5.
- [88] Cassaignon, S.; Pauporté, T.; Guillemoles, J. F.; Vedel, J. Copper Diffusion in Copper Sulfide: a Systematic Study. *Ionics* **1998**, 4, 364–371.
- [89] Cassaignon, S.; Sanchez, S.; Guillemoles, J.; Vedel, J.; Meier, H. G. Influence of the Composition on the Copper Diffusion in Copper Sulfides. *Journal of The Electrochemical Society* **1999**, 146, 4666–4671.
- [90] Casavola, M.; Huis, M. A. V.; Bals, S.; Lambert, K.; Hens, Z.; Vanmaekelbergh, D. Anisotropic Cation Exchange in PbSe/CdSe Core/Shell Nanocrystals of Different Geometry. *Chemistry of Materials* **2012**, 24, 294–302.
- [91] Thiel, F.; Palencia, C.; Weller, H. Kinetic Analysis of the Cation Exchange in Nanorods from Cu_{2-x}S to CuInS₂: Influence of Djurleite's Phase Transition Temperature on the Mechanism. *ACS Nano* **2023**, 17, 3676–3685.
- [92] Cabot, A.; Iba, M.; Guardia, P.; Alivisatos, A. P. Reaction Regimes on the Synthesis of Hollow Particles by the Kirkendall. *Journal of the American Chemical Society* **2009**, 131, 11326–11328.
- [93] Mu, L.; Wang, F.; Sadtler, B.; Loomis, R. A.; Buhro, W. E. Influence of the Nanoscale Kirkendall Effect on the Morphology of Copper Indium Disulfide Nanoplatelets Synthesized by Ion Exchange. *ACS Nano* **2015**, 9, 7419–7428.
- [94] Pan, D.; An, L.; Sun, Z.; Hou, W.; Yang, Y.; Yang, Z.; Lu, Y. Synthesis of Cu-In-S Ternary Nanocrystals with Tunable Structure and Composition. *Journal of American Chemical Society* **2008**, 130, 5620–5621.
- [95] Makuła, P.; Pacia, M.; Macyk, W. How To Correctly Determine the Band Gap Energy of Modified Semiconductor Photocatalysts Based on UV-Vis Spectra. *Journal of Physical Chemistry Letters* **2018**, 9, 6814–6817.
- [96] Koo, B.; Patel, R. N.; Korgel, B. A. Wurtzite–Chalcopyrite Polytypism in CuInS₂ Nanodisks. *Chem. Mater.* **2009**, 21, 1962–1966.
- [97] Huang, W. C.; Tseng, C. H.; Chang, S. H.; Tuan, H. Y.; Chiang, C. C.; Lyu, L. M.; Huang, M. H. Solvothermal Synthesis of Zinblende and Wurtzite CuInS₂ Nanocrystals and Their Photovoltaic Application. *Langmuir* **2012**, 28, 8496–8501.

- [98] Luther, J. M.; Jain, P. K.; Ewers, T.; Alivisatos, A. P. Localized surface plasmon resonances arising from free carriers in doped quantum dots. *Nature Materials* **2011**, *10*, 361–366.
- [99] Lu, X.; Zhuang, Z.; Peng, Q.; Li, Y. Controlled synthesis of wurtzite CuInS₂ nanocrystals and their side-by-side nanorod assemblies. *CrystEngComm* **2011**, *13*, 4039–4045.
- [100] Connor, S. T.; Hsu, C.-M.; Weil, B. D.; Aloni, S. Phase Transformation of Biphasic Cu₂S–CuInS₂ to Monophasic CuInS₂ Nanorods. *Journal of the American Chemical Society* **2009**, *131*, 4962–4966.
- [101] Li, J.; Bloemen, M.; Parisi, J.; Kolny-Olesiak, J. Role of Copper Sulfide Seeds in the Growth Process of CuInS₂ Nanorods and Networks. *ACS Applied Materials and Interfaces* **2014**, *6*, 20535–20543.
- [102] Batabyal, S. K.; Tian, L.; Venkatram, N.; Ji, W.; Vittal, J. J. Phase-Selective Synthesis of CuInS₂ Nanocrystals. *The Journal of Physical Chemistry C* **2009**, *113*, 15037–15042.
- [103] Evans, H. T. Djurleite (Cu_{1.94}S) and Low Chalcocite (Cu₂S): New Crystal Structure Studies. *Science* **1979**, *203*, 356–358.
- [104] Rehwald, W.; Hweke, G. On the Conduction Mechanism in Single Crystal β -Indium Sulfide In₂S₃. *Journal of Physics and Chemistry of Solids* **1965**, *26*, 1309–1324.
- [105] Pistor, P.; Álvarez, J. M.; León, M.; Michiel, M. D.; Schorr, S.; Klenk, R.; Lehmann, S. Structure Reinvestigation of α -, β - and γ -In₂S₃. *Acta Crystallographica Section B: Structural Science, Crystal Engineering and Materials* **2016**, *72*, 410–415.
- [106] Stam, W. V. D.; Berends, A. C.; Donega, C. D. M. Prospects of Colloidal Copper Chalcogenide Nanocrystals. *ChemPhysChem* **2016**, *17*, 559–581.
- [107] Xia, C.; Oversteeg, C. H. V.; Bogaards, V. C.; Spanjersberg, T. H.; Visser, N. L.; Berends, A. C.; Meeldijk, J. D.; Jongh, P. E. D.; Donega, C. D. M. Synthesis and Formation Mechanism of Colloidal Janus-Type Cu_{2-x}S/CuInS₂ Heteronanorods via Seeded Injection. *ACS Nano* **2021**, *15*, 9987–9999.
- [108] Zhai, Y.; Flanagan, J. C.; Shim, M. Lattice Strain and Ligand Effects on the Formation of Cu_{2-x}S/I-III-VI₂ Nanorod Heterostructures through Partial Cation Exchange. *Chemistry of Materials* **2017**, *29*, 6161–6167.
- [109] Uehara, M.; Watanabe, K.; Tajiri, Y.; Nakamura, H.; Maeda, H. Synthesis of CuInS₂ fluorescent nanocrystals and enhancement of fluorescence by controlling crystal defect. *Journal of Chemical Physics* **2008**, *129*, 134709.

- [110] Akkerman, Q. A.; Genovese, A.; George, C.; Prato, M.; Moreels, I.; Casu, A.; Marras, S.; Curcio, A.; Scarpellini, A.; Pellegrino, T.; Manna, L.; Lesnyak, V. From Binary Cu_2S to Ternary Cu-In-S and Quaternary Cu-In-Zn-S Nanocrystals with Tunable Composition via Partial Cation Exchange. *ACS Nano* **2015**, *9*, 521–531.
- [111] Kim, Y.-K.; Ahn, S.-H.; Chung, K.; Cho, Y.-S.; Choi, C.-J. The photoluminescence of CuInS_2 nanocrystals: effect of non-stoichiometry and surface modification. *Journal of Materials Chemistry* **2012**, *22*, 1516–1520.
- [112] Shannon, R. D. Revised Effective Ionic Radii and Systematic Studies of Interatomic Distances in Halides and Chalcogenides. *Acta Crystallographica A* **1976**, *32*, 751–767.
- [113] Sands, T. D.; Washburn, J.; Gronsky, R. High Resolution Observations of Copper Vacancy Ordering in Chalcocite (Cu_2S) and the Transformation to Djurleite ($\text{Cu}_{1.97 \text{ to } 1.94}\text{S}$). *Physica Status Solidi A* **1982**, *72*, 551–559.
- [114] Pauporté, T.; Vedel, J. Temperature effects on copper diffusion in natural chalcocite. *Solid State Ionics* **1999**, *116*, 311–320.
- [115] Stam, W. V. D.; Berends, A. C.; Rabouw, F. T.; Willhammar, T.; Ke, X.; Meeldijk, J. D.; Bals, S.; Donega, C. D. M. Luminescent CuInS_2 Quantum Dots by Partial Cation Exchange in Cu_{2-x}S Nanocrystals. *Chemistry of Materials* **2015**, *27*, 621–628.
- [116] Wuensch, B. J.; Buerger, M. J. The Crystal Structure of Chalcocite, Cu_2S . *Mineralogical Society of America* **1963**, *1*, 164–170.
- [117] Gariano, G.; Lesnyak, V.; Brescia, R.; Bertoni, G.; Dang, Z.; Gaspari, R.; Trizio, L. D.; Manna, L. Role of the Crystal Structure in Cation Exchange Reactions Involving Colloidal Cu_2Se Nanocrystals. *Journal of the American Chemical Society* **2017**, *139*, 9583–9590.
- [118] Lesnyak, V.; Brescia, R.; Messina, G. C.; Manna, L. Cu Vacancies Boost Cation Exchange Reactions in Copper Selenide Nanocrystals. *Journal of the American Chemical Society* **2015**, *137*, 9315–9323.
- [119] Sadtler, B.; Demchenko, D. O.; Zheng, H.; Hughes, S. M.; Merkle, M. G.; Dahmen, U.; Wang, L.; Alivisatos, A. P. Selective Facet Reactivity during Cation Exchange in Cadmium Sulfide Nanorods Selective Facet Reactivity during Cation Exchange in Cadmium Sulfide Nanorods. *Journal of the American Chemical Society* **2009**, *131*, 5285–5293.
- [120] Ha, D. H.; Caldwell, A. H.; Ward, M. J.; Honrao, S.; Mathew, K.; Hovden, R.; Koker, M. K.; Muller, D. A.; Hennig, R. G.; Robinson, R. D. Solid-solid phase transformations induced through cation exchange and strain in 2D heterostructured copper sulfide nanocrystals. *Nano Letters* **2014**, *14*, 7090–7099.

- [121] Fenton, J. L.; Steimle, B. C.; Schaak, R. E. Tunable intraparticle frameworks for creating complex heterostructured nanoparticle libraries. *Science* **2018**, *360*, 513–517.
- [122] Qi, Y.; Liu, Q.; Tang, K.; Liang, Z.; Ren, Z.; Liu, X. Synthesis and Characterization of Nanostructured Wurtzite CuInS₂: A New Cation Disordered Polymorph of CuInS₂. *Journal of Physical Chemistry C* **2009**, *113*, 3939–3944.
- [123] Bothe, C.; Kornowski, A.; Tornatzky, H.; Schmidtke, C.; Lange, H.; Maultzsch, J.; Weller, H. Solid-State Chemistry on the Nanoscale: Ion Transport through Interstitial Sites or Vacancies? *Angewandte Chemie - International Edition* **2015**, *54*, 14183–14186.
- [124] Tao, J.; Chen, J.; Li, J.; Mathurin, L.; Zheng, J. C.; Li, Y.; Lu, D.; Cao, Y.; Wu, L.; Cava, R. J.; Zhu, Y. Reversible structure manipulation by tuning carrier concentration in metastable Cu₂S. *Proceedings of the National Academy of Sciences of the United States of America* **2017**, *114*, 9832–9837.
- [125] Yoon, D.; Jin, H.; Ryu, S.; Park, S.; Baik, H.; Oh, S. J.; Haam, S.; Joo, C.; Lee, K. Scalable synthesis of djurleite copper sulphide (Cu_{1.94}S) hexagonal nanoplates from a single precursor copper thiocyanate and their photothermal properties. *CrystEngComm* **2015**, *17*, 4627–4631.
- [126] Abdelhady, A. L.; Ramasamy, K.; Malik, M. A.; O'Brien, P.; Haigh, S. J.; Raftery, J. New routes to copper sulfide nanostructures and thin films. *Journal of Materials Chemistry* **2011**, *21*, 17888–17895.
- [127] Li, C.; Wang, W.; Yang, Y.; Liu, S.; Zhu, C.; Tian, Q. Core-shell Cu_{1.94}S–MnS nanoheterostructures synthesized by cation exchange for enhanced photocatalytic hydrogen evolution. *CrystEngComm* **2021**, *23*, 6291–6299.
- [128] Philips Lighting. Datenblatt TL-D Schwarzlicht. https://www.lighting.philips.ch/prof/konventionelle-lampen-und-leuchtstofflampen/speziellampen/farbige-und-schwarzlicht-leuchtstofflampen/tl-d-schwarzlicht/928048010805_EU/product (accessed: 2023-01-17).
- [129] Sigma-Aldrich. Sicherheitsdatenblatt. <https://www.sigmaaldrich.com/DE/de/> (accessed 2023-01-17).
- [130] Strem Chemicals. Sicherheitsdatenblatt. https://www.strem.com/uploads/sds/sd15-1337_DE.pdf (accessed 2023-01-18).
- [131] Institut für Arbeitsschutz der Deutschen Gesetzlichen Unfallversicherung. Liste der krebserzeugenden, keimzellmutagenen und reproduktionstoxischen Stoffe (KMR-Stoffe). <https://publikationen.dguv.de/widgets/pdf/download/article/3517> (accessed: 2023-01-17).